ABSTRACT

Title of Thesis: DEVELOPMENT, VALIDATION AND APPLICATION OF RESISTANCE - CAPACITANCE BASED MODELS (RCM) FOR PHASE CHANGE MATERIAL HEAT EXCHANGERS

Tanjebul Alam, Master of Science, 2023

Thesis Directed By: Research Professor Vikrant Aute, Department of Mechanical Engineering

Latent thermal energy storage use Phase Change Material (PCM) because of its ability to absorb or release a large amount of latent heat within a narrow temperature range. The low conductive heat transfer in PCMs can be improved with thermal enhancement techniques such as the addition of highly conductive metal foams and extended surfaces like fins or periodic metal structures within the PCM domain. High-order modeling tools like Computational Fluid Dynamics (CFD) are widely used for the simulation of different types of PCM heat exchangers (HXs). High computing costs are typically associated with CFD, particularly for the complex transient phase-change processes. This becomes restrictive in some applications such as PCMHX optimization where the conventional process is limited by the computational cost of the high-order physics models. A simulation tool with a faster turnaround is necessary for such cases, even if it comes with a small accuracy penalty. Resistance-capacitance based model (RCM) can be a suitable solution for this type of problem as the model is computationally inexpensive. RCM does not solve for the mass and momentum governing equations as in CFD, but can still predict the PCMHX characteristics with reasonable accuracy, especially for configurations where conduction is the dominant heat transfer mechanism. This work presents the development of RCMs for four types of PCMHXs which are a rectangular PCM enclosure enhanced with copper foam subject to constant heat flux, a geometry enhanced with 3D lattice structures subject to constant heat flux, a cylindrical PCMHX with annular fins and tube in conjugate heat transfer with single-phase heat transfer fluid and a cylindrical PCMHX with annular fin and tube enhanced with copper foam. In all these geometries the effect due to the flow of molten PCM can be considered negligible and the geometries are regarded as structured. The models were validated against experimental data and compared against CFD models for computational cost and prediction accuracy. Both of the models predicted the energy storage within 0.8% of the experimental data for the rectangular PCM enclosure enhanced with copper foam. For the cylindrical PCMHX with annular fins, the maximum RMSE for average PCM temperature prediction was found to be 0.62K for CFD and 0.7K for RCM. These results show that RCM can predict the average temperature profile and energy storage up to 5 orders of magnitude faster than CFD while having negligible prediction deviation. The validated model for annular finned PCMHX is used with a multi-objective genetic algorithm to optimize a PCMHX integrated with a domestic water heater. Additionally, thermal Ragone plots were generated to compare different designs at various operating conditions which can be used for optimal design selection.

DEVELOPMENT, VALIDATION AND APPLICATION OF RESISTANCE-CAPACITANCE BASED MODELS FOR PHASE CHANGE MATERIAL HEAT EXCHANGERS

by

Tanjebul Alam

Thesis submitted to the Faculty of the Graduate School of the
University of Maryland, College Park, in partial fulfillment
of the requirements for the degree of
Master of Science
2023

Advisory Committee:
Research Professor Vikrant Aute, Chair
Professor Bao Yang
Associate Professor Damena Agonafer

Dedication

To

Ridwana and Raiya

Acknowledgements

I would like to express my deepest gratitude to my thesis advisor, Dr. Vikrant Aute, for his support and guidance throughout the entire research work. His expertise in the field and willingness to share knowledge have been invaluable to me. Thank you, Dr. Aute, for accepting me as a part of this outstanding research team.

I am truly grateful for the time and effort Dr. Daniel Bacellar dedicated to provide insightful comments and suggestions on my work. He showed enormous patience in developing my research skills which have greatly improved the final product. His eagerness to provide constructive criticism and support throughout the research journey has been an inspiration to me.

I would also like to thank all the professors I had during my time at the University of Maryland, particularly, Dr. Bao Yang, and Dr. Damena Agonafer, for their helpful feedback and suggestions on my thesis.

I am indebted to Professor Reinhard Radermacher for being a source of constant motivation to me through his passion for the field of energy systems. I acknowledge Dr. Jiazhen Ling for always extending a helping hand during hardship; Jangho Yang for all his endeavor in the testing and providing the data to validate my models; Jan Muehlbauer, whose laboratory experience is unparalleled; and Heat Transfer Technologies LLC for prototyping the heat exchangers.

The people I have worked with in CEEE have been incredible. Thank you, Dr. James Tancabel, for the numerous technical discussions and your inexhaustible patience. The first person I met from the lab was Rajath Subbappa and he has been a source of support and encouragement since. I will miss having conversations with Brian O'Malley and

Alhussain Othman about random things in life. Thanks to Lalith Kannah, Dr. Ransisi Huang, Suraj Krishnamurti, Vijay Meruva, Rui Liu, Ellery Klein and, Dr. Dongyu Chen for the positive influence they had during my time in CEEE. Dr. Turash Haque Pial and Raihan Ali Khan, thanks for always being there when I missed talking to someone in Bangla.

I would like to thank my parents and siblings for their encouragement and unconditional support. I also want to express my gratitude towards my wife, Ridwana Binte Sharif, for her constant emotional support. Without her, it would not have been possible to complete this journey.

This material is based upon work supported by the U.S. Department of Energy's Office of Energy Efficiency and Renewable Energy (EERE) under the Building Technologies Office Award Number DE-EE0009158. The views expressed herein do not necessarily represent the views of the U.S. Department of Energy or the United States Government. This work was also supported in part by the Modeling and Optimization Consortium at the University of Maryland.

Table of Contents

List of Tables

List of Figures

Nomenclature

a	Experiment start time	(s)
A	Area	(m^2)
b	Experiment end time	(s)
c_p	Specific heat	(J/kg-K)
C	Heat capacity	(J/kg-K)
D	Diameter	(mm)
E	Energy storage	(J)
F	Fin pitch	(mm)
ΔH	Latent heat	(J/kg)
I	Current	(A)
k	Thermal conductivity	(W/m-K)
L	PCM domain length	(m)
LF	Liquid Fraction	(-)
m	Mass	(kg)
M	Number of segments lengthwise	(-)
MR	Melting Range	(K)
N	Number of segments widthwise	(-)
P	Pressure	(Pa)
$\dot{Q}$	Heat flow	(W)
$\dot{Q}''$	Heater heat flux	(W/m^2)
$\dot{Q}_{loss}$	Heat loss	(W)
RMSE	Root mean square error	(-)
SOC	State of Charge	(%)
$T_{H,avg}$	Heater average temperature	(°C)
T_{sol}	Solidification temperature	(K)
T_{melt}	Liquidous temperature	(K)
T_{exp}	Experimental temperature	(K)
T_{sim}	Simulation temperature	(K)
T_{max}	Maximum temperature in experiment	(K)
T_{min}	Minimum temperature in experiment	(K)
TC	Thermocouple	(-)
T	Temperature	(K)
Δt	time step size	(s)
R	Thermal resistance	(K/W)
V	Volume	(m^3)
W	PCM domain width	(m)

Greek

α	Real-time factor	(-)
β	Thermal Expansion Coefficient	(1/K)
γ	Porosity	(-)
ρ	Density	(kg/m^3)
μ	Viscosity	(kg/m-s)
σ	Deviation	(-)

Subscripts

Alloy	Metal alloy
amb	Ambient
B	Base
cond	Conduction
conv	Convection
eff	Effective
e	Electrochemical
Fin	Fins
Foam	Copper foam
H	Heater
HW	Hot water
i	Specific segment number (lengthwise)
j	Specific segment number (widthwise)
max	Maximum
min	Minimum
P	PCM
t	Specific timestep
T	Tube
Temp	Temperature
th	Thermal
W	Wall
s	Solid phase
l	Liquid phase
0	lengthwise direction
1	widthwise direction
L	Longitudinal direction
R	Radial direction

Chapter 1 Introduction

The energy consumption worldwide is predicted to grow by approximately 50% between 2018 to 2050 [1]. Heating, ventilation, and air conditioning (HVAC) accounts for 38% of building energy consumption, equivalent to 12% of global energy[2]. Due to this additional energy demand, the grid-demand response becomes more challenging and there will be higher carbon emission with traditional fossil fuel-based energy sources. Renewable energy such as wind and solar will play a significant role in reducing carbon emissions but they have intermittency. Energy storage is a necessary component to address such challenge. In addition to smoothing the variability in renewable energy production, storage technology can also provide backup or standby power that comes from fossil fuel sources.

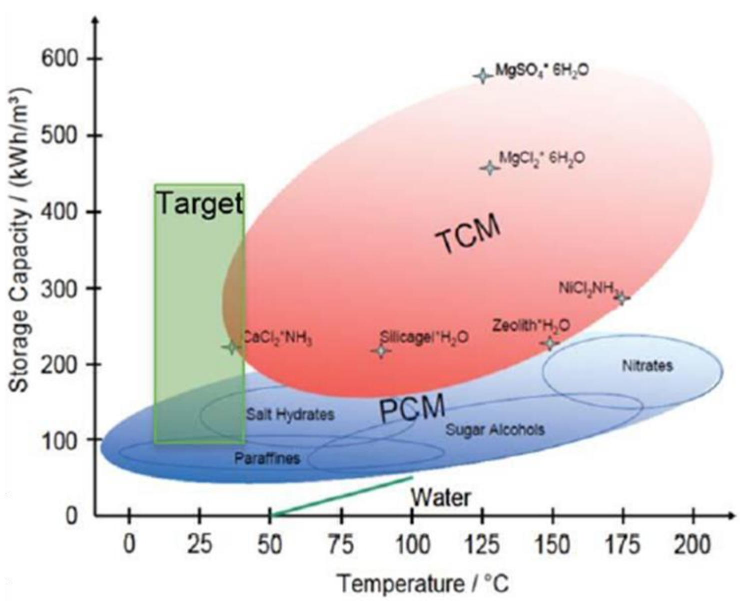

Figure 1: PCM Storage Capacity and Target Application Range [3]

Thermal energy storage (TES) is a promising technology due to its lower cost and environmental impact compared to other technologies [4]. In TES, energy can be stored in the form of sensible or latent heat, or thermochemically. Thermochemical energy storage can be a promising technique but the high transition temperature in this technology is out of range for HVAC related applications as shown in Figure 1.

The sensible and latent energy systems are considered mature technology and has been widely researched [5]. The main advantage of latent system over sensible is its high energy density and the capacity of storing a large amount of energy within a small temperature range. Latent thermal storage use phase-change materials (PCMs) to absorb or release latent heat in a narrow temperature range. PCM heat exchangers (PCMHXs) can offer an efficient way to reduce peak load by using the energy stored in off-peak hours to offset the on-peak load partially or fully. The load shifting tries to take advantage of the difference in electricity demands between different times of the day as shown in Figure 2.

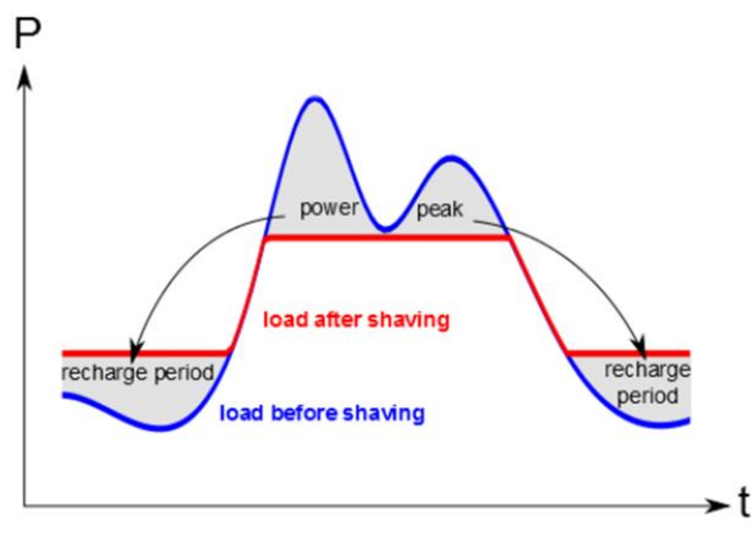

Figure 2: Schematic of load shifting control [6]

1.1 Literature Review

PCM energy storage models have been developed using both analytical and numerical methods in the literature. Elgafy & Lafdi [7] provided an analytical approach based on one-dimensional heat conduction in PCM enhanced with carbon nanofiber to predict the effective thermal conductivity using the effective thermal resistance approach. The study assumed that the carbon nanofibers are uniformly distributed. The study only compares the effective thermal conductivity but does not compare the transient temperature profile or the energy storage. Lamberg & Siren [8] provided a simplified approximate analytical model for solidification in a rectangular PCM storage with internal fins to predict the solid–liquid interface location and temperature distribution of the fin. The model assumes a constant value for solidification temperature and a constant wall temperature. In reality, PCMs have a solidification range and the wall temperature is not necessarily constant in most of the cases. The analytical solution is comprised of the Neumann solution [9] for the solid-liquid interface location and a derived analytical solution for the temperature distribution of the fin.

Shamberger [10] defined a figure of merit (FOM) of PCMs from the analytical solution of the two phase Neumann-Stefan problem [11] with constant wall boundary condition. The FOM depends highly on the PCM thermophysical properties and is defined with equation (1), where α is the thermal diffusivity, k is the conductivity, li is the subscript denoting liquid phase and λ is the solution to the transcendental equation which describes the position of meting front [10].

$$FOM = \frac{k_l}{\sqrt{\alpha_l} erf(\lambda)} \quad (1)$$

FOM can be used as an objective function for selection of material for electronics based thermal management that require faster dynamic response. Yazawa et al. [12] built on this study and used a lumped mass model for mapping different materials showing power and energy tradeoff. FOM was used to compare the cooling power capability of different PCMs and single-phase materials. FOM was also plotted against energy density to graphically demonstrate performance tradeoff between different materials as shown in Figure 3.

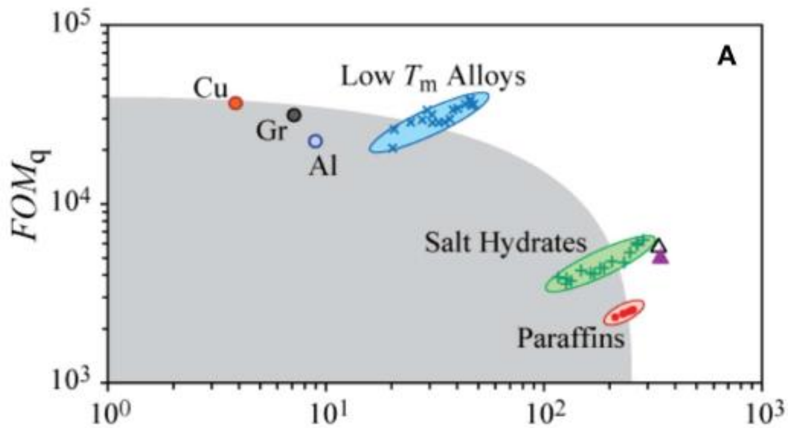

Figure 3 : FOM against specific energy for different PCMs and single phase materials [12]

Table 1: Thermophysical properties of PCMs and calculated FOM

PCM	**Specific Heat (J/kg-K)**	**Thermal Conductivity (W/m-K)**	**Latent Heat, (kJ/kg)**	**Density (kg/m^3)**	**FOM ($W/K\text{-}m^2\text{-}s^{0.5}$)**	**Energy Density (MJ/m^3)**
RT35	1800(s) 2400(l)	0.2	160	860(s) 770(l)	2391	130.4
RT62HC	1800(s) 2400(l)	0.2 (s) 0.1(l)	230	850(s) 840(l)	2134	194.4
RT35+ Copper foam (2%)	1772(s) 2360(l)	7.8	156.8	1021(s) 933(l)	16300	127.8
ClimaSel 32	3600	1.08(s) 0.76(l)	145	1500	7178	217.5

Using the approach from Shamberger [10], a FOM and energy density can be created for the PCMs that were used in this study as shown in Table 1.The first two PCMs in the table are organic PCMs and the third one is a composite of 98% RT35 and 2% copper foam. The properties of the composite were calculated based on effective porosity. The last row of the table is for an inorganic PCM ClimaSel32. From the table and equation (1) it can be seen that the thermal conductivity is responsible for the change in FOM and Shamberger reported that conductivity was responsible for 92.8% of the variance in different materials [10]. In the table, the composite showed the highest FOM but the lowers energy density as for incorporating the metal foams it lost some PCM storage. This highlights the importance of thermal conductivity enhancement for PCM based storage but also demonstrates the tradeoff between energy and power.

The major advantage of analytical models is their ability to predict trends at a low computational cost to accuracy's detriment. Moreover, these approximate techniques are generally limited to one-dimensional analysis and simpler domains. Analytical solution does not exist for more complicated geometries, mushy interfaces and other boundary conditions and numerical method is necessary.

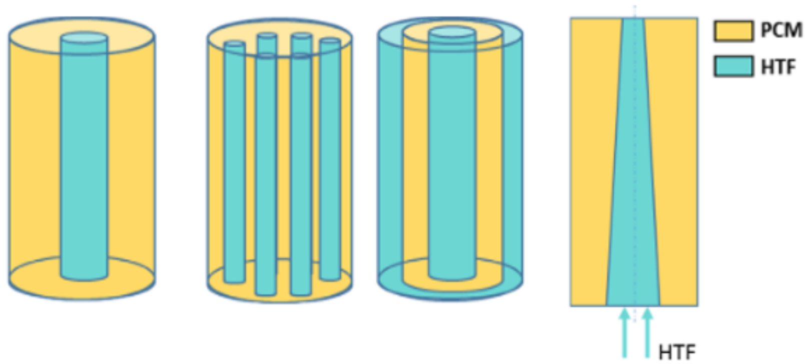

Figure 4 : Different Configurations of Cylindrical and Frustum-Shaped PCMHX [13]

Numerical methods, such as finite difference, finite element and finite control volume methods are more powerful in solving the complex multidimensional models. The use of Computational Fluid Dynamics (CFD) is the most extensively found in various heat transfer applications, including PCMHX's [14], [15], [24]–[30], [16]–[23] . Figure 4 shows some examples of different cylindrical and frustum-shaped PCMHX configurations that were studied in the literature. The different color in the figure indicates the domain of PCM storage area and the HTF flow. Figure 5 illustrates the 3D meshing of different PCMHX geometries created for CFD analysis.

CFD usually imposes high computation cost especially for complex problems such as time-dependent phase-change processes. Bacellar et al. [31], [32] investigated reduced order model using CFD-based correlations and reduced order domain for faster evaluation of PCMHX. The results showed good match to the CFD simulations with 4 to 5 orders of magnitude less computational cost compared to CFD. But generating correlations that cover a large design space can still be computationally expensive. In certain applications, this may become prohibitive as such that a faster simulation engine with a certain degree of accuracy penalty is acceptable and needed.

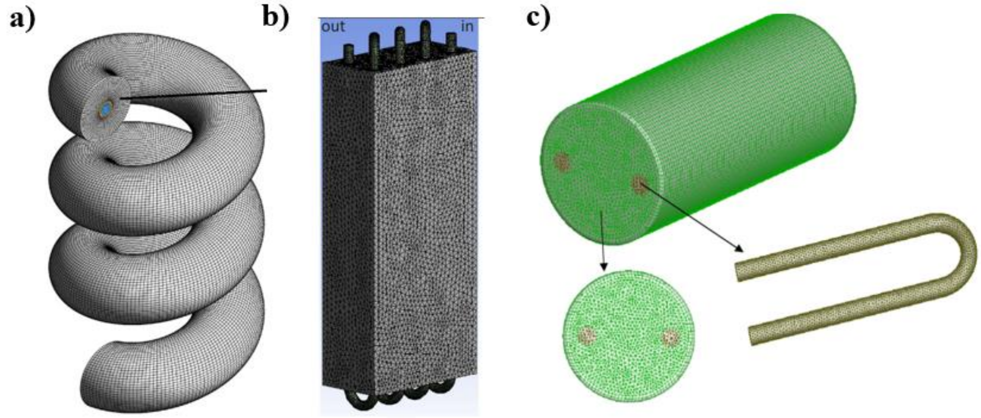

Figure 5: 3D meshing of a) Double pipe helical coil PCMHX [33] **b) PCMHX with spiral-wired tubes** [27] **c) Shell and tube PCMHX with heat pipe**[15]

Lattice Boltzmann method (LBM) is a mesoscopic numerical method [34] which has been used to model heat transfer process in PCMHX. While CFD solves the Navier-Stokes equations, LBM solves the Boltzmann equation [34] in discrete forms and the implementation of this method can describe the fluid motion without solving the Navier-Stokes equations. LBM can have 2 times lower computational cost [35] than CFD due to the model using explicit scheme and local interactions. Consequently, this approach has a very low communication ratio to run efficiently in parallel supercomputers [36].

Liu and He [37] developed a LBM model for PCM melting in porous media and verified the model with data from literature. Gao et al. [38] used an enthalpy-based LBM for porous PCM melting with fins where the solid-liquid phase interface is distinguished by calculating liquid fraction. Li et al. [39] proposed an axisymmetric LBM for PCMHX solidification and validated their model by the experimental data from Sparrow et al. [40]. The study also showed that LBM can be two orders of magnitude faster compared to CFD. Chen et al. [41] developed a axisymmetric LBM model for melting in a cylindrical heat exchanger with copper foam. The model was validated from experimental data [42] and good match of experimental temperature and predicted temperature was found. While LBM can be faster than CFD, most of the PCMHXs simulated with LBM are comparatively simple and use constant temperature or constant heat flow boundary conditions. The conjugate heat transfer between HTF and PCM is usually not considered as the implementation of energy conservation scheme in LBM is not straightforward. The pre-processing of input and post-processing of output data is also complex in LBM. The twofold speed gain by using LBM may still be restrictive for applications where faster turnaround is required and thus a faster solver is needed.

An alternate approach is the resistances and capacitances-based models (RCM), which has been used for developing building thermal models [43] and heat exchanger modeling [44]. Unlike CFD or LBM, RCM does not solve for the high-order physics which means the continuity and momentum equations. The model only solves for the energy balance equation and thus have significantly less computational cost. The PCM domain is represented with thermal resistance and capacitance [45]–[49] and an example is shown in Figure 6 which represents a RC network representation for a shape-stabilized PCM slab. This method can provide good estimation of heat transfer rate and energy storage. Gao et al. [47] reported that the average error of surface temperature and heat flux predictions are 0.42°C and 15% respectively when compared to experimental data for a shape-stabilized PCM slab. Mirzaei et al. [49] compared their model against CFD and the obtained mean errors for solidification and melting process were found to be 0.11 K and 0.44 K respectively. These models are 1D and assume conduction as the dominant heat transfer mechanism..

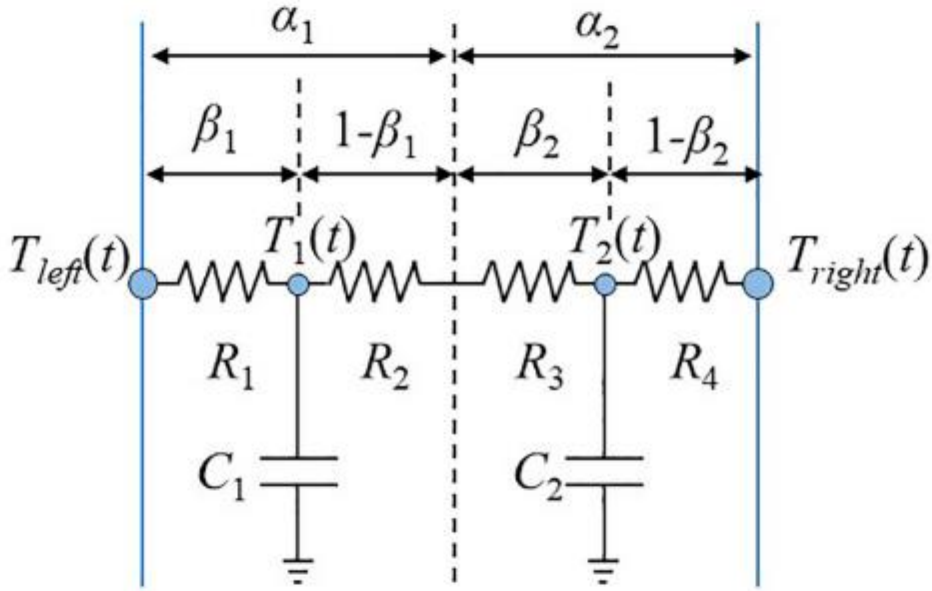

Figure 6: Schematic of the RC network of Shape-Stabilized PCM Slab [47]

Pan et al. [50] introduced an approach which they named Layered Thermal Resistance (LTR) for PCMHX solidification simulation in multi-dimensions with and without fins. The model assumes a quasi-steady heat conduction approach. The liquid PCM is assumed to be solidified layer by layer and once a layer is fully solidified the solidification front moves to the next layer as shown in Figure 7. The total solidification time of the domain is estimated by summing up the solidification times of all the different layers. When compared to a CFD model it was first found that the LTR model overestimated the solidification time by 50-60%. A regression model was later used to find a tuning parameter from the CFD model to tune the resistance in LTR. The model was verified with a CFD model after the tuning. However, this tuning with the configuration and operation specific correction factor limits its applicability.

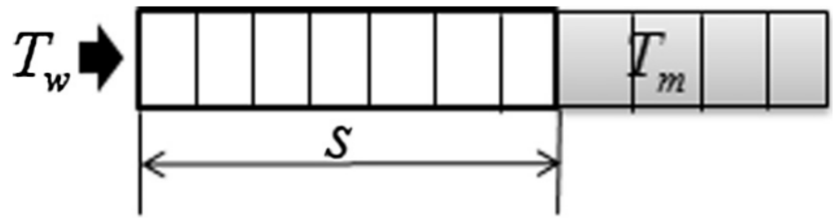

Figure 7: 1D Layered Thermal Resistance solidification front [40]

Parsazadeh et al. [51] proposed an improved LTR model for better prediction of the solid-liquid phase change process. Unlike the original model, this improved model considered transient heat conduction in each layer and did not use a tuning factor. The new model showed better predictions of solidification time than the previous model for large Stefan numbers (ratio of sensible-to-latent heat). The higher Stefan number indicates more sensible heat utilization which means higher degree of superheating or subcooling.

Neumann et al. [52] proposed a simplified 2D RC-model for a flat plate PCM energy storage. The model accounted for free convection during the melting process in rectangular PCM gaps between the flat plates (Figure 8), based on CFD based correlations developed by Vogel et al. [53]. According to Vogel et al. [53] the natural convection effect is significant when the melting process reaches a critical liquid fraction which is a function of the Rayleigh number (Ra) and geometry parameter A in equation (2).

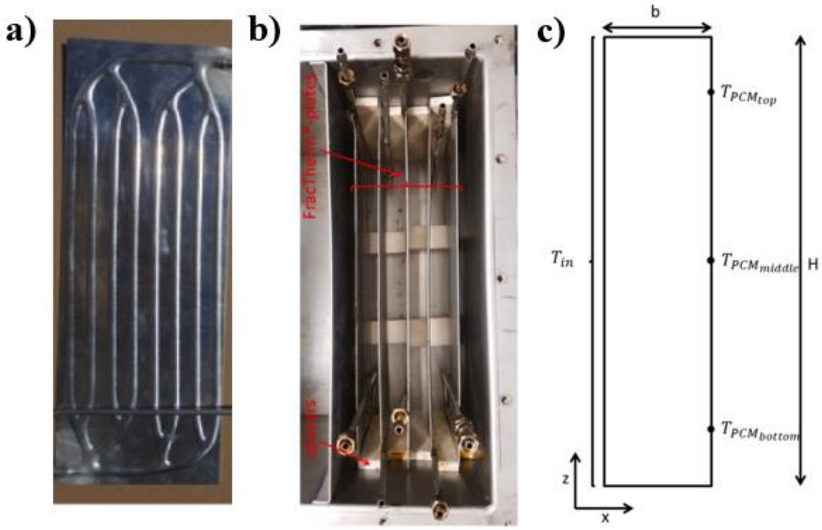

Figure 8: Schematic of a) used flat plate b) top view of storage envelope c) 2D computational domain for a PCM gap [42]

A is the ratio of PCM gap (b) and the gap height (H) as shown in Figure 8c. If the liquid fraction (f) was lower than the critical liquid fraction f_{crit} , the heat transfer in the RC-model was defined by only heat conduction. If the liquid fraction goes over the critical value a reduction factor $\overline{\boldsymbol{\varepsilon}}$ is used to add the effect of natural convection in the model as shown in equation(3). These equations are developed for rectangular PCM gaps in flat plate PMCHX and may not be valid for other configurations.

$$f_{crit} = \sqrt[4]{\frac{150A}{Ra}} \tag{2}$$

$$\overline{\varepsilon} = \begin{cases} 1 & for\ Ra^{\frac{1}{6}}A^{-\frac{1}{4}} < 2.73 \\ 0.57\left(Ra^{\frac{1}{6}}A^{-\frac{1}{4}}\right) - 0.38 & for\ Ra^{\frac{1}{6}}A^{-\frac{1}{4}} \geq 2.73 \end{cases} \tag{3}$$

Neumann et al. [52] validated the RC-model with a finite element model (FEM), and reported that the mean deviation of the outlet fluid temperature and PCM temperature between both models were 0.62Kand 0.85K, respectively. The simulation time for the RC model was reduced by 20-30 times compared to the FEM. This study considered a geometry where the motion of liquid PCM is significant. But for geometries where the flow of molten PCM is negligible, the natural convection effect can be considered less dominant and be dismissed in favor of computational speed gains [31].

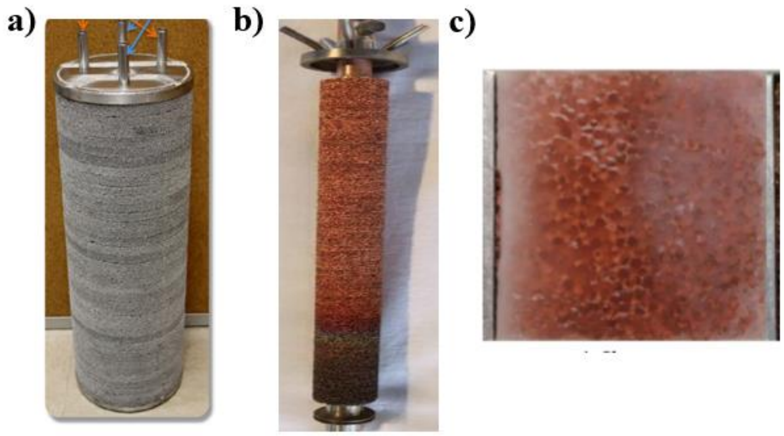

Figure 9: PCMHX with a) Cylindrical Aluminum Metal Foam [54] **b) Cylindrical Copper Metal Foam** [42] **c) Rectangular Copper Metal Foam** [55]

A simple way for thermal enhancement in PCMHX is embedding porous materials with high thermal conductivity like metal foam. This method has been explored widely both experimentally [28], [54]–[57] (shown in Figure 9) and with CFD based numerical methods in different studies [16], [19], [28], [30]. The presence of high conductivity metal foam in this geometry means that the flow of molten PCM is restricted and the heat transfer is largely diffusion based. The effect of buoyancy can be neglected in this type of geometry which makes it very suitable for simplified solver like RCM. However, RCM for this type of geometry has not been discussed in literature.

Another type of thermal enhancement technique is adding periodic metal structures to the PCMHX container as shown in Figure 10. In contrast to metal foam enhancement, the porosity (ratio of metal and PCM volume) is not uniform everywhere in this structure. To develop RCM for this type of structures, a scheme is required to find the porosity in each segment which has not been discussed in literature.

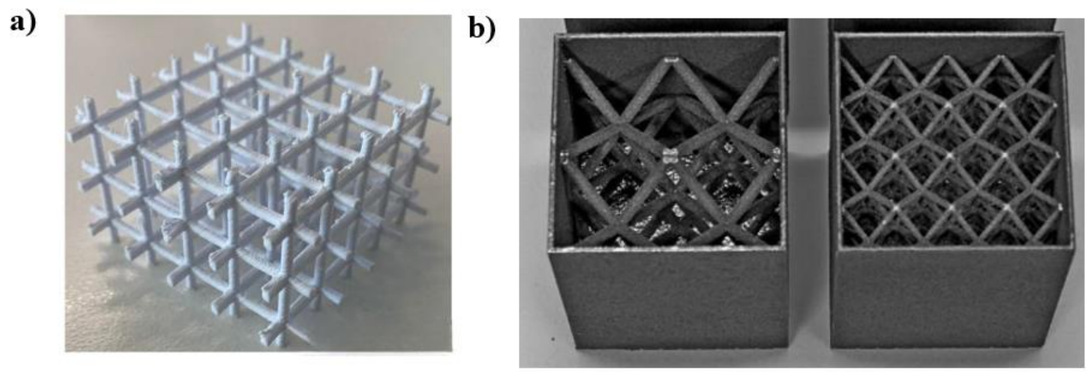

Figure 10: Periodic Structured Enhancements for PCMHX [58]**,** [59]

Enhancing PCM thermal conductivity by adding fins in cylindrical PCMHX been widely studied in the literature with both experimental [17], [25], [60] and CFD based numerical studies [23], [25], [26], [29]. Again, the presence of conductive fins and limited space between the fins and the container in this type of geometry makes it suitable to be studied with simplified models like RCM but was not explored by the researchers.

Different PCMHX modeling approaches covered in this review are summarized in Table 2. Table 3 briefly summarizes different PCMHX modeling approaches based on the accuracy, computational cost and the ability to solve complex geometries.

Table 2: Summary of Different Modeling Techniques

Author	Model Type	Software	Dimension	Validation
Elgafy & Lafdi [7]	Analytical	NA	1D	Yes. Experimental
Lamberg & Siren [8]	Analytical	NA	1D	No
Longeon et al. [20]	CFD	Ansys FLUENT	2D	Yes. Experimental
Pu et al. [23]	CFD	Ansys FLUENT	2D	Yes. Data from Longeon et al. [20]
Zhang et al. [29]	CFD	Ansys FLUENT	2D	Yes. Data from Longeon et al. [20]
Tay et al. [24]	CFD	Ansys CFX	3D	Yes. Data from Tay et al. [62]
Duan et al. [63]	CFD	Ansys FLUENT	3D	Yes. Experimental
Yang et al. [26]	CFD	Ansys FLUENT	2D	Yes. Experimental
Jian-you [64]	Simple iterative model	NA	1D	Yes. Experimental
Al-Abidi et al [14]	CFD	Ansys FLUENT	2D	Yes. Experimental
Mat et al. [22]	CFD	Ansys FLUENT	2D	Yes. Experimental
Mahdi & Nsofor [65], [66]	CFD	Ansys FLUENT	2D	Yes. Data from Esapour et al.[16]
Youssef et al. [27]	CFD	Ansys FLUENT	3D	Yes. Experimental
Ebrahimi et al. [15]	CFD	Ansys FLUENT	3D	Yes. Data from Elgafy et al. [5]
Mahdi et al. [21]	CFD	Ansys FLUENT	3D	Yes. Experimental
Koukou et al. [18]	CFD	Ansys FLUENT	2D	Yes. Experimental
Hu et al. [67]	CFD	Ansys FLUENT	2D	Yes. Data from Akgün et al. [68]
Faghani et al. [69]	CFD	Ansys FLUENT	2D	Yes. Data from Assis et al. [70]
Assis et al. [70]	CFD	Ansys FLUENT	2D	Yes. Experimental
Zhao et al. [71]	CFD	Ansys FLUENT	2D	Yes. Data from Al-Abidi et al. [72]
Najafian et al. [73]	-	TRNSYS	2D	No
Righetti et al.[74]	-	TRNSYS	2D	Yes. Experimental

Dhumane et al. [75]	-	Modelica	NA	Yes, Data from Du et al. [76]
Dhumane et al. [77]	-	Modelica	NA	Yes, Data from Du et al. [78]
Promoppatum et al.[79]	CFD	COMSOL	2D	Yes. Experimental
Zhang et al. [80]	CFD	COMSOL	2D	Yes, Experimental
Calvet et al. [81]	CFD	COMSOL	2D	Yes. Experimental
Bacellar et al. [31]	CFD	Ansys FLUENT	2D	NA
Bacellar et al.[32]	CFD	Ansys FLUENT	2D	NA
Velraj et al.[82]	FDM	NA	1D	Yes. Experimental
Ismail et al.[83]	FDM	NA	1D	Yes. Experimental
Erek et al. [84]	FDM	FDM	2D	Yes. Experimental
Liu & He[37]	LBM	NA	2D	No
Gao et al. [38]	LBM	NA	2D	No
Li et al. [39]	LBM	NA	2D	Yes. Data from Sparrow et al. [40]
Liu et al. [85]	LBM	NA	2D	No
Chen et al.[41]	LBM	NA	2D	Yes. Data from Martinelli et al.[42]
Zhu et al. [45]	RCM	NA	1D	Yes. Experimental
Bontemps et al. [46]	RCM	TRNSYS	1D	Yes. Experimental
Gao et al. [47]	RCM	NA	1D	Yes. Experimental
Stupar et al. [48]	RCM	NA	1D	No
Mirzaei et al. [49]	RCM	NA	1D	No
Neumann et al. [52]	RCM	NA	2D	Yes. Experimental

Table 3: Comparison of PCMHX Modeling Approaches

Approach	**Physics Order**	**Accuracy**	**Computational Cost**
Analytical	Low	Low	Low
RCM	Low	Medium	Low
LBM	High	High	High
RCM	High	Very High	Very High

Predicting the temperature profile and energy storage with numerical models is difficult without accurate knowledge of PCM thermophysical properties. Specific heat, density, latent heat, and thermal conductivity are typically available from manufacturer datasheet, while others such as thermal expansion coefficient, viscosity and melting temperature range are seldom included. Several studies have discussed the impact of the commonly available thermophysical properties in PCM-based simulations [86]–[88]. However, the literature lacks a more holistic discussion of the impact of thermal expansion coefficient (β), viscosity (μ) and the melting range on the PCM-HX performance. In the literature, for some PCMs these values can be found but they are not always consistent across references. For instance, the reported values of β and μ as reported in different literatures can vary by a whole order of magnitude, as shown in Table 4.

Table 4: Properties of PCM RT35 from Different Literature Sources

Source	β (1/K)	μ (kg/m-s)	Latent Heat (kJ/kg)
Pu et al. [23]	0.001	0.0029	157
Longeon et al. [20]	0.001	0.0027	157
Ebadi et al. [89]	0.0006	0.023	160
Rahimi et al. [90]	0.0006	NA	170
Manufacturer Datasheet [91]	NA	NA	160

None of these papers mention any experimental or calculation procedure for estimating these parameters. Some of the variations in the data may also be attributed to editing or typos but without a literature source or any calculation procedure it is difficult to confirm this hypothesis are generally determined using specific instruments which are not always accessible and can be an expensive process both in cost and time.

To the best of the author's knowledge, there is no simple method to estimate these values for different PCMs. This is a significant gap in the research for the numerical modeling of PCMHX which needs more in-depth discussions, which however, are beyond the scope of this work.

Lin et al. [92] studied integration of PCM in HVAC system for a solar decathlon house and used an analytical model with particle swarm optimization for optimized geometric and operation variables for maximum energy density. They reported an energy density improvement from 13.58 to 26.47 kWh/m^3 with optimized designs. Malik et al. [93] studied solar still desalination system with PCM and used an analytical model with multi-objective genetic algorithm (MOGA) for optimized PCM mass and brine water flow rate for maximum exergy efficiency and distilled water rate. The exergy efficiency increased about 1.47% and annual distilled water increased by 4.35%. Zhou et al. [94] optimized for mass flow rate and inlet temperature of water in PCM integrated system with PV to maximize overall output energy in five regions in China. This study used MOGA and artificial neural network for optimization and reported an increase in overall output energy by up to 7.4% in Kunming. Najafian et al. [73] studied integration of PCM in domestic water heater with MOGA and artificial neural network with TRNSYS and optimized for best location for PCM containers in water tank and PCM mass. These optimization studies are mainly performed with low accuracy models and did not look into the optimization of heat exchanger geometry. Yang et al. [26] used a CFD based model to study the effect of fin thickness and fin numbers on PCM melting rate in an annular finned PCMHX but due to high computational cost the study did not perform a full optimization.

Summarizing, analytical solutions have been mainly explored as simple 1D models and the solution procedure can get difficult for multidimensional and more complex geometries. Numerical models like CFD have been widely used in the literature for PCMHX simulation but the computational cost associated with this modeling approach is expensive due to the phase change process being intrinsically transient. along with the uncertainty of PCM thermophysical properties and its effect on these simulations have not been extensively discussed. LBM is a promising modeling approach; however, it has been usually applied to simple PCMHX geometries with constant temperature and heat flux boundary condition and the computational cost may still be prohibitive. RCM can provide significant speed increase and is suitable for tasks where rapid simulation is needed. The modeling of natural convection may not be necessary for PCMHX geometries with metal foams and fins which can be considered structured. These geometries are suitable to be studied with simplified models like RCM but has not been explored much with this approach.

1.2 Research Gaps

CFD is widely used for numerical studies of PCMHX but can be computationally expensive and this cost is not typically mentioned in the literature. There is also uncertainty regarding the accuracy of PCM thermophysical properties and their consistency across the literature. CFD-based studies have not extensively discussed the effects of thermophysical properties that are less frequently available. In order to optimize PCMHX simulation performance, accuracy, and computational cost, it is necessary to understand which heat transfer mechanism is dominant and which one can be ignored for simulation speed gain with negligible penalty in accuracy.

High accuracy with a simplified modeling approach like RCM is possible when the effect of buoyancy in PCM can be considered negligible and modeling the natural convection can be disregarded for simulation speed. This assumption can be made for structured PCMHX with thermal enhancements like highly conductive metal foams, periodic structures, and fins. These techniques to deal with low PCM thermal conductivity has been widely used but RCM for these types of geometries has not been explored extensively. In most RCMs, the boundary conditions tend to be constant temperature and heat flux, and there are not many validated models with conjugate heat transfer between HTFs and PCM. The literature also lacks discussion on systematic design optimization workflow for PCMHX optimization using RCM and multi objective optimization.

1.3 Objectives

The objectives of this study are to:

- Quantify the impact of uncertainty in thermophysical properties on performance prediction of PCMHX
- Develop a flexible, computationally efficient, and accurate model for common PCMHX
- Demonstrate application of RCM for design optimization of PCMHX and evaluate computational efficacy

1.4 Thesis Organization

The rest of the thesis is organized as follows. In Chapter 2, the development of CFD and RCM models for different PCMHX is discussed. Chapter 3 discusses the CFD computational cost and the effect of some PCM thermophysical properties on CFD-based simulations. Chapter 4 shows the RCM model validations and also contains the comparison of speed and accuracy between RCM and CFD. In Chapter 5, the applications of RCM are demonstrated with an optimization study, Ragone plot generation, and web tool development. Finally, Chapter 6 summarizes the work, lists the contributions and recommends future work.

Chapter 2 Modeling Approach

2.1 CFD Modeling

2.1.1 PCMHX Geometries

Annular PCM storage is a common technique for storing latent energy and has been investigated extensively by researchers for both experimental and numerical studies. These devices are made up of two concentric cylinders where the heat transfer fluid (HTF) flows through the inner tube and the PCM fills up the annular space. Ismail and Abugderah [95] and Trp et al. [96] modeled these devices by removing the HTF, the tube wall domain and only taking diffusion as a heat transfer model in the PCM domain for simplification. While these studies provide simple numerical solution, they do not consider the effect of natural convection in the PCM domain. It has been experimentally shown by Ettouney et al. [97], Agyenim et al. [98], Hosseini et al. [99] and Longeon et al. [20], that the natural convection plays a major role in the melting process of PCM when the flow of liquid PCM is not constrained. Numerical studies by Mesalhy et al.[100] , Longeon et al. [20], Hosseini et al. [101] and Pu et al.[23] have discussed the necessity of considering natural convection for fitting the models with experimental results for setups where PCM can flow.

Predicting the effect of natural convection in a model can be difficult as the it depends on PCM thermophysical properties, gravitational forces, thickness of liquid PCM layer and the flow direction of HTF. One of the major challenges in modeling phase-change process in CFD, is the lack of information regarding thermophysical properties of PCMs, e.g., melting temperature range (typically not a single melting or solidification point, viscosity and thermal expansion coefficient. These can have critical impact on the buoyancy and heat transfer predictions when natural convection is not negligible like in a configuration without any thermal enhancement. For configurations with fins and copper foam the effect of natural convection may be negligible due to restriction to the flow of liquid PCM.

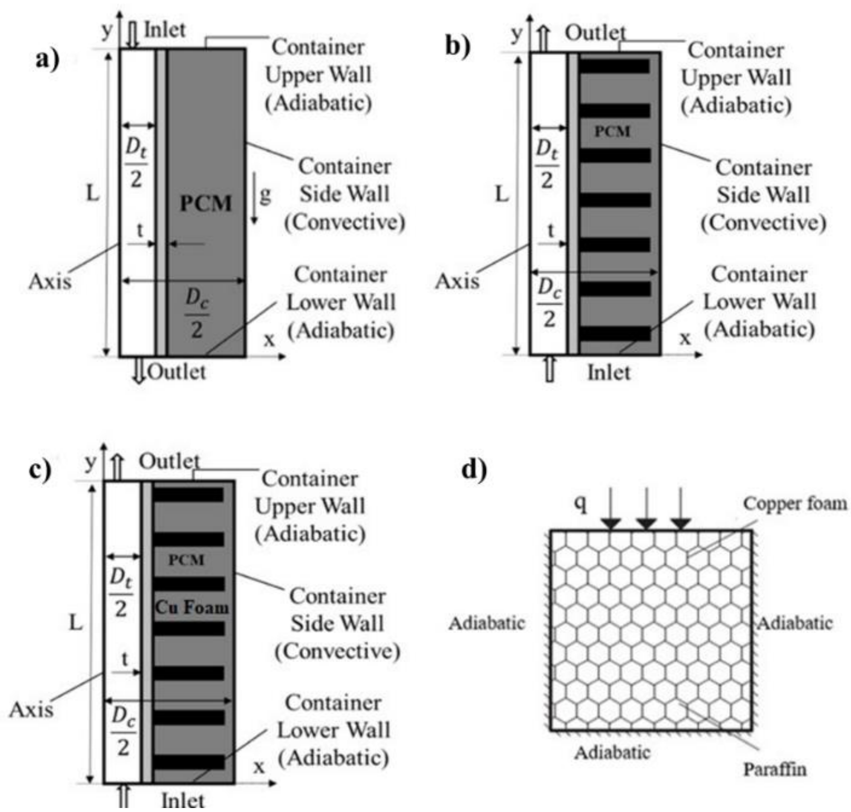

Figure 11: Computational domain of- cylindrical PCMHX with straight tube a) with no fins b) with annular fins c) with annular fins and copper foam and d) rectangular PCM enclosure enhanced with copper foam [55]

In this study CFD based numerical models were studied for four different PCMHX configurations and three of those are based on a cylindrical PCMHX with straight tube and PCM in the annular space. The geometries are- a) non-finned b) annular finned c) annular finned and copper foam, as shown in Figure 11. All these geometries had conjugate heat transfer with single-phase heat transfer fluid.

Additionally, another CFD model was studied which was a rectangular PCM enclosure enhanced with copper foam (Figure 11d) subject to constant heat flux.

A complete 3D model considering the conjugate heat transfer between working fluid and PCM, is computationally too intensive to solve in CFD. In the literature, this type of problem is often solved by reducing it to a two-dimensional axisymmetric domain (Figure 11). In this work, such a model was analyzed in ANSYS Fluent 2019 R3.

2.1.2 Governing Equations

The solidification and melting module in ANSYS Fluent is used to simulate the phase-change process of PCM which uses the Enthalpy-porosity model [102], [103]. Natural convection is taken into consideration during PCM melting process using Boussinesq approximation [19], [20], [30]. The thermophysical properties of the HTF, fin and foam materials are constant. The specific heat of PCM is set as piecewise linear function of temperature All the other properties of the PCM were assumed constant. The governing equations to describe flow and heat transfer of the PCM and HTF are given as-

The continuity equation is written as:

$$\frac{\partial \rho}{\partial t} + \frac{\partial (\rho u)}{\partial x} + \frac{\partial (\rho v)}{\partial y} = 0 \tag{4}$$

The momentum equation can be written as,

$$\frac{\partial (\rho u)}{\partial t} + \frac{\partial (\rho u u)}{\partial x} + \frac{\partial (\rho u v)}{\partial y} = -\frac{\partial P}{\partial x} + \mu \frac{\partial}{\partial x}\left(\frac{\partial u}{\partial x}\right) + \mu \frac{\partial}{\partial y}\left(\frac{\partial u}{\partial y}\right) + S_u \tag{5}$$

$$\frac{\partial (\rho v)}{\partial t} + \frac{\partial (\rho u v)}{\partial x} + \frac{\partial (\rho v v)}{\partial y} = -\frac{\partial P}{\partial y} + \mu \frac{\partial}{\partial x}\left(\frac{\partial v}{\partial x}\right) + \mu \frac{\partial}{\partial y}\left(\frac{\partial v}{\partial y}\right) + S_v \tag{6}$$

where,

$$S_u = Au \tag{7}$$

$$S_v = Av + \rho g \beta (T - T_L) \tag{8}$$

$$A = \frac{C(1 - LF^2)}{LF^2 + \varepsilon} \tag{9}$$

ρ is the PCM density, g is the gravitational acceleration, β is the thermal expansion coefficient, C is the mushy zone parameter set as 10^5 and ε is a small constant of 0.001. The Thermal Expansion Coefficient *(β)* and Melting Range (MR) are all part of the momentum source term in the momentum equation and is required to model the transition between solid and liquid phase. An increase in *β* will proportionally increase the buoyancy force and the impact of natural convection as shown in equation (8) . MR dictates at what temperature the phase change process is complete. Increasing viscosity (*μ)* impacts the viscous force by slowing down the fluid motion, and thus reducing the natural convection as shown in equation (5). Because of the phase change phenomena, the buoyancy and viscous terms have more impact than the inertial terms. LF is the liquid mass fraction and time required for LF to reach the value of 1 is defined as melting time. LF is defined as:

$$LF = \begin{cases} 0 & T < T_s \\ \dfrac{T - T_s}{T_L - T_s} & T_s \le T \le T_L \\ 1 & T > T_L \end{cases} \tag{10}$$

The complete energy equation in its differential form is written as,

$$\frac{\partial(\rho T)}{\partial t} + \frac{\partial(\rho u T)}{\partial x} + \frac{\partial(\rho v T)}{\partial y} = \frac{\partial}{\partial x}\left(k\frac{\partial T}{\partial x}\right) + \frac{\partial}{\partial y}\left(k\frac{\partial T}{\partial y}\right) + S \tag{11}$$

S is the source item in PCM region which is defined as-

$$S = -\rho \Delta H \frac{\partial(LF)}{\partial t} \quad (12)$$

where ΔH is the latent heat of PCM, k is the PCM conductivity.

The enthalpy (h) can be described as-

$$h = \begin{cases} \int_{T_r}^{T} c_p dT & T < T_s \\ \int_{T_r}^{T_s} c_p dT + LF * \Delta H & T_s \leq T \leq T_L \\ \int_{T_r}^{T_s} c_p dT + LF * \Delta H + \int_{T_L}^{T} c_p dT & T > T_L \end{cases} \quad (13)$$

Here T_r is the reference temperature which is 288.15 K. The energy equation solved for the fins is-

$$\rho_{fin} c_{p,fin} \frac{\partial T}{\partial t} = \frac{\partial}{\partial x}\left(k_{fin} \frac{\partial T}{\partial x}\right) + \frac{\partial}{\partial y}\left(k_{fin \frac{\partial T}{\partial y}}\right) \quad (14)$$

For the foam, the non-equilibrium porous medium model in Fluent is used. Structure of porous medium is assumed to be homogeneous, isotropic and open-celled between porous medium and PCM. The energy equation in the PCM and the foam can be written by using equations (15) and (16) respectively.

$$\mathrm{\gamma \rho c_p} \frac{\partial \mathrm{T}}{\partial \mathrm{t}} + \frac{\partial(\mathrm{\rho u T})}{\partial \mathrm{x}} + \frac{\partial(\mathrm{\rho v T})}{\partial \mathrm{y}} = \mathrm{k_{fe}}(\frac{\partial^2 \mathrm{T}}{\partial \mathrm{x}^2} + \frac{\partial^2 \mathrm{T}}{\partial \mathrm{y}^2}) + +\mathrm{h_{sf} A_{sf}}\,(\mathrm{T_f} - T_s) + \mathrm{S} \quad (15)$$

$$(1 - \gamma)\rho_s c_{p,s} \frac{\partial \mathrm{T_s}}{\partial \mathrm{t}} = \mathrm{k_{se}}(\frac{\partial^2 \mathrm{T}}{\partial \mathrm{x}^2} + \frac{\partial^2 \mathrm{T}}{\partial \mathrm{y}^2}) + +\mathrm{h_{sf} A_{sf}}\left(\mathrm{T_s} - T_f\right) \quad (16)$$

Here subscript s refers to metallic foam. γ is the porosity, k_{fe} is the effective fluid thermal conductivity, k_{se} is the solid effective thermal conductivity, h_{sf} is inertial heat-transfer coefficient between liquid PCM and porous foam and A_{sf} is the area between PCM and porous foam. k_{fe} , k_{se} , h_{sf} and A_{sf} are calculated based on the equations by Esapour et al. [16].

The results from CFD models for different geometries discussed in this section will be discussed later and will be compared against both experimental and RCM model for validation and computational cost comparison.

2.2 Resistance Capacitance Based Model (RCM)

2.2.1 RCM Geometries

The RCM is lightweight compared to CFD as it does not solve higher-order physics but still can provide good accuracy using an approximation of the thermal resistance at a very low computational cost. In this study RCM has been developed for four different PCMHX configurations and two of those are based on a cylindrical PCMHX with straight tube and PCM in the annular space with enhancement. The geometries are- a) annular finned b) annular finned and copper foam as shown in Figure 11. There geometries had conjugate heat transfer with single-phase heat transfer fluid. Additionally, another RCM was studied for a rectangular PCM enclosure enhanced with copper foam (Figure 11d) subject to constant heat flux.

Righetti et al. [58], [104] investigated PCMHXs with additively manufactured aluminum structured ligaments in a lattice structure for thermal enhancement. Three different geometries with different base pore sizes were added to the PCM and the porosity was kept constant so as to compare the performance of designs with same storage potential (i.e., volume of PCM). The addition of enhancement resulted in faster energy storage and release in the PCMHX compared to a baseline design without the lattice structures. Higher number of ligaments with smaller diameter resulted in lower melting times and more uniform temperature distribution.

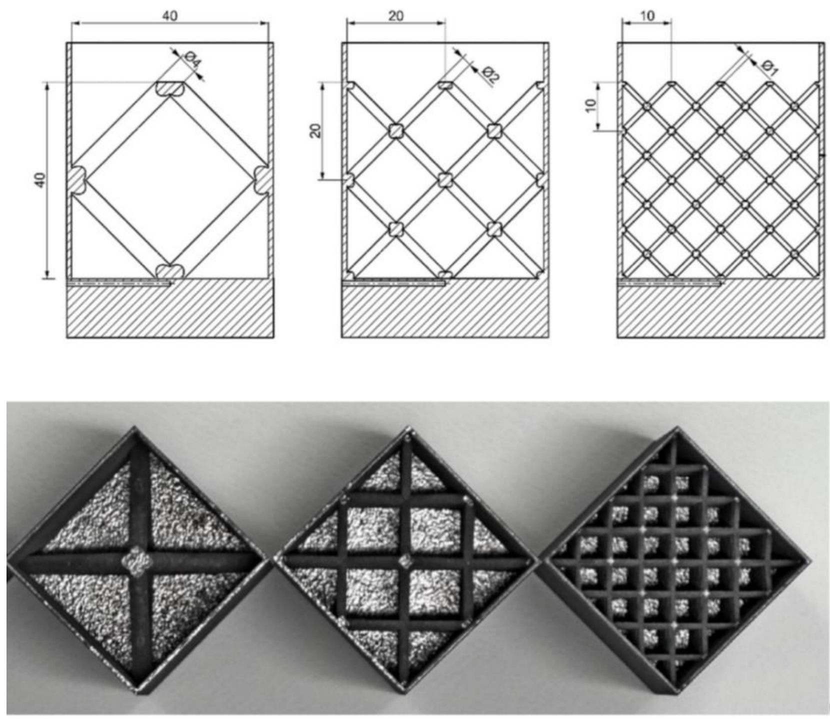

Figure 12: Additively manufactured 3D periodic structures [104]

Figure 12 shows three different additively manufactured periodic structures which were experimentally tested under different heat flux conditions [104]. The porosity (ratio of PCM volume and container volume) for all the geometries was 0.95. In our study we developed RCM for these three geometries.

In this work, RCM has been applied to such PCMHX geometries where convection heat transfer within the liquid PCM can be ignored due to the presence of conductive metal as fins and foam. The gravitational effects can thus be neglected as the heat transfer will be mainly dominated by the high conductive heat transfer rate.

2.2.2 RCM Assumptions

The general assumptions in RCM for all the configurations are –

- Effects of natural convection are negligible and heat transfer is conduction-dominated
- The properties of a given segment is constant and the entire segment can be described by a point at the center of the segment
- The PCM, fins and foams are not considered as separate materials and an effective medium was considered where the effective material properties are calculated based on the volume of material present in a segment
- The effect of contact resistance is ignored
- No mass transfer in between segments

Apart from these assumptions, additional problem specific assumptions have been made for individual configurations.

2.2.3 RC Network Development

Figure 13 shows the thermal network of heat flow in the 1D RCM representation of the physical model for the rectangular PCM enclosure enhanced with copper foam. The computational domain is discretized into equal-length segments and each of the segments has the same resistance and capacitance as uniform porosity was assumed. It was assumed that there was no heat loss from the walls.

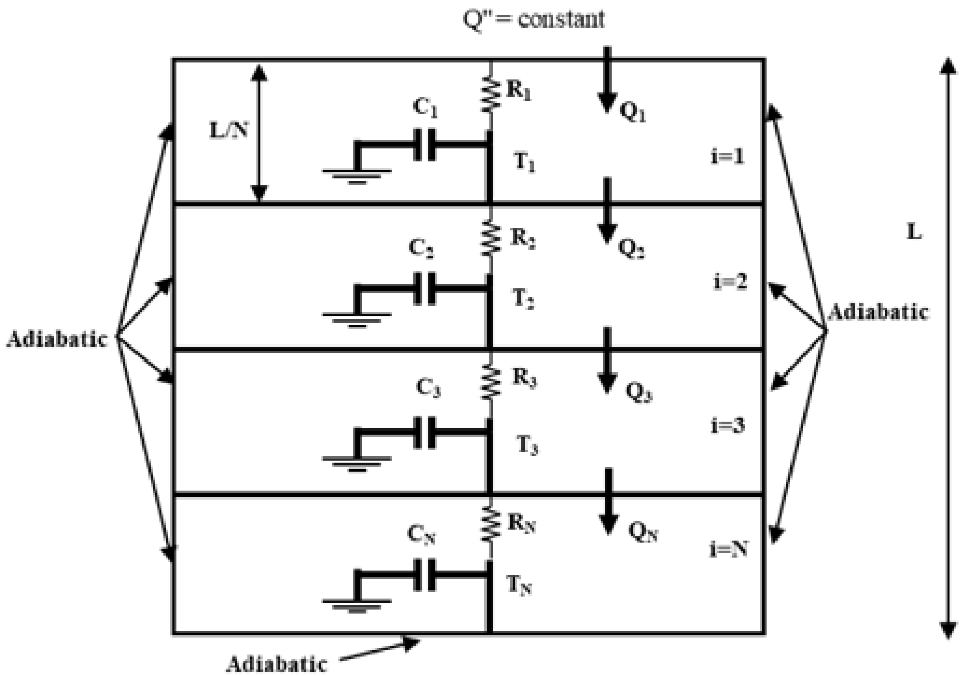

Figure 13: Thermal Network of 1D RCM for PCM with copper foam

Figure 14 shows the thermal network of heat flow in the RCM representation for the 3D periodic structures. The computational domain is discretized into segments of equal length and width, and each segment has an individual resistance and capacitance in contrast to the previous geometry. The thermal resistance and capacitance in each of the segments are dependent upon the porosity of the segment.

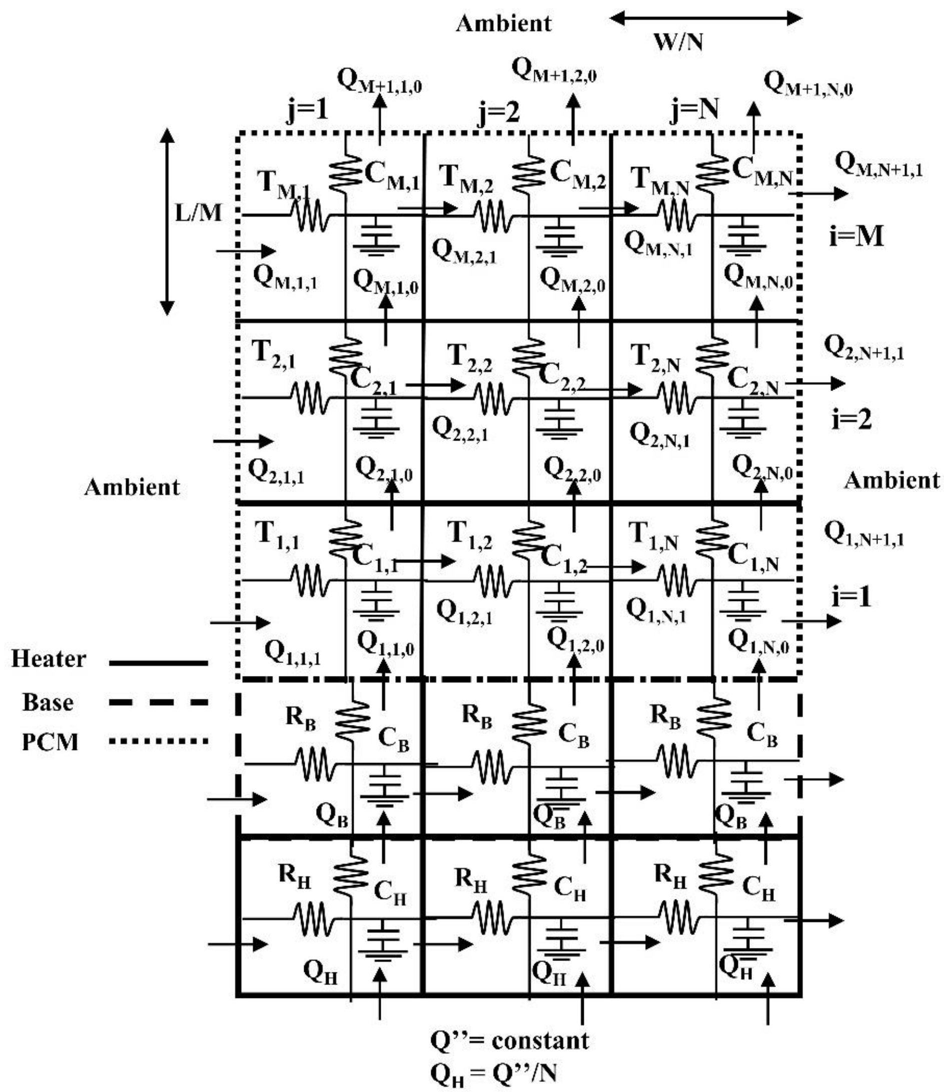

Figure 14: Thermal network of 2D RCM for periodic structures

Figure 15 shows the thermal network of heat flow in the RCM representation of the annular finned straight tube PCMHX. The computational domain is divided into three separate zones which are the HTF or the tube side, the tube wall and the PCM and fins zone. For the annular finned and copper foam configuration, PCM, fins and foams are assumed to be a homogeneous material with the effective material properties are calculated based on the volume of material present in a segment.

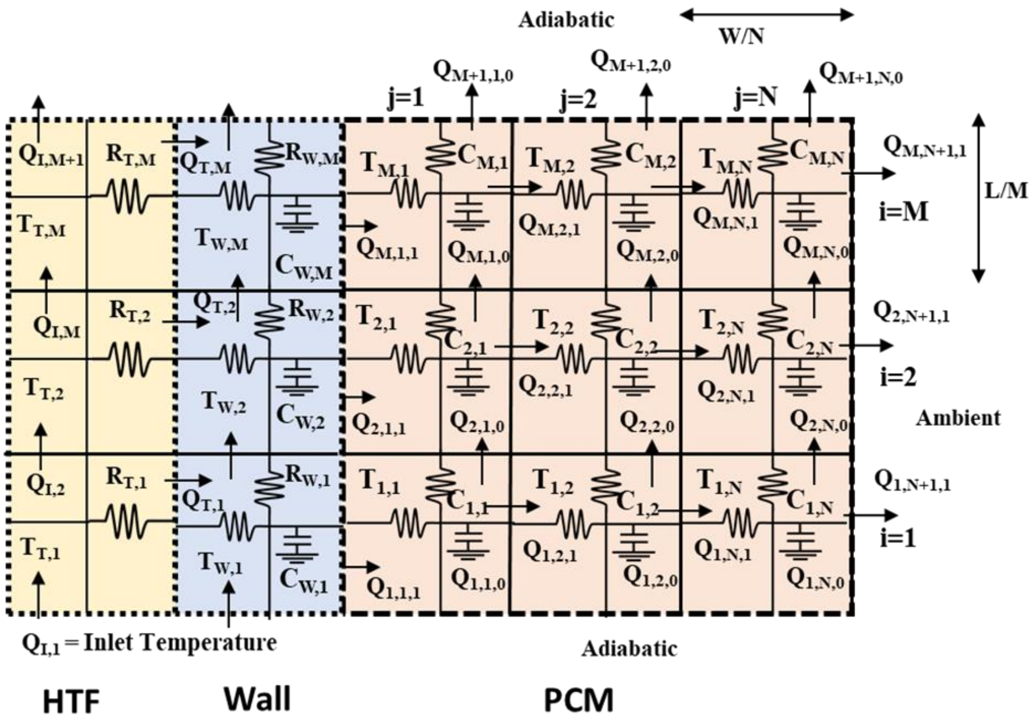

Figure 15: Thermal Network of 2D RCM for Annular Finned PCMHX

The PCM and fin domain is discretized into equal-length segments in both vertical and radial direction. The tube and the wall are only discretized in the vertical direction. Each of the segments has individual resistance and capacitance. Heat transfer between the tube and tube wall are calculated based on the laminar flow correlations available in literature.

2.2.4 Non-uniform Porosity Calculation

For the 3D lattice structures, the thermal resistance and capacitance in each of the segments are dependent upon the porosity of the segment which is not uniform. 2D discretization of the geometries are shown in Figure 16. In the figure, the solid black lines represent the metal structures, the dotted lines are grid lines and the white background represents the PCM.

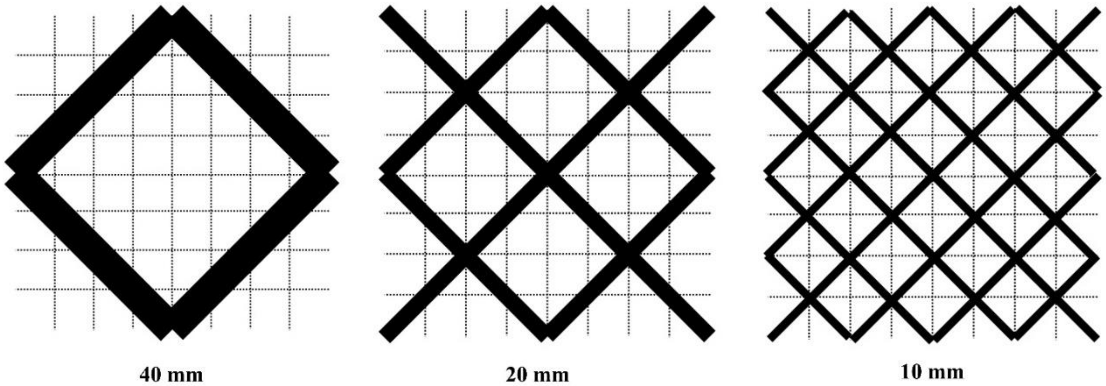

Figure 16: 2D discretization of periodic structures

Using the image processing capability of MATLAB [105], a program is set up to read these images pixel by pixel. The number of white and black pixels in a grid provides the face area of the lattice structure in a grid and the total face area of the grid based on a 2D image. Porosity is a volume based (3D) calculation and equation was used to convert the 2D area-based estimation to volume-based porosity.

$$\gamma_{i,j} = \frac{V_{PCM,i,j}}{V_{T,i,j}} = 1- \frac{V_{alloy,i,j}}{V_{T,i,j}} = 1- \frac{A_{alloy,i,j}}{A_{T,i,j}}\left(\frac{V_{alloy,i,j}}{V_{T,i,j}}\frac{A_{T,i,j}}{A_{alloy,i,j}}\right) \qquad (17)$$

$$\frac{V_{alloy}}{V_T}\frac{A_T}{A_{alloy}} = 0.1643;$$

The same approach is used to calculate the porosity for each segment in the annular finned PCMHX.

2.2.5 Explicit Time Marching Formulation

The explicit time marching formulation is used to solve for the transient temperature profile in the PCM domain and consequently the energy stored in the RCM can be calculated. All the RCM for different configurations is solved using the same methodology. Here, the explicit time marching formulation for the annular finned PCMHX is shown as it is the most complex one.

The thermal network parameters on the tube side can be calculated based on the equations (18)-(21).

$$R_{T,i,t} = \frac{1}{h_w A\_t} \tag{18}$$

$$\dot{Q}_{T,i,t} = \frac{T_{T,i,t} - T_{W,i,t}}{R_{T,i,t}} \tag{19}$$

$$T_{T,i,t} = T_{w,in};\ i = 1 \tag{20}$$

$$\mathrm{T_{T,i,t} = T_{T,i-1,t} - \frac{\dot{Q}_{T,i,t}}{\dot{m}_w c_{p,w}}\ ;\ i \geq 2} \tag{21}$$

The thermal network parameters on the wall can be calculated based on the equations (22)-(27).

$$R_{W,i,R} = \frac{M ln \frac{D_o}{D_i}}{2\pi L k_w} \tag{22}$$

$$\dot{Q}_{W,i+1,t} = \frac{T_{W,i,t} - T_{W,i+1,t}}{R_{W,i,V}} \tag{23}$$

$$\dot{Q}_{P,i,0,t} = \frac{T_{W,i,t} - T_{i,0,t}}{R_{W,i,t,R}} \tag{24}$$

$$\frac{dT_{W,i,t+1}}{dt} = \frac{\dot{Q}_{T,i,t} + \dot{Q}_{W,i,t} - \dot{Q}_{W,i+1,t} - \dot{Q}_{P,i,0,t}}{C_{W,i,t}} \tag{25}$$

$$T_{W,i,t+\Delta t} = T_{W,i,t} + \frac{dT_{W,i,t}}{dt} \cdot \Delta t \tag{26}$$

$$R_{W,i,V} = \frac{L / M}{k_w \cdot A_w} \tag{27}$$

The thermal network parameters on the PCM and Fins can be calculated based on the equations (28)-(35).

$$R_{P,i,j,R} = \begin{cases} \dfrac{M ln \frac{D_1}{D_0}}{2\pi L k_{eff}}; for\ i = 1 \\ \dfrac{M ln \frac{D_j}{D_{j-1}}}{2\pi L k_{eff}}; for\ i \geq 2 \end{cases} \tag{28}$$

$$R_{P,\,i,\,j,\,V}=\frac{L/M}{k_{eff} \times A} \tag{29}$$

$$\dot{Q}_{i,j,t,0} = \begin{cases} 0 & ; for\ i = 1 \\ \dfrac{T_{i-1,j,t} - T_{i,j,t}}{R_{P,i,j,V}} & ; for\ i \geq 2 \end{cases} \tag{30}$$

$$\dot{Q}_{i,j,t,1} = \begin{cases} \dfrac{T_{i,j,t} - T_{i,j+1,t}}{R_{P,i,j,V}}\ ; for\ i \geq 1 \\ \dfrac{T_{i,N,t} - T_{amb}}{R_{P,i,j,V}}; for\ i = N \end{cases} \tag{31}$$

$$\frac{dT_{i,j,t}}{dt} = \frac{\dot{Q}_{i,j,t,0} + \dot{Q}_{i,j,t,1} - \dot{Q}_{i+1,j,t,0} - \dot{Q}_{i,j+1,t,1}}{C_{i,j,t}} \tag{32}$$

$$T_{i,\,j,\,t+1}=T_{i,\,j,\,t}+\frac{dT_{i,\,j,\,t}}{dt} \times \Delta t \tag{33}$$

$$C_{PCM} = \begin{cases} C_s; & T < T_s \\ Cs + \dfrac{\Delta H}{T_{melt} - T_{sol}}; & T_s \leq T \leq T_l \\ C_l; & T > T_l \end{cases} \tag{34}$$

$$C_{i,\,j,\,t}=[\gamma\, C_{PCM}\, \rho_{PCM}+(1\text{-}\gamma)\, C_{FIN}\, \rho_{FIN}]\, V_{i,j} \tag{35}$$

Here, i denotes a specific segment vertically, j is radially and t denotes a specific time step. 0 and 1 are used to denote heat flow in vertical and radial direction respectively. Total volume of a PCM and fin segment is denoted by V, area of a segment is A, total height of the computational domain is L and W is the radial dimension in PCM and Fin domain. The domain is discretized into M x N segments. R, C, Q, T represent the thermal resistance, thermal capacitance, heat flow and temperature of a specific segment at time t respectively. PCM porosity is, γ, β represents the liquid fraction, ρ, the density, and k_{eff} is the effective thermal conductivity.

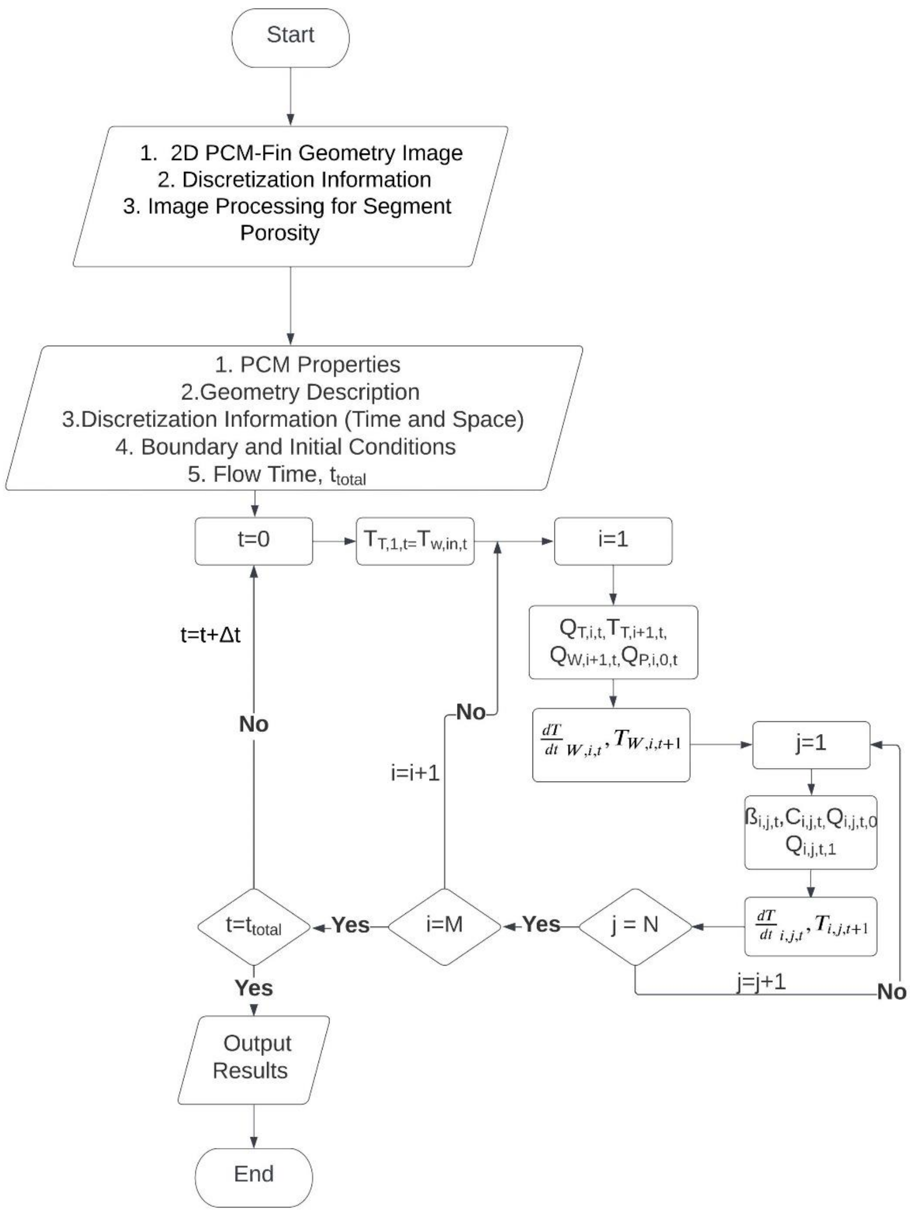

Figure 17: Solver Flowchart for the RCM for Annular Finned PCMHX

The explicit time marching formulation and the solver flowchart shown here are for the annular finned PCMHX. Similar explicit time marching formulation can be used for the other geometries. The changes in the equations and flowchart will be based on the boundary conditions, the discretization dimensions and porosity calculations. The detailed equations and individual solver flowcharts for the other geometries are shown in the Appendix.

Chapter 3 CFD Computational Efficiency and Effect of Thermophysical Properties

3.1 CFD Computational Cost Study

Straight tube PCMHX is a simple heat exchanger geometry which will be used to study the computational cost of CFD for a transient conjugate heat transfer problem for a simple geometry. Here, PCM in charging (melting) and discharging (solidification) processes will be simulated based on the process discussed on Section 2.1 to study the CFD prediction form PCM temperature profile and associated computational cost.

3.1.1 Subject of Study

Longeon et al. [20] presented a detailed experimental study of melting and solidification on a straight tube PCMHX (Figure 18a) which was used to validate the CFD model. The geometry specification from this study is provided in Table 5. The geometry was modeled as a conventional full-sized axisymmetric domain (Figure 18b) as it has been done extensively in the literature (e.g., Pu et al. [23] and Zhang et al. [106]). The temperatures at the three different thermocouples placed in the experimental setup [20] will be used to validate the model. Figure 18c shows the location of the thermocouples.

Table 5: Geometry Specifications

Dimension	Unit	Value
Tube Diameter - D_t	mm	15
Tube Wall Thickness - t	mm	2.5
Tube Length - L	mm	400
Tube Material	-	Stainless Steel
Container Diameter - D_c	mm	44

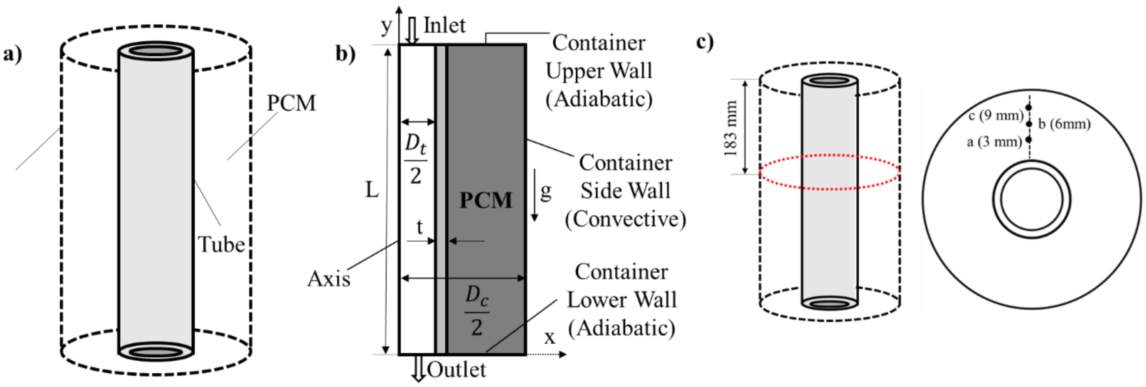

Figure 18: Schematic of a) Straight Tube PCM Embedded Heat Exchanger b) Computational Domain c) Thermocouple Positions

3.1.2 Model Details and Settings

The HTF is water, flowing from top to bottom, at different temperatures for melting and solidification processes. Paraffin RT35 by Rubitherm GmbH [91] is used as the PCM. The corresponding Reynolds number for the tube flow is 146 [20] and hence a laminar flow model was used. The uniform initial temperature conditions are 22 °C for melting and 40 °C for solidification. As seen from Figure 18b the upper and lower container walls are modeled as adiabatic and the left side of the container is used as an axis for the symmetry. Heat loss to ambient through container side wall is considered. An empirical correlation for natural convection was used to estimate a convective heat transfer coefficient between the container wall and the ambient [23] of 7.3 W/m^2-K. The ambient temperature is assumed constant at 30°C [20].

The settings for melting and solidification models are similar except the change in phase-change temperature range, water inlet temperature, and PCM initial temperature. The structured rectangular grids are used to discretize the computational domain as shown in Figure 19. A successful numerical melting model validation with the same experimental setup was found in literature [23] using a grid with 2.7 x 10^5 elements and a time step size of 0.1s. The same time and spatial discretization are used in this work. The PCM thermophysical properties, initial boundary conditions, and the general CFD settings used in this work are presented in Table 6.

Table 6: PCM Thermophysical Properties, Initial Boundary Conditions and CFD Settings

Property	Units	Method	Value(s)
Density	kg/m^3	Boussinesq	880
Specific Heat	kJ/kg- K	Piecewise Lin.	1.8(s)/ 2.4(l)
Thermal Conductivity	W/m-K	Constant	0.2
Viscosity	kg/m-s	Constant	0.0029
Thermal Expansion Coefficient	K^{-1}	Constant	0.001
Latent Heat	kJ/kg	Constant	157
Solidification Temperature Range	K	Constant	300.15-311.15
Melting Temperature Range	K	Constant	301.15-313.15
Initial Temperature - Melting	K	Constant	295.15
Water Inlet Temperature -Melting	K	Constant	325.15
Initial Temperature - Solidification	K	Constant	313.5
Water Inlet Temperature - Solidification	K	Constant	290.15
Ambient Temperature	K	Constant	303.15
Water Inlet Velocity	m/s	Constant	0.01

Settings	Value(s)
Pressure-Velocity Coupling	SIMPLE
Pressure Discretization Scheme	PRESTO!
Momentum Discretization Scheme	QUICK
Energy Discretization Scheme	QUICK
Continuity Convergence Criteria	10^{-5}
x-vel. Convergence Criteria	10^{-5}
y-vel. Convergence Criteria	10^{-5}
Energy Convergence Criteria	10^{-12}
Iterations per Time Step	40
Flow Regime Model	Laminar
Mushy Zone Parameter	10^6
Pressure Under Relaxation	0.3
Momentum Under Relaxation	0.7
Energy Under Relaxation	1

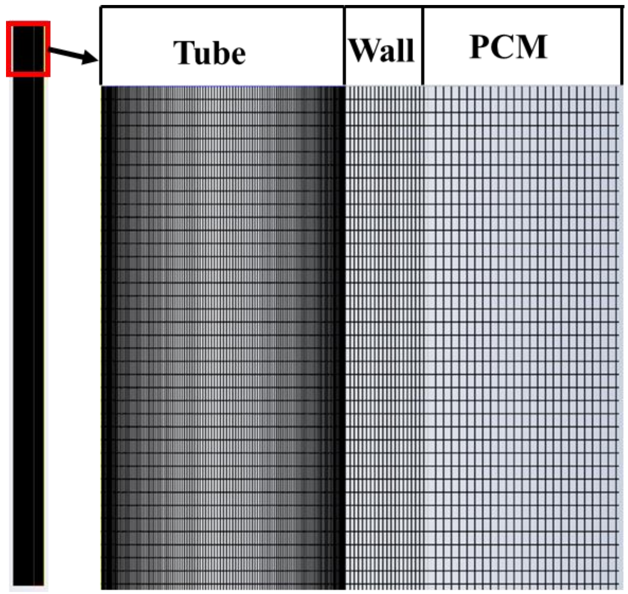

Figure 19: Structured rectangular grids in computational domain with a zoomed in version

3.1.3 Model Validation

Figure 20a show the temperature profile during melting at the thermocouple positions mentioned above for the first 6000s flow time. This is compared with the experimental results from Longeon et al. [20].

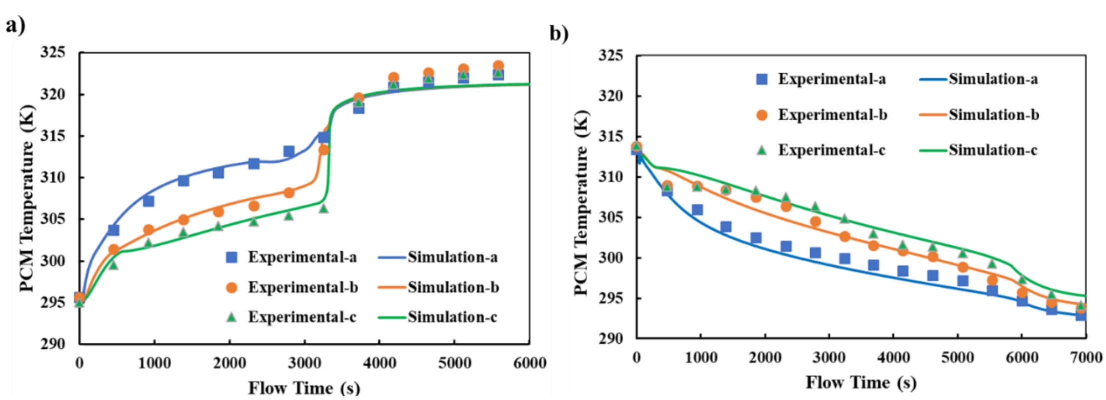

Figure 20: Comparison of Temperature Profile in a) Melting Model and b) Solidification Model with Experimental Results from Literature

It can be observed that the results of simulation agree well with the experimental results from literature. The deviation after 3000s can be attributed to the unknown angular position of the thermocouples and the overestimation of heat loss to the ambient. Figure 20b shows the temperature profile during solidification for the thermocouple positions for the first 7000s. The thermocouple positions are same as the positions in melting model. This is compared with the experimental results from Longeon et al. [20]. It is evident that the results are in very good agreement with the experimental data. The predicted PCM temperature profile in both the models agrees well within 2K over time compared to the experimental data.

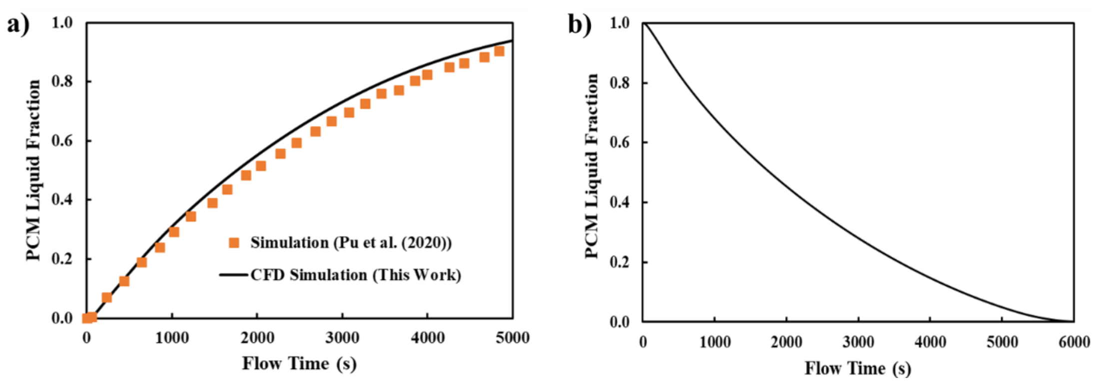

Figure 21: a) Comparison of Liquid Fraction in Melting Model with Numerical Results from Literature, b) Liquid Fraction in Solidification Model

Figure 21a shows that the average liquid fraction of PCM compared to numerical results from Pu et al. [23] for the same case. Figure 21b shows the average liquid fraction over time for the solidification model.

Figure 22 shows the comparison of experimental and predicted outlet temperature of water in models for melting and solidification. The prediction of outlet water temperature matches very closely in solidification process compared to the melting process. In the melting process the deviation from experimental outlet temperature increases over time. This can be attributed to overestimation of heat loss to the ambient. With time, the temperature of PCM increases in the model and this increases the amount of heat loss. Compared to the melting model, the temperature difference between PCM and ambient was lower in solidification process which results in lower heat loss.

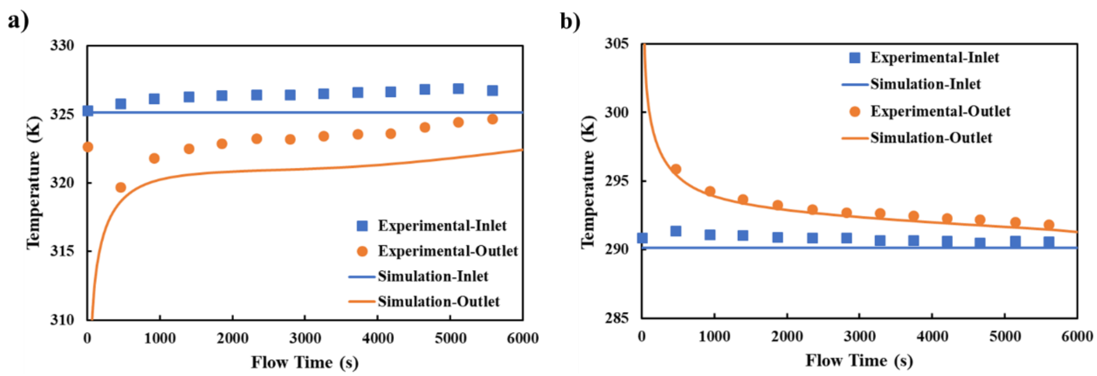

Figure 22: Comparison of Experimental and Numerical Water Inlet and Outlet Temperature for a) Melting b) Solidification

Figure 23 shows the comparison of experimental and numerical heat flow rate of water for melting and solidification process. The experimental heat flow rate was calculated assuming a constant flow rate based on the average velocity from Longeon et al. [20]. The deviation of heat flow from the experiments is higher in the melting model because of higher deviation in outlet temperature prediction as shown in Figure 5a. But overall, both the models show similar trend in heat flow rate when compared to the experimental results.

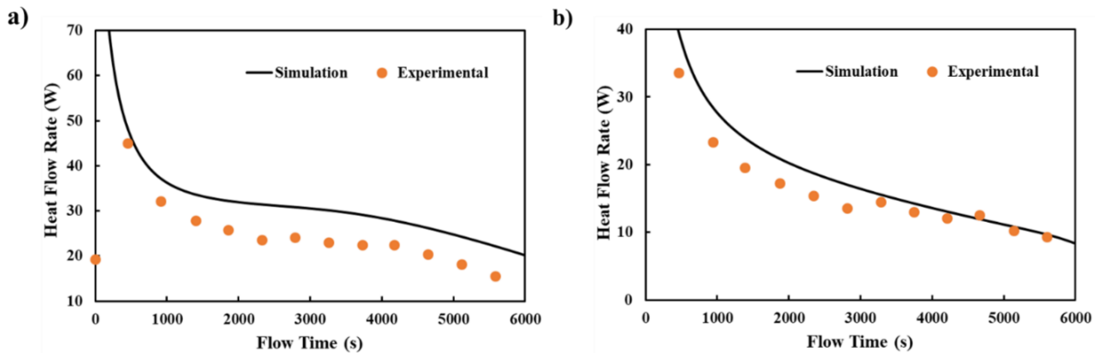

Figure 23: Comparison of Experimental and Numerical Water Heat Flow Rate for a) Melting, b) Solidification

3.1.4 Computational Cost

Table 7 summarizes the hardware information and the computational cost. The solidification model took approximately half the time to simulate first 6000s of flow time compared to the melting model. During the solidification, the mode of heat transfer from the tube wall to PCM is mainly conduction as the PCM near the tube wall solidifies first. With time, PCM around the container begins to solidify and amount of liquid PCM reduces. In case of melting, the heat transfer from the tube wall to the PCM is a combination of both conduction and natural convection due to the motion of liquid

Table 7: Hardware Information and Computational Cost

<table>
<tr><th colspan="4">Hardware</th></tr>
<tr><th>No. of Cores</th><th colspan="2">Processor</th><th>RAM (GB)</th></tr>
<tr><td>28</td><td colspan="2">2 x Intel® Xeon® Gold 5117, 2.00 GHz</td><td>96</td></tr>
<tr><th colspan="4">Computational Cost</th></tr>
<tr><th>Model</th><th>Flow Time (s)</th><th>Computation Time (h)</th><th>α</th></tr>
<tr><td>Melting</td><td>6000 (Full)</td><td>105</td><td>63</td></tr>
<tr><td rowspan="2">Solidification</td><td>6000 (First)</td><td>50</td><td>30</td></tr>
<tr><td>7000 (Full)</td><td>56</td><td>28.8</td></tr>
</table>

PCM near the tube wall. The effect of natural convection can be significant for this geometry as the liquid PCM can flow in the annular space due to buoyancy. The table also shows the real-time factor (RTF) which is the ratio between simulated time and simulation time required for the model. The RTF shows that even though CFD can predict the temperature profile and melting time accurately, it can take 63 times longer for melting and approximately 30 times longer to simulate compared to the actual experimental results.

3.2 Effect of Thermal Expansion Coefficient, Viscosity and Melting Range in CFD Simulation

It was shown in Table 4 that the reported values of β and μ as reported in different literatures are inconsistent and can vary by an order of magnitude. Compared to the other thermophysical properties, the values of β, μ and melting ranges are not often mentioned in the manufacturer datasheet. Here, CFD-based models for two PCMHX domains - with and without fins – are studied to find the impact of β, μ and melting range temperature on the PCM temperature profile and melting time. The role that heat source temperature plays in the deviation caused by using uncertain thermophysical properties is also investigated here.

3.2.1 Subject of Study

In section 3.1, the numerical model for melting in a straight tube PCMHX has been discussed and the results agree well with the experiment. However, using thermophysical data from Ebadi et al. [89] , the model would have not been validated as well as it did when data from Pu et al. [23] was used since there is significant difference between the thermophysical data of PCM reported in these two sources

(Table 4). There is always uncertainty involved when reliable source for a thermophysical data is not present and the range of that uncertainty needs to be studied.

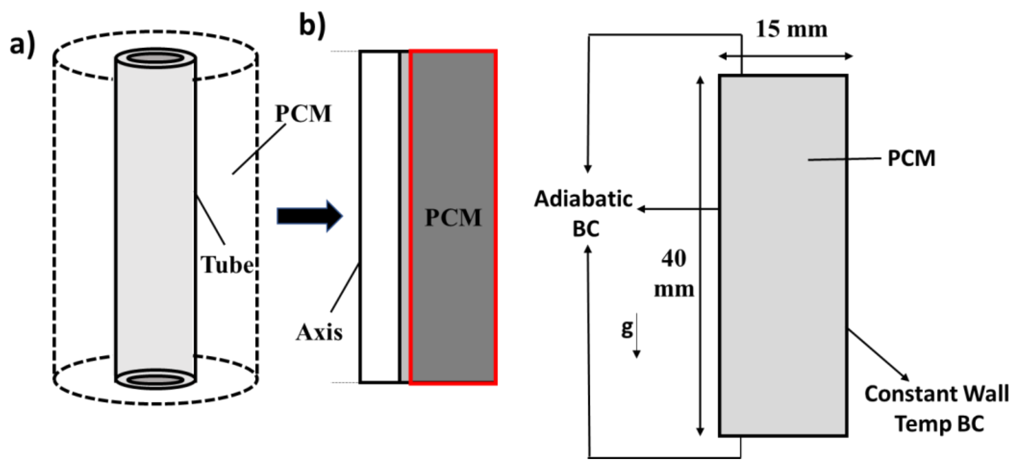

Figure 24: Non-Finned Domain A) Physical Model B) Computational Domain

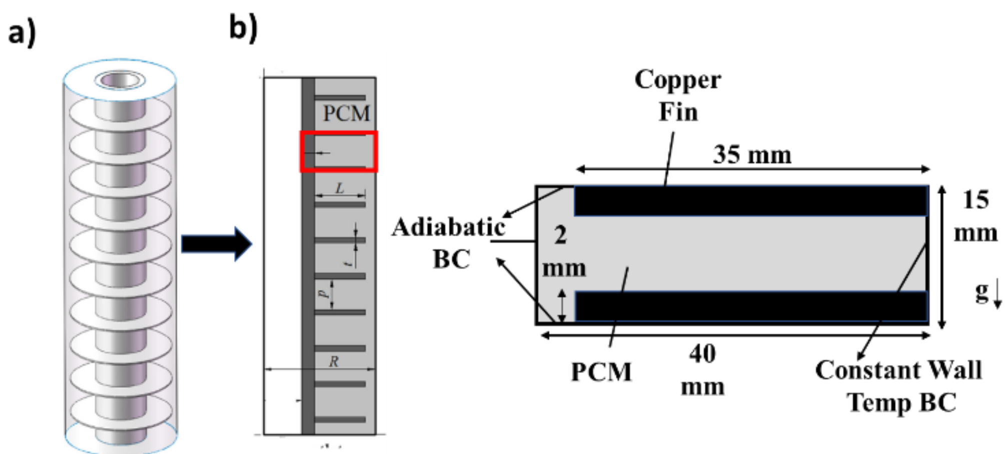

Figure 25: Finned Domain A) Physical Model B) Computational Domain

Unlike non-finned domains, the PCM flow can get obstructed in the finned which reduces the natural convection. As the latter also depends on thermophysical properties, it is necessary to check if there is any difference in the impact of the thermophysical properties between these two domain types which were investigated in this study (Figure 24 and Figure 25).

3.2.2 Model Details and Settings

Both the computational domains are 2D axisymmetric. The non-finned domain is a 40 mm x 15 mm rectangular section, while the finned one is a part of the annular finned PCMHX. It has been shown by Bacellar et al. [31] that for structured surface with fins, reduced domains reproduces the same behavior as full domain at approximately half the computational cost. The annular fins have a diameter of 70 mm, thickness of 4 mm, and fin pitch of 15 mm. The ratio between fin pitch and diameter is less than 0.25, which can be considered as small fin pitch. The finless domain may be considered a case with very large fin pitch; therefore, we are addressing both extremes. Both the tube and the fin are copper.

Both models have constant temperature boundary condition on the tube wall. The wall temperature for this study was 100°C but other wall temperatures were used in a separate study presented at a later subsection in this manuscript to verify consistency in the results. All the other walls in the domain were set as adiabatic. The initial temperature for the simulation was 26°C. Natural convection is taken into consideration during PCM melting process using Boussinesq approximation. The flow of liquid PCM is considered laminar since viscous forces play a major role as it will be discussed further. Structured rectangular grids are used to discretize the computational domain, and a time step size of 0.1s was used. General CFD settings used in this work are presented in Table 8.

Table 8: Thermophysical Properties of RT35 Used for the Study

Constant value properties			
Property	**Units**	**Method**	**Value(s)**
Density	kg/m^3	Boussinesq	880
Specific Heat	kJ/kg-K	Piecewise Linear	1.8(solid)/2.4(liquid)
Thermal Conductivity	W/m-K	Constant	0.2
Properties for sensitivity analysis			
$\boldsymbol{\beta}$ **(1/K)**	**Source**	$\boldsymbol{\mu}$ **(kg/m-s)**	**Source**
0.0006	[89]	0.0029	[91]
0.001	[91]	0.01295	-
0.0026	[107]	0.023	[89]

A parametric study consisting of a combination of threes values of β, μ and melting range, was conducted. Two values of β were taken from the literature and using an equation from Schimmelpfennig et al.[107], a third value for β was estimated. The equation requires the density of liquid PCM in two different temperatures, however, from the manufacturer provided data there are only density of PCM in two different phases.

Using these density values, β is likely to be overestimated since the expansion only occurs, in practice, in the liquid phase. Two of the values of μ are taken from the literature and the third is the average of the two. Three melting ranges with a nominal melting temperature of 34°C were considered. The remaining thermophysical properties were taken from Pu et al. [23] .

3.2.3 Effects of Thermal Expansion Coefficient

For each μ and melting range values while parameterizing β resulted in 27 cases for each non-finned and finned domain. The results are summarized in Table 9.

Table 9: Effect of Thermal Expansion Coefficient in Melting Time

Case No.	MR (°C)	μ (kg/m-s)	β (1/K)	Non-Finned Melting Time (s)	Dev (%)	Finned Melting Time (s)	Dev (%)
1	28-40	0.0029	0.0006	532	*	231	*
4			0.001	465	-12.6	204	-11.7
7			0.0026	356	-33.1	174	-24.7
2		0.01295	0.0006	707	*	290	*
5			0.001	628	-11.2	260	-10.3
8			0.0026	492	-30.4	210	-27.6
3		0.023	0.0006	795	*	321	*
6			0.001	703	-11.6	286	-10.9
9			0.0026	553	-30.4	230	-28.3
10	30-38	0.0029	0.0006	530	*	229	*
13			0.001	464	-12.5	202	-11.8
16			0.0026	354	-33.2	173	-24.5
11		0.01295	0.0006	715	*	291	*
14			0.001	634	-11.3	260	-10.7
17			0.0026	497	-30.5	209	-28.2
12		0.023	0.0006	795	*	323	*
15			0.001	709	-10.8	288	-10.8
18			0.0026	561	-29.4	234	-27.6
19	32-36	0.0029	0.0006	528	*	227	*
22			0.001	460	-12.9	200	-11.9
25			0.0026	352	-33.3	172	-24.2
20		0.01295	0.0006	727	*	294	*
23			0.001	644	-11.4	264	-10.2
26			0.0026	502	-30.9	210	-28.6
21		0.023	0.0006	794	*	328	*
24			0.001	725	-8.7	293	-10.7
27			0.0026	573	-27.8	236	-28.0

* - Compared against this value

The change in β can significantly impact the melting rate in all the cases; for all combinations of μ and melting range, the deviation after increasing β is similar. Increasing the thermal expansion coefficient impacts, the volume expansion rate of the liquid PCM which can considerably increase melting rate. For the finned and non-finned domains, significant difference in the deviation for increasing β is not found in almost all the cases. The exceptions are for cases 7,16,25, in which, the lowest value of μ and the highest value of β were used, and hence, the heat transfer through natural convection is the highest. This can be seen from Table 9 as the corresponding melting time is the lowest for these three cases. But in the finned domain, when the flow of the liquid PCM is obstructed, the maximum impact of the highest natural convection for these cases is not realized as much as seen from the non-finned cases. This leads to the significant deviation between finned and non-finned domains for these three cases.

Figure 26 shows the average PCM temperature profile of some sample cases for both finned and non-finned domains. For the non-finned domain, the temperature deviation due to increase of β is higher than the finned cases. Temperature profiles of PCM is often used to validate models against experimental data and this figure shows the importance using accurate value of β for model validation purposes, especially if the domain is not finned.

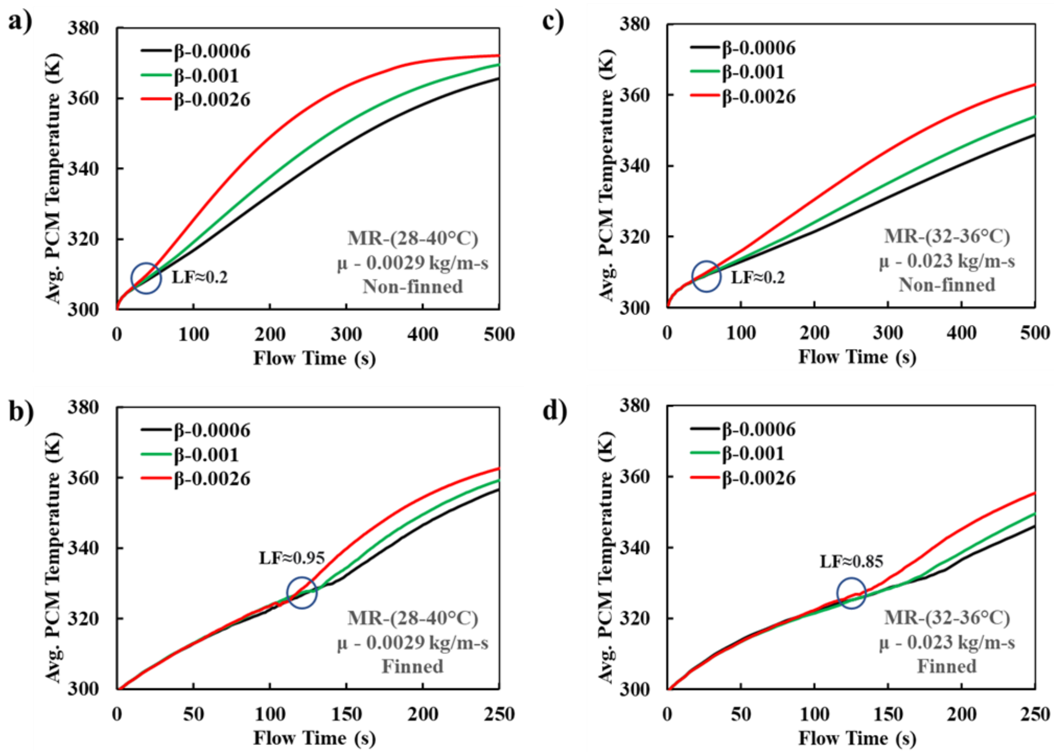

Figure 26: Effect of Thermal Expansion Coefficient in Average PCM Temperature Profile, For Case (1,4,7) A) Non-Finned B) Finned; For Case (21,24,27) C) Non-Finned D) Finned

Figure 26 shows the average PCM temperature profile of some sample cases for both finned and non-finned domains. For the non-finned domain, the temperature deviation due to increase of β is higher than the finned cases. Temperature profiles of PCM is often used to validate models against experimental data and this figure shows the importance using accurate value of β for model validation purposes, especially if the domain is not finned.

The local temperature deviation in the PCM for using inaccurate values of β can be much higher than the average temperature. The plot also displays the liquid fraction when the temperature profile starts to deviate. For the non-finned domain, the temperature profile starts deviating quite early in the melting process. For the finned domain, the deviation starts when the PCM is close to fully melted since conduction is the dominant heat transfer mode near the fin walls, and hence the effect of β is less pronounced.

3.2.4 Effects of Viscosity

Table 10 summarizes the results from the 27 cases and shows the impact of changing viscosity with different values of β and melting range. The case studies are same as Table 9 but this table is presented in a way to visualize the effects of viscosity.

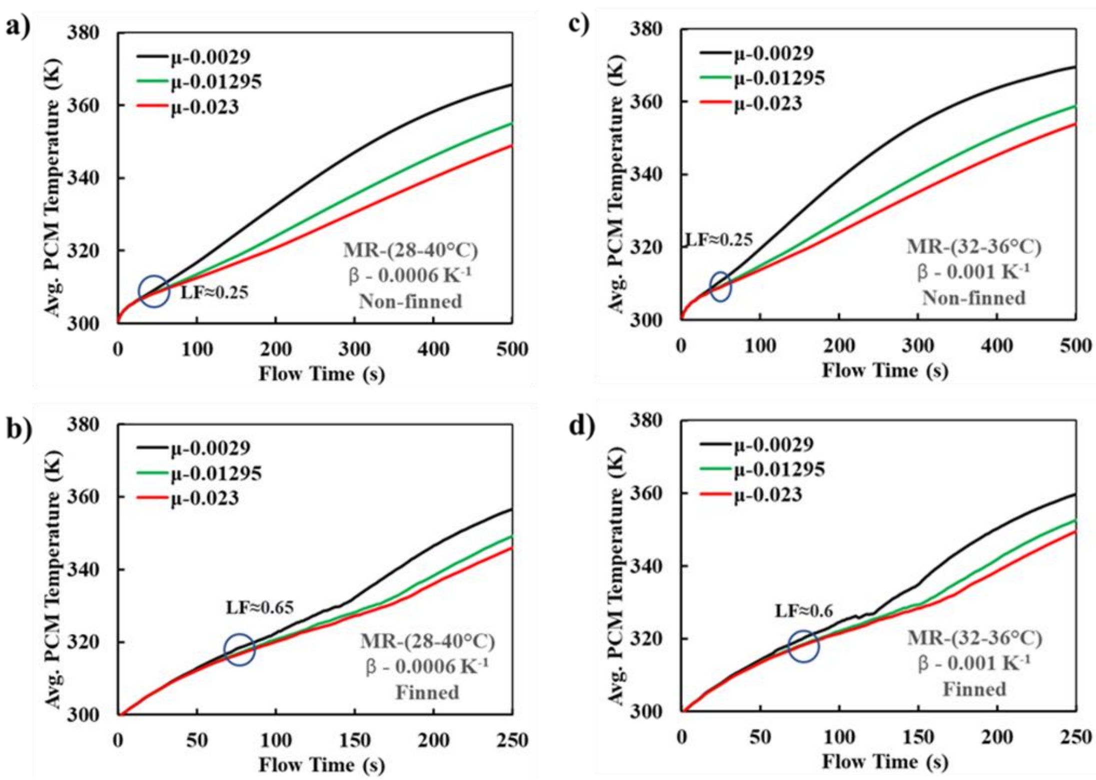

Figure 27: Effect of Viscosity in Average PCM Temperature Profile, For Case (1,2,3) A) Non-Finned B) Finned; For Case (22,23,24) C) Non-Finned D) Finned

A variation in μ can significantly impact the melting rate in all the cases. When the viscosity is increased, the flow of the liquid PCM is also increased and thus reducing the natural convection and increasing the melting time. The deviation due to change in

μ is higher compared to the previous section when we changed β. This can happen because the magnitude of difference between the three values were higher for viscosity.

Table 10: Effect of Viscosity in Melting Time

Case No.	MR (°C)	β (1/K)	μ (kg/m-s)	Non-Finned Melting Time (s)	Dev (%)	Finned Melting Time (s)	Dev (%)
1	28-40	0.0006	0.0029	532	-	231	-
2			0.01295	707	32.9	290	25.5
3			0.023	795	49.4	321	39.0
4		0.001	0.0029	465	-	204	-
5			0.01295	628	35.1	260	27.5
6			0.023	703	51.2	286	40.2
7		0.0026	0.0029	356	-	174	-
8			0.01295	492	38.2	210	20.7
9			0.023	553	55.3	230	32.2
10	30-38	0.0006	0.0029	530	-	229	-
11			0.01295	715	34.9	291	27.1
12			0.023	795	50.0	323	41.0
13		0.001	0.0029	464	-	202	-
14			0.01295	634	36.6	260	28.7
15			0.023	709	52.8	288	42.6
16		0.0026	0.0029	354	-	173	-
17			0.01295	497	40.4	209	20.8
18			0.023	561	58.5	234	35.3
19	32-36	0.0006	0.0029	528	-	227	-
20			0.01295	727	37.7	294	29.5
21			0.023	794	50.4	328	44.5
22		0.001	0.0029	460	-	200	-
23			0.01295	644	40.0	264	32.0
24			0.023	725	57.6	293	46.5
25		0.0026	0.0029	352	-	172	-
26			0.01295	502	42.6	210	22.1
27			0.023	573	62.8	236	37.2

Unlike the previous section, here the impact on finned cases is significantly lower compared to the non-finned cases. This can be explained by the fact that the fins impose a flow resistance reducing the freedom of motion of the liquid PCM, therefore minimizing the buoyancy effects. From the table it can also be seen that, for higher value of β, the deviation between the melting time increases compared to the lower values.

Figure 27 shows the average PCM temperature profile for some sample cases for finned and non-finned domain when different values of μ are used. Like in the previous section, for the non-finned domain, the temperature deviation is higher than the finned cases. However, unlike in the previous section, the deviation of temperature does not start at the end of the melting process, rather it starts in the middle of the process. The lower viscosity reduces flow resistance allowing the liquid PCM to move more freely, thus contributing to an enhanced heat transfer as supported by the higher temperature values observed.

3.2.5 Effects of Melting Range

Table 11 summarizes the results from the 27 cases and shows the impact of changing MR with different values of β and μ. The table shows that change in MR did not significantly impact the melting time for any of the cases for both finned and non-finned domain. This finding can be useful as it can lead to less uncertainty while performing future CFD simulation tasks by not requiring the accurate knowledge of PCM MR.

Table 11: Effects of Melting Range

Case No.	β (1/K)	μ (kg/m-s)	MR (°C)	Non-Finned Melting Time (s)	Dev (%)	Finned Melting Time (s)	Dev (%)
1	0.0006	0.0029	28-40	532	-	231	-
10			30-38	530	-0.4	229	-0.9
19			32-36	528	-0.8	227	-1.7
2		0.01295	28-40	707	-	290	-
11			30-38	715	1.1	291	0.3
20			32-36	727	2.8	294	1.4
3		0.023	28-40	795	-	321	-
12			30-38	795	0.0	323	0.6
21			32-36	794	-0.1	328	2.2
4	0.001	0.0029	28-40	465	-	204	-
13			30-38	464	-0.2	202	-1.0
22			32-36	460	-1.1	200	-2.0
5		0.01295	28-40	628	-	260	-
14			30-38	634	1.0	260	0.0
23			32-36	644	2.5	264	1.5
6		0.023	28-40	703	-	286	-
15			30-38	709	0.9	288	0.7
24			32-36	725	3.1	293	2.4
7	0.0026	0.0029	28-40	356	-	174	-
16			30-38	354	-0.6	173	-0.6
25			32-36	352	-1.1	172	-1.1
8		0.01295	28-40	492	-	210	-
17			30-38	497	1.0	209	-0.5
26			32-36	502	2.0	210	0.0
9		0.023	28-40	553	0.0	230	0.0
18			30-38	561	1.4	234	1.7
27			32-36	573	3.6	236	2.6

Figure 28 shows the average PCM temperature profile for some sample cases for finned and non-finned domains with minimal deviation among the different MR's. This, however, may have been masked by the fact that a large temperature difference was used. The next section presents a more detailed analysis introducing the effect of temperature potential.

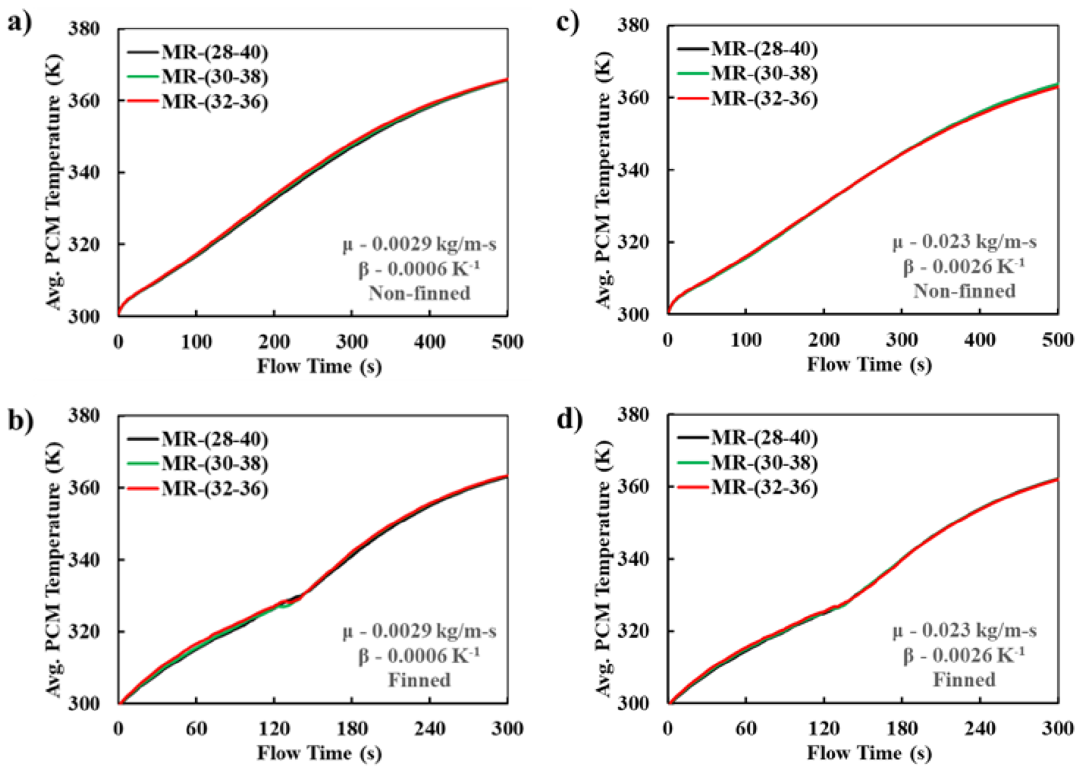

Figure 28: Effect of MR in Average PCM Temperature Profile, For Case (1,2,3) A) Non-Finned B) Finned; For Case (22,23,24) C) Non-Finned D) Finned

3.2.6 Effects of Wall Temperature

Wall temperature of 100^{o}C can be considered high therefore additional cases with lower wall temperature were investigated. These cases were only performed for the finned domain. Table 12 summarizes the result for a lower and higher wall temperature for different values of β and μ. The result shows that, the lower wall temperature did not show much different results compared to what was obtained before for change of β, but it showed significant change for μ. For lower wall temperature, the deviation of melting time due to increase of μ is reduced. The reduction of approach temperature has greater impact in the viscous forces compared to the buoyancy forces. This study, however, was only performed for the finned cases and the results may differ for non-finned cases where PCM can flow more freely. When the temperature gradient is lower, the impact in the thermal characteristics is also lower because the viscous effect is reduced.

Table 12: Effect of Wall Temperature in Melting Rate Deviation

Case No.	MR (°C)	μ (kg/m-s)	β (1/K)	Wall Temp-45°C		Wall Temp-100 °C	
				Melting Time(s)	Dev (%)	Melting Time(s)	Dev (%)
1	28-40	0.0029	0.0006	1327	--	231	-
4			0.001	1180	-11	204	-12
7			0.0026	982	-25.9	174	-24.7
4	28-40	0.0029	0.001	1180	-	204	-
5		0.01295		1383	17.2	260	27.5
6		0.023		1478	25.2	286	40.2

Table 13: Effect of Wall Temperature in Melting Rate Deviation Caused by Different Melting Ranges

µ-0.0029 (kg/m-s) β-0.001 (1/K)		Wall Temp-45°C		Wall Temp-65°C		Wall Temp-100 °C	
Case No.	MR(°C)	Melting Time(s)	Dev (%)	Melting Time(s)	Dev (%)	Melting Time(s)	Dev (%)
4	28-40	1180	-	408	-	204	-
13	30-38	1102	-6.6	402	-1.5	202	-1
22	32-36	1065	-9.8	403	-1.2	200	-2

Table 13 summarizes the result for effect of three different wall temperature in the impact for change in melting range. The result shows that for both the high and medium wall temperature, change in melting rate do not have any effect in the melting time. However, for the low wall temperature the deviation in melting time is significant. This shows that when the temperature difference between the heat source and the nominal temperature of PCM is close, the selection of melting range becomes significant.

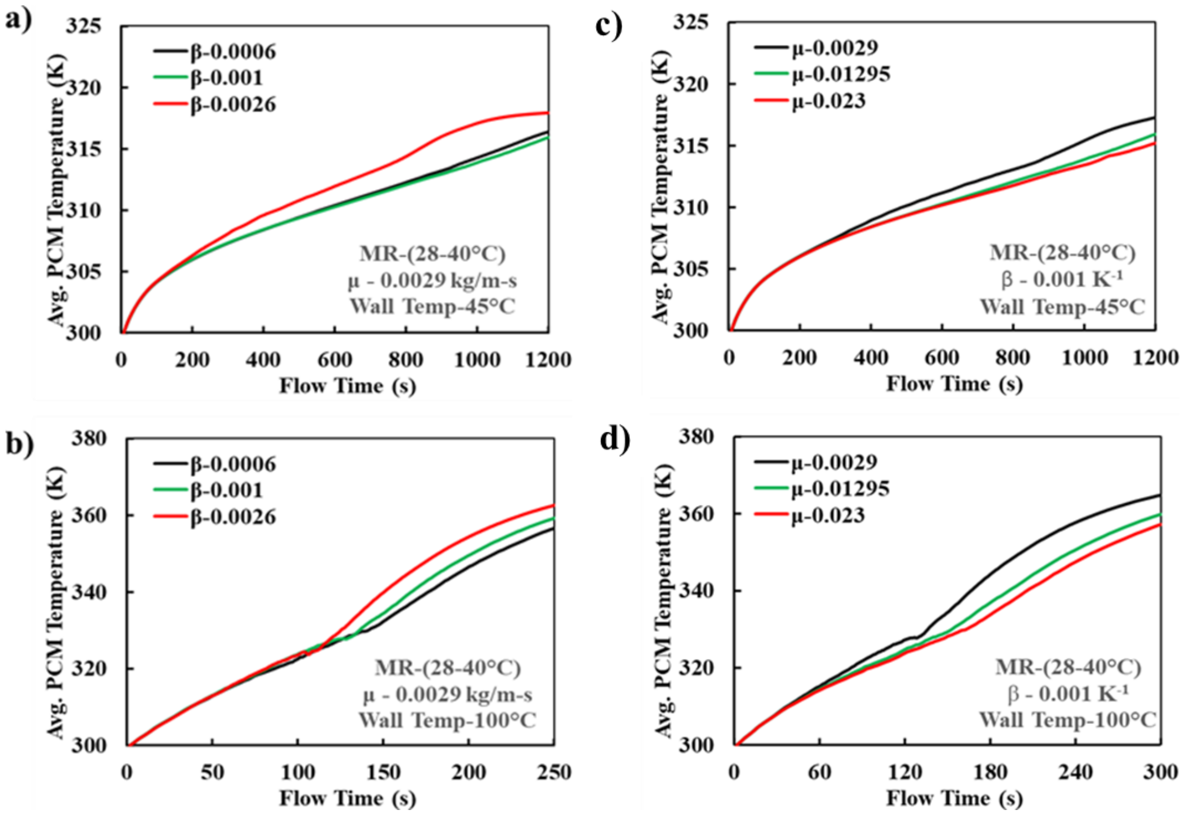

Figure 29: a), b) Effect of Wall Temperature in Deviation Caused by Thermal Expansion Coefficient, For Case (1,4,7); c), d) Effect of Wall Temperature in Deviation Caused by Viscosity, For Case (4,5,6)

Figure 29 shows the effect of wall temperature in the PCM temperature profile deviation caused by different values of β and μ respectively. For the higher wall temperature, effect of change of μ is higher than the lower wall temperature.

The change in values for β and μ showed a significant impact on the melting time prediction. Using different μ and β values from literature resulted in a deviation of up to 57.6% and 12.9% respectively for the non-finned domain. For the finned domain, the effect of μ is comparatively lower (46.5%) while the effect of β is found similar (11.9%) when compared to the non-finned domain.

The study highlights the challenges imposed by the inaccurate knowledge of μ and β for accurate prediction of PCMHX temperature profile and melting time with

CFD. β and μ are part of the momentum source term in the momentum equation solved in CFD and is required to model the transition between solid and liquid phase. For the simulation of different PCMs available in the market, CFD can be restrictive. In this work for rapid simulation tool and optimization framework development, focus was given on geometries where the momentum equations are not required to be solved and thus simplified model like RCM can be created for the accurate prediction in PCMHX.

Chapter 4 RCM Validation and Comparison with CFD

4.1 RCM for PCM Embedded in Porous Media

To the best of the author's knowledge, no study has previously utilized RCM to model composite PCM with metal foam. In section 2.2, the approach of developing a computationally inexpensive RCM for the melting of PCM embedded in metal foam supplied with constant heat flux has been discussed. Here, the model validation against experimental data from literature and then comparison against a validated CFD model will be discussed. The prediction difference in local temperature profile, energy storage, and melting time between the two models is discussed in this section along with the respective computational costs.

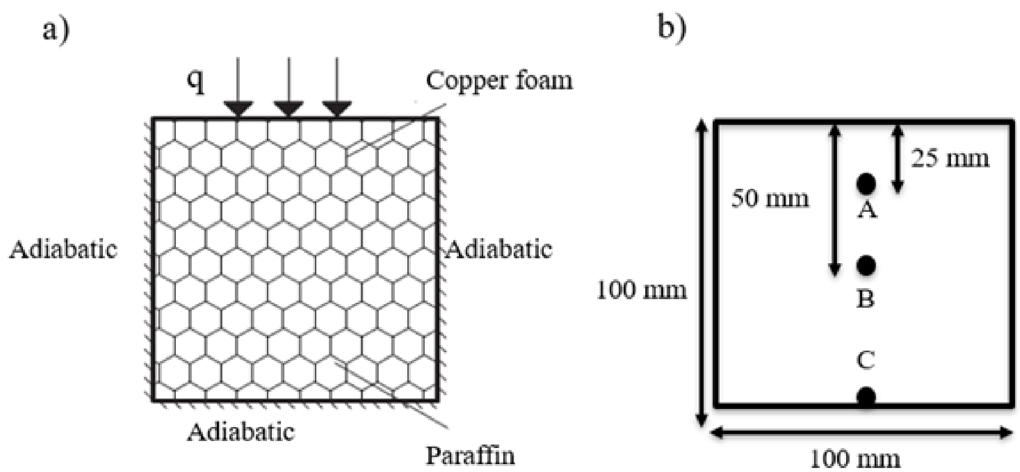

Figure 30: a) Composite PCM Setup with Metal Foam [55] **b) Thermocouple Positions**

4.1.1 Subject of Study

Melting in paraffin-based PCM impregnated with copper, the foam has been tested experimentally by Zheng et al.[55]. The composite PCM of porosity (ratio of PCM volume and total volume) 0.95 was utilized in the melting experiment. The metal foam pore size was 5 Pores Per Inch (PPI). Figure 30a show the composite PCM with the dimension of 100×100×30 mm. It was heated with a 100×10×30 mm electrical heater attached to the top of the PCM enclosure, which provided constant and uniform heat flux. All the other walls are considered adiabatic in the model. Three thermocouples A, B & C were placed at 25, 50, and 100 mm away from the heated wall respectively, as shown in Figure 30b. The thermophysical properties of PCM and copper foam are provided in Table 14.

Table 14: Thermophysical Properties of PCM and Copper Foam [55]

Properties	Paraffin	Copper Foam
k (W/m-K)	0.3	380
ρ (kg/m^3)	900	8900
c_p (J/kg-K)	2300	386
T_{sol} - T_{melt} (K)	323-331	-
ΔH (J/kg)	148,800	-
μ (Pa-s)	0.00324	-
β (K^{-1})	0.0005	-

4.1.2 Details and Settings of the Models

A 2D numerical simulation was carried out in ANSYS Fluent and the method has been discussed in the previous section. Structured grid was used to discretize the computational domain, containing 10,000 elements as shown in Figure 31. Time step size was fixed in 0.5s based on a similar CFD study by Zhang et al.[28]. The initial temperature was 287K and a constant heat flux (1150W/m^2) was applied on the top wall. All the other walls were assumed adiabatic. The effective thermal conductivity was calculated (2.28 W/m-K) from the equations provided by Esapour et al. [16]. The mushy

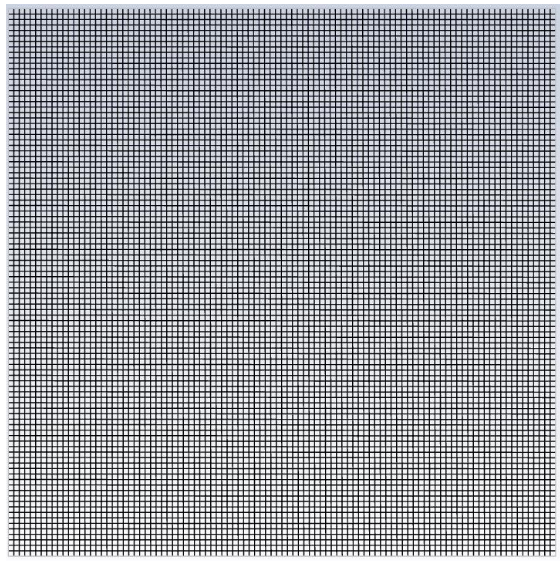

Figure 31: Structured Rectangular Grid of the Computational Domain

zone parameter was selected as 10^5 and 30 iterations per time step were used. The other CFD settings are provided in Table 15.

Table 15: CFD Settings for Melting in Composite PCM With Metal Foam

Pressure-Velocity Coupling	**Transient Formulation**	**Momentum Discretization Scheme**	**Energy Discretization Scheme**
SIMPLE	2nd order implicit	2nd order upwind	2nd order upwind
Pressure Discretization Scheme	**x, y-velocity Convergence Criteria**	**Continuity Convergence Criteria**	**Energy Convergence Criteria**
PRESTO!	10^{-5}	10^{-5}	10^{-12}

RCM approach discussed in section 2.2 is used to develop the reduced order model for this geometry. Figure 32 and Figure 33 show the grid size and the time step independency of RCM, respectively. Other than one very large segment size number, all the other grid sizes show the similar result. We use 10 segments and 2s time step size in this work.

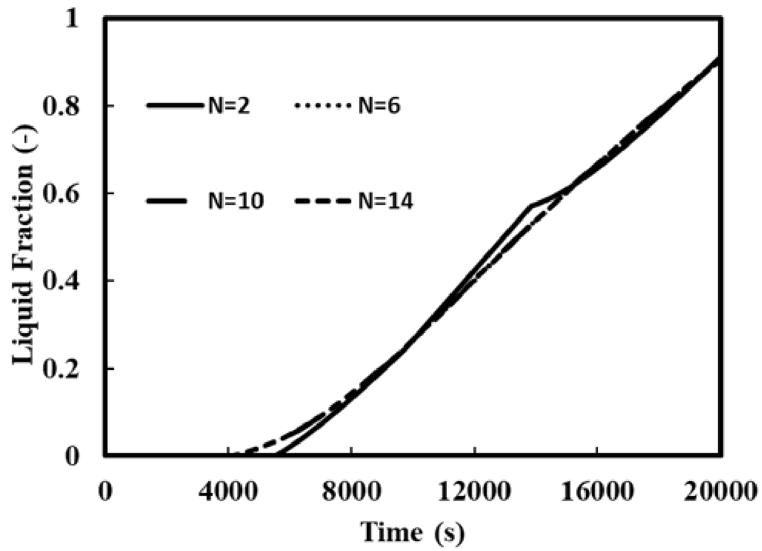

Figure 32: Grid Independence Analysis

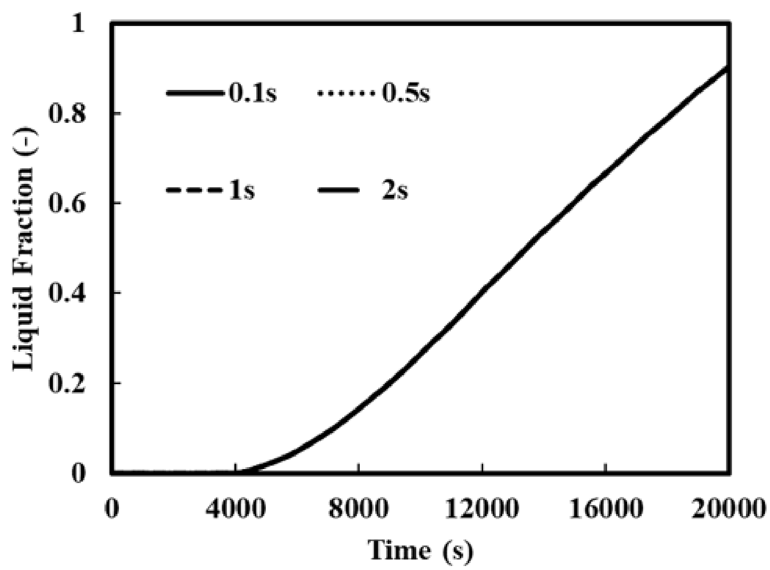

Figure 33: Time Step Independence Analysis

4.1.3 Model Validation

The temperature profile in points A and C for experiment and CFD simulation have been compared with RCM results in Figure 34. The plots show that the RCM results are matching very well with both the experimental and CFD results. The mean deviations of CFD and experimental temperature are found to be 1.62K and 2.97K for thermocouples A and C, respectively. For RCM and experimental temperature, the mean deviations are 1.84K and 2.96K for thermocouples A and C, respectively. The plots validate both CFD and RCM for the composite PCM.

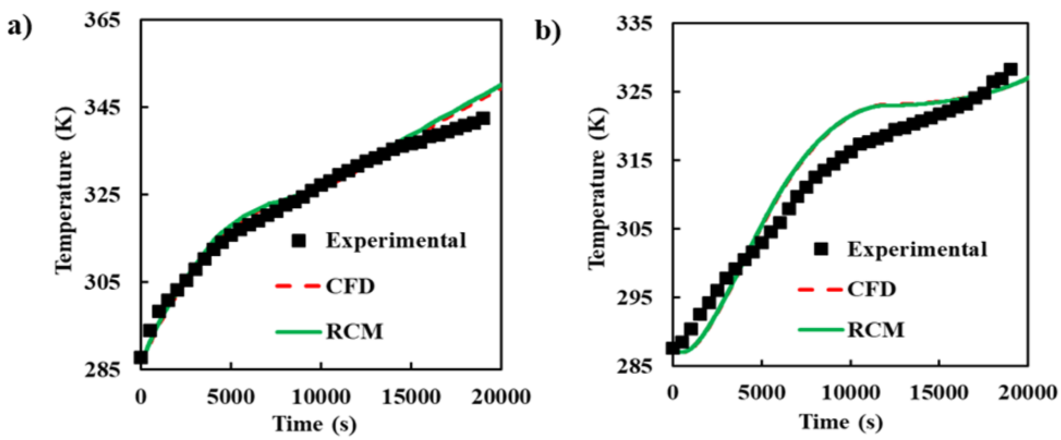

Figure 34: Comparison of RCM results with experiment and CFD for a) thermocouple A (TC-A) b) thermocouple C (TC-C)

The deviation in the predicted temperature for TC-C is higher in both RCM and CFD compared to TC-A as shown in Figure 34. This can be attributed to the adiabatic wall condition assumed in the model although there is heat loss to the ambient in the experiment. The hypothesis is that at the beginning of the simulation when the PCM temperature is lower (below ambient), the model is not considering the heat gain from ambient and so it is underpredicting the temperature. Once the PCM temperature rises higher than the ambient, the model is does not consider the heat loss and so overpredicts the temperature.

Figure 35 shows the comparison of RCM results with CFD results for average PCM temperature and liquid fraction. The plots show that the results from RCM are matching almost exactly with CFD.

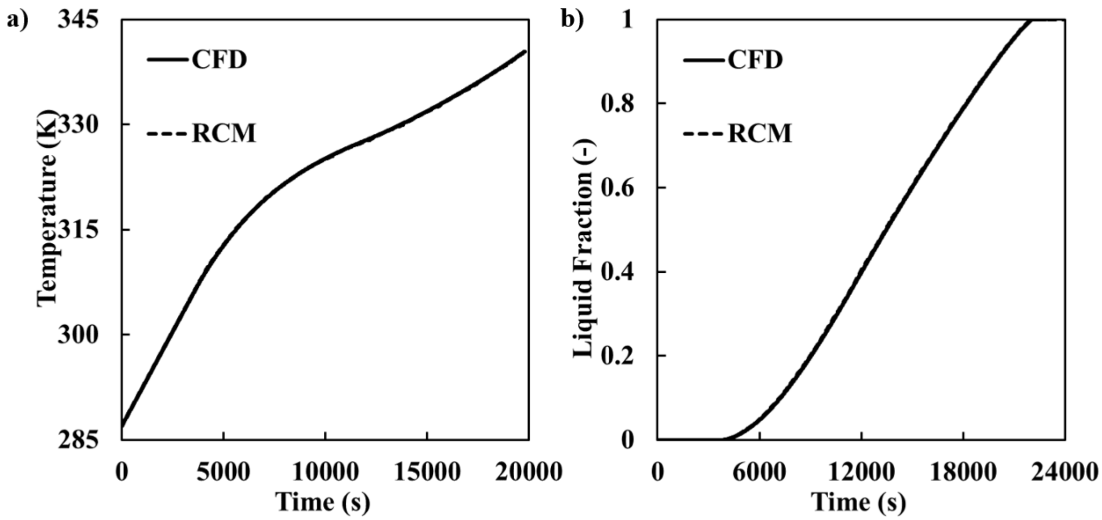

Figure 35: Comparison of RCM results with experiment and CFD for a) average PCM Temperature b) Liquid Fraction

4.1.4 Computational Cost and Accuracy Comparison

Table 16 compares computational cost and accuracy of melting time, energy storage, and local temperature prediction between RCM and CFD. Here, the real-time factor is the ratio between the time required for simulation and experimental time and is denoted by α. The results for RCM are based on 0.5s time step to compare against CFD results with same time step. However, with a higher time step size of 2s, the model is also similarly accurate with even lower computational cost. (Figure 33)

Table 16 shows that, both CFD and RCM predicted the energy storage with a deviation of around 0.8% when compared to experimental energy storage. In both CFD and RCM, the time needed for liquid fraction to go to 1 is considered as melting time. Ensuring this is difficult in an experimental study and it is possible to visually consider a case fully melted before it completely melts. The table also demonstrates that, with a deviation of less than 1%, the RCM can predict the melting time similar to CFD with 10^5 order of speed gain.

Mean absolute temperature deviation is denoted by σ_{Temp} and temperature deviation factor is denoted by σ_F. Here, we will introduce a cost-effectiveness index (CEI) to compare the tradeoff between different models for transient simulations. The index will be calculated based on equation (39). If the deviation between two models is considered acceptable, then the lower the value of CEI is for a model, the better its performance.

$$\sigma_{Temp} = \frac{\sum_{n=1}^{n} |T_{exp,t} - T_{sim,t}|}{n} \tag{36}$$

$$n = \frac{a - b}{\Delta t} \tag{37}$$

$$\sigma_F = \frac{\sigma_{Temp}}{T_{max} - T_{min}} \tag{38}$$

$$CEI = \frac{1}{\alpha x \sigma_f} \tag{39}$$

For temperature prediction at point A, the CEI for CFD is 4. The CEI for RCM is 10593.22 which is 2.648 x 10^3 times better than CFD. The CEI can also be calculated based on the absolute deviation for energy storage also. The CEI along with the figures and the table provided above show that for a composite PCMHX, with a good estimation of thermal conductivity of composite, CFD is not needed as RCM can predict with excellent accuracy with significant speed gain. This also validates our assumption of neglecting the effects of natural convection in a metal foam composite PCM and shows that diffusion-based solvers can predict the thermal characteristics of a PCMHX with structured enhancement accurately.

Table 16: Comparison of Computational Cost and Accuracy Between CFD and RCM (With 4 Parallel Cores)

Parameter	Experimental	CFD	RCM
Run Time (s)	23,400	201,600	1.2
Time Step (s)	-	0.5	0.5
α	1	8.61	$5.13\text{x}10^{-5}$
Time for β=1	NA	22,067	22,008
Energy Storage (kJ)	68.31	67.72	67.7
Absolute Deviation for Energy Storage (%)	-	0.86	0.88
σ_{Temp} at A (K)	-	1.62	1.84
σ_{Temp} at C (K)	-	2.97	2.96

4.2 RCM for 3D Periodic Structured PCMHX

In this section, a computationally effective RCM is developed for the melting of PCM in different periodic structures subjected to constant heat flux as discussed in the Section 3.2. Image processing capability of a commercial software was used to find the local porosity values in the discretized grids. The model is validated against experimental data by Righetti et al. [104]. The accuracy in prediction of average temperature profile and energy storage is discussed with the respective computational costs.

4.2.1 Subject of Study

Figure 12 shows three different additively manufactured periodic structures which were experimentally tested under different heat flux conditions [104]. The intersection of aluminum fibers results three pyramid structures of 40 mm, 20 mm, and 10 mm cell size. The porosity (ratio of PCM volume and container volume) for all the geometries was 0.95. Each of the geometries were filled with an organic PCM with nominal melting temperature of 55°C, and melting tests were conducted under three different heat fluxes (6250 W/m^2, 12500 W/m^2 and 18750 W/m^2). Each sample used a 20 mm thick aluminum heater block and a 12 mm thick aluminum alloy square base with an area of 1764 mm^2 for homogeneous distribution of the heat flux.

Table 17: Thermophysical Properties of PCM and Metals

Properties	RT55	Aluminum alloy	Aluminum
k (W/m-K)	0.2	96	240
ρ (kg/m^3)	825	3745	2700
c_p (J/kg-K)	2000	1206	890
T_{sol} - T_{melt} (K)	324-330	-	-
ΔH (kJ/kg)	170	-	-

AlSi10Mg-0403 aluminum alloy was used for the additive manufacturing of the periodic structures and its conductivity was measured to be 96 Wm^{-1}K^{-1}[104]. The thermophysical properties of the PCM, aluminum, and aluminum alloy are listed in Table 17.

4.2.2 Model Details

Figure 36 shows the grid size and the time step independency of the RCM. In Figure 36a, RCM with 64 and 96 segments show very similar results. In Figure 36b, apart from 1s time step all the other time step selection in the RCM provided similar results. A time step size of 0.5s and grid size of 8x8 (64 segments) was selected for this work.

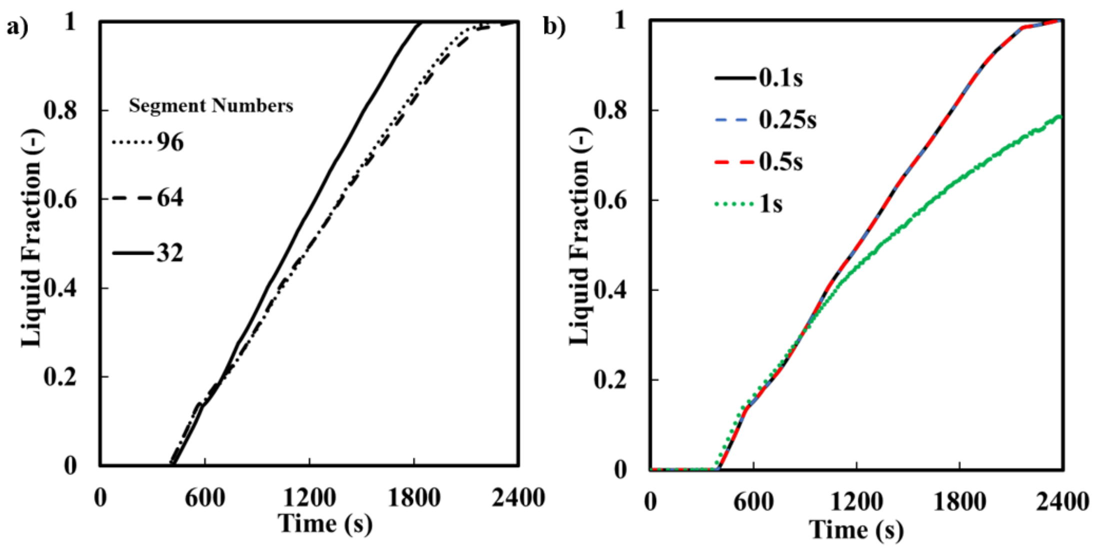

Figure 36: a) Effect of grid size, b) Effect of time step

The heat loss through the heater block was calculated using equation (40) [104].

$$\dot{Q} = 0.0162 * T_{H,avg}[°C] - 0.3459[W] \tag{40}$$

At all side walls the heat loss were assumed to have mixed convection-radiation boundary condition. Constant heat transfer coefficient of 10 $Wm^{-2} K^{-1}$ and an emissivity of 0.95 were imposed, as suggested by Calati et al. [108]. The free stream temperature was set equal to the ambient temperature of 293 K.

4.2.3 Model Validation

Six thermocouples were placed at different locations in the PCM domain for the experiments [104] .The experimental PCM average temperature is found by taking the average of these temperatures. Figure 37a, Figure 38a and Figure 39a compare the experimental average PCM temperature profile to the RCM predicted average temperature profile for the 10 mm, 20 mm and 40 mm geometries, respectively.

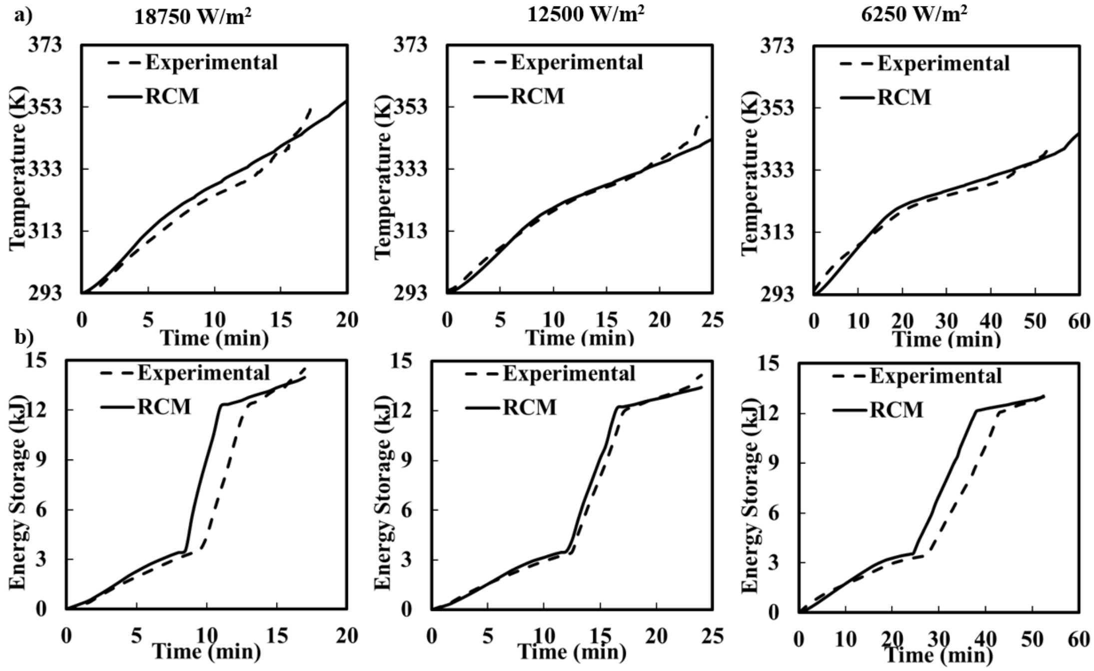

Figure 37: Comparison of experimental and RCM predicted a) Average PCM temperature b) Energy storage in 10 mm geometry

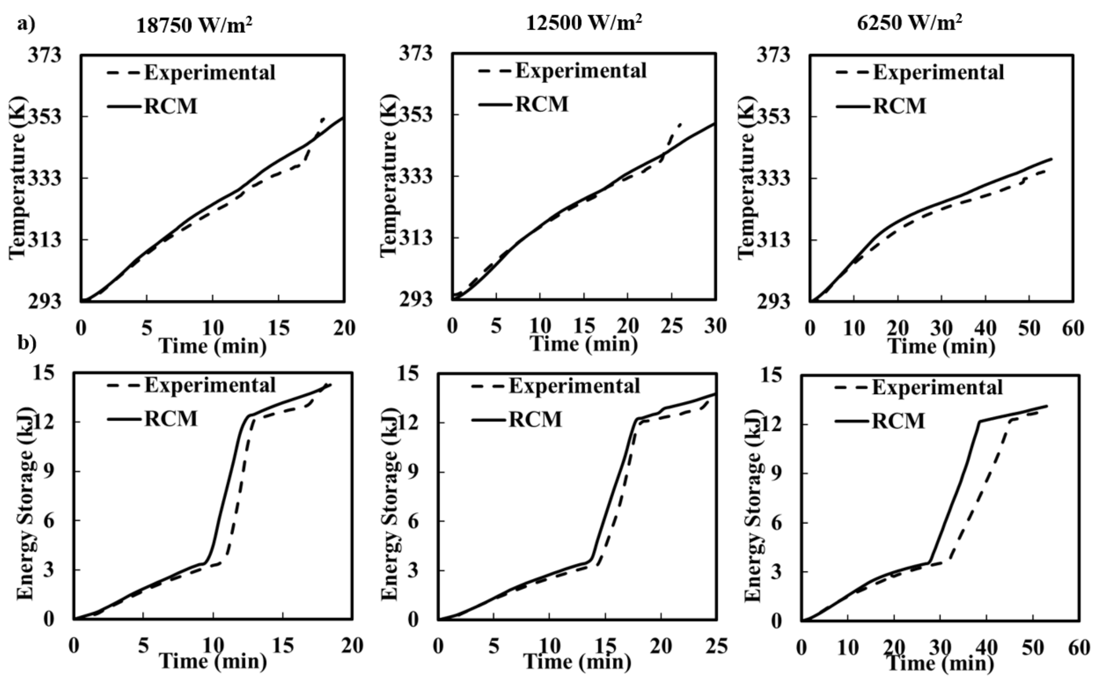

Figure 38: Comparison of experimental and RCM predicted a) Average PCM temperature b) Energy storage in 20 mm geometry

Each of the figures has three plots for three different heat flux (6250 W/m^2, 12500 W/m^2 and 18750 W/m^2) values used. The RCM predictions agree well with the experimental temperatures, in all the cases.

In RCM, the heat transfer is assumed to be conduction dominant, and the effect of natural convection is not considered. However, even though the model neglects the heat transfer enhancement by the natural convection, the results from Figure 37a, Figure 38a and Figure 39a show that the average PCM temperature is slightly overpredicted by the model in most of the cases. The PCM temperature can be measured separately from the metal in the experiment and this temperature is always lower compared to the surrounding metal structures. The model assumes a single temperature for the PCM and the metal alloy and thus overpredicts the PCM temperature. The assumption to neglect the contact resistance between PCM and metal structure can also play a part in the overprediction. The heat loss calculation with a constant heat transfer coefficient may also cause some deviation in the prediction; especially at the beginning of the tests. These reasons lead to the overprediction of PCM average temperature.

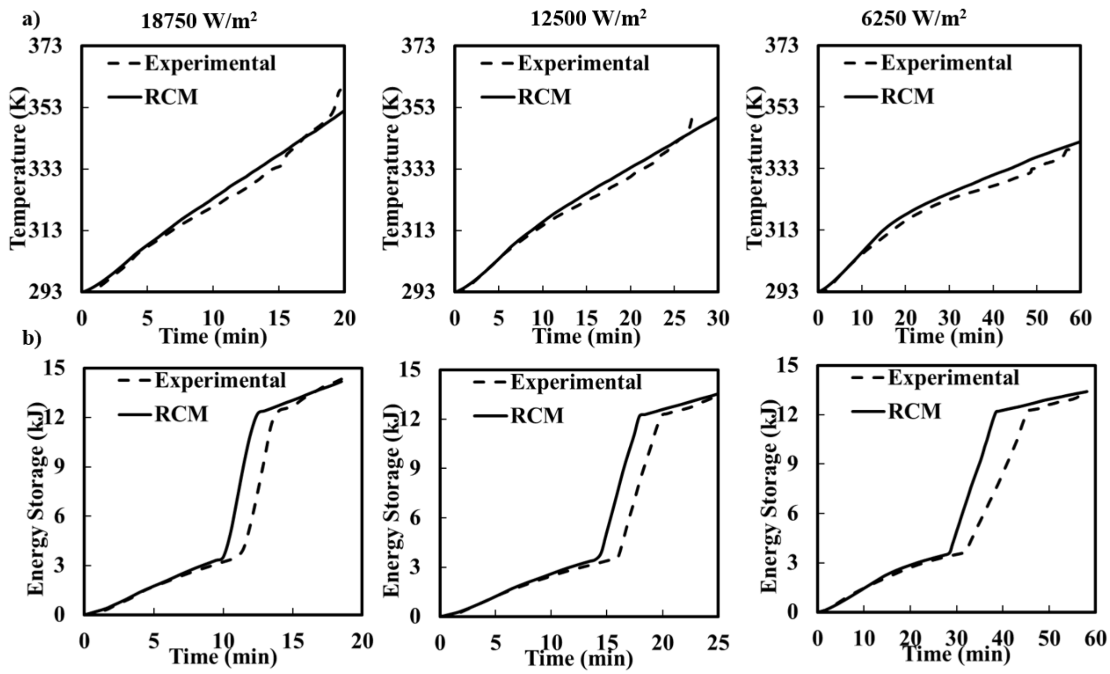

Figure 39: Comparison of experimental and RCM predicted a) Average PCM temperature b) Energy storage in 40 mm geometry

Figure 37b, Figure 38b and Figure 39b compares the experimental energy storage to the RCM predicted energy storage profile for the 10 mm, 20 mm, and 40 mm geometries, respectively. As the storage is a direct function of the average temperature, the deviation between the model and experimental temperature causes the deviation in storage as seen in the plots. But overall the energy storage curves show the same trend and the difference in energy storage in fully melting conditions is negligible.

Table 18 shows the computational cost and accuracy of average temperature prediction for RCM. The table shows the mean deviation of average temperature prediction for all the cases which ranges from 1.34K to 2.81K. The table also reports the maximum deviation in average temperature found in all the cases. The maximum average temperature deviation was found to be 5.45K for the 20mm geometry for a heat flux of 18750 W/m^2. It has been observed that the PCM temperature rises abruptly at the end of melting in some of the tests. The deviation between RCM and experiment due to this sudden rise in temperature is ignored for this comparison.

Table 18: Summary of Computational Cost and Temperature Prediction Accuracy

Case No	Base Diameter (mm)	Heat Flux (W/m^2)	Mean of Avg. Temperature Dev. (K)	Max. of Avg. Temperature Dev. (K)	Simulated Time (s)	Run Time (s)	α
1	10	18750	2.81	4.51	1250	0.326	2.61×10^{-4}
2		12500	1.34	3.30	1650	0.585	3.55×10^{-4}
3		6250	1.64	3.51	4200	1.305	3.11×10^{-4}
4	20	18750	2.15	5.45	1200	0.354	2.95×10^{-4}
5		12500	1.53	4.05	1800	0.602	3.34×10^{-4}
6		6250	2.45	3.87	3300	1.147	3.48×10^{-4}
7	40	18750	2.03	3.91	1500	0.444	2.96×10^{-4}
8		12500	1.56	3.15	1800	0.597	3.32×10^{-4}
9		6250	2.21	4.28	3600	1.150	3.19×10^{-4}

The most important aspect of the RCM is its speed and this is highlighted by the last column in the table. Here, the real-time factor (RTF) is the ratio between simulated time and simulation time required for the model. In all the cases, the RCM RTF was found to be in the order of 10^{-4}, whereas, in CFD the RTF is a value typically much greater than 1 as seen from the CFD simulations discussed in the previous sections. The results from Table 18 shows that RCM has very low computational cost with minimal penalty in accuracy.

4.3 RCM for Straight Tube Annular Finned PCMHX

In this section, an RCM is developed for an annular finned PCMHX with straight tube based on the details in section 2.2 and the model is validated with in-house experimental data and compared to a CFD model for accuracy and computational cost. The RCM developed in the previous sections only had constant heat flux boundary conditions. However, in the RCM developed for annular finned PCMHX with straight tube, the conjugate heat transfer is applied.

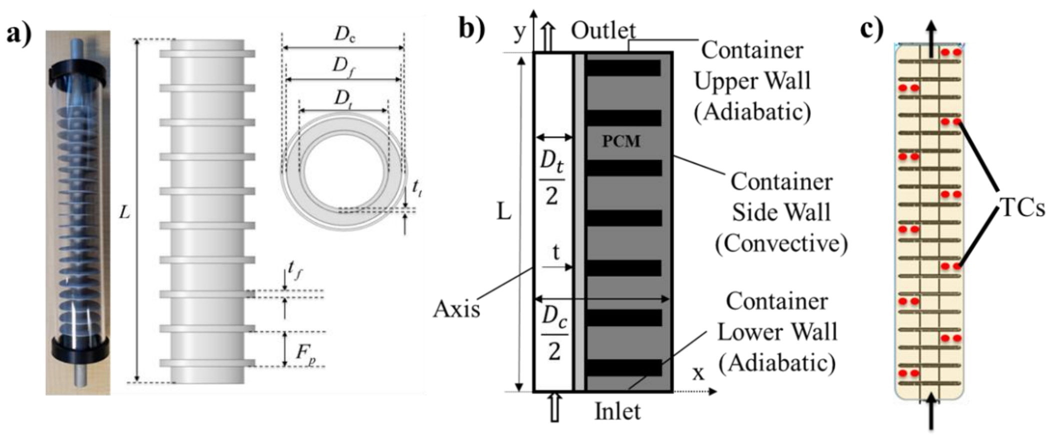

Figure 40: Schematic of a) Physical Model b) Computational Domain c) Thermocouple positions

4.3.1 Subject of Study

A straight tube annular finned PCMHX (Figure 40a) has been experimentally tested in-house under different operating conditions [60]. This geometry is modeled as an axisymmetric domain (Figure 40b) and the geometric specification of the configuration is listed in Table 19. Figure 40c shows the positions of 16 thermocouples (TCs) installed in the experimental setup which is used to calculate experimental average PCM temperature and to validate the model. The mass flow rate of water is 2.5 g/s and the water flow are in upwards direction.

Table 19: Geometry Specification of Annular Finned PCMHX

Dimension	Unit	Value
Tube Diameter - D_t	mm	12.7
Tube Wall Thickness - t	mm	1.5
Tube Length - L	mm	285
Tube and Fin Material	-	Aluminum alloy
Container Diameter - D_c	mm	44.5 [ID], 50.8[OD]
Fin Diameter- D_f	mm	42.45
Fin Pitch- F_P	mm	12.7
Fin Thickness	mm	1.5

The experiment utilized see-through insulation cylinders filled with air and argon gas to reduce the amount of heat loss from the test section while still being able to visually observe the experiment. Figure 41 shows the insulation cylinder assembly used in the experiment [60]. Several TCs were installed in the insulation cylinders and these were used to calculate heat loss from the PCMHX.

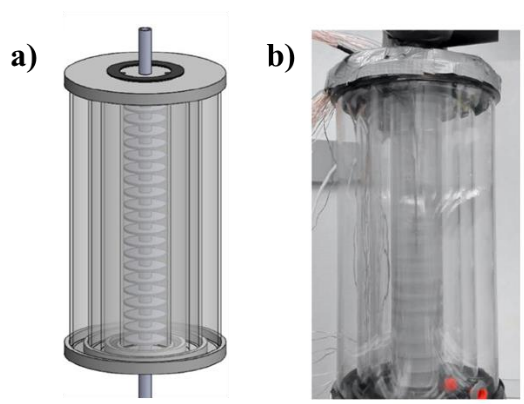

Figure 41: Insulation Cylinders Assembly a) 3D model b) Actual Experimental Setup

4.3.2 Details of Models and Settings

An axisymmetric CFD model is implemented for the experimental setup in ANSYS Fluent 2019 R3. The HTF is water, flowing from bottom to top, at different temperatures for melting and solidification processes. Paraffin RT35 [91] is used as the PCM and the tube and fins are made of aluminum allow. The material properties are listed in Table 20 . The corresponding Reynolds number for the tube flow is 327 and so a laminar flow model is considered on the tube side. The solidification and melting module in Fluent are used to simulate the phase-change process of PCM and the settings used is the same as described in section 4.1.

Table 20: Thermophysical Properties of Materials

Properties	**RT35**	**Aluminum alloy**
k (W/m-K)	0.2	170
ρ (kg/m^3)	880	2670
c_p (J/kg-K)	1800 (s),2400 (l)	890
T_{sol} - T_{melt} (K)	301.15-308.15	-
ΔH (kJ/kg)	135	-
μ (kg/m-s)	0.0029	-
β (K^{-1})	0.001	-

The initial temperature was selected from the individual experiment and the initial velocity of the computational domain is taken as zero. The upper and lower container walls are modeled as adiabatic and heat loss through container side wall is considered. The ambient temperature was taken as 25°C based on the experiment. Three different operating conditions were simulated and Table 21 lists the initial and boundary conditions used in the simulation.

Table 21: Boundary and Initial Conditions

Test No	Mass Flow Rate (g/s)	Flow Direction	Inlet Water Temp. (°C)	Initial Domain Temp. (°C)	Heat Loss HTC (W/m²·K)
1	2.5	Up	44.5	298.4	7.53
2			49.5	298.4	6.8
3			54.5	298.5	6.37

8000 structured rectangular grids were used to discretize the computational domain (Figure 42) and 0.1s time step size was used.

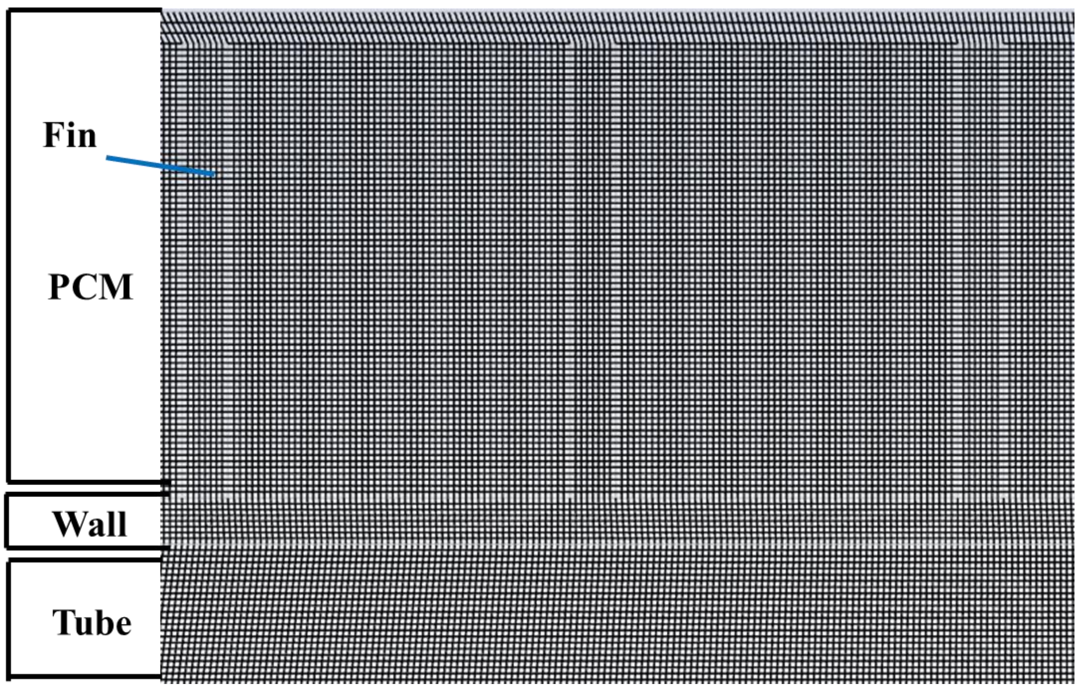

Figure 42: Structured rectangular grids in computational domain (zoomed in)

The RCM was developed using the approach detailed in section 2.2.

4.3.3 Model Validation

16 TCs were placed in different fin compartments in the PCMHX and an estimation was conducted to determine the TC temperature for the compartments where a fin is not located. The average of these temperature is denoted as the experimental

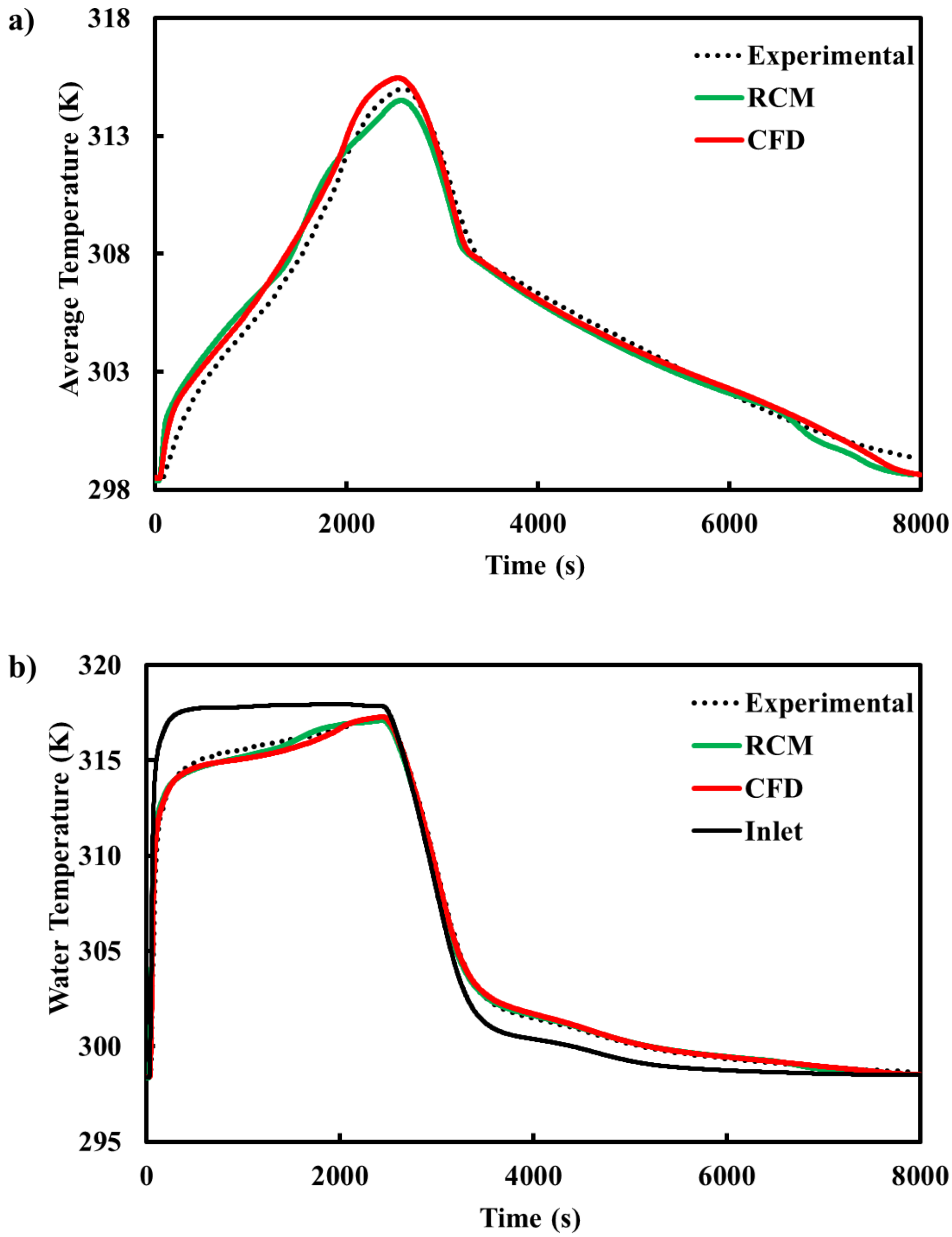

Figure 43: Comparison of a) Average PCM Temperature b) Outlet Water Temperature for Inlet Temperature of 44.5°C

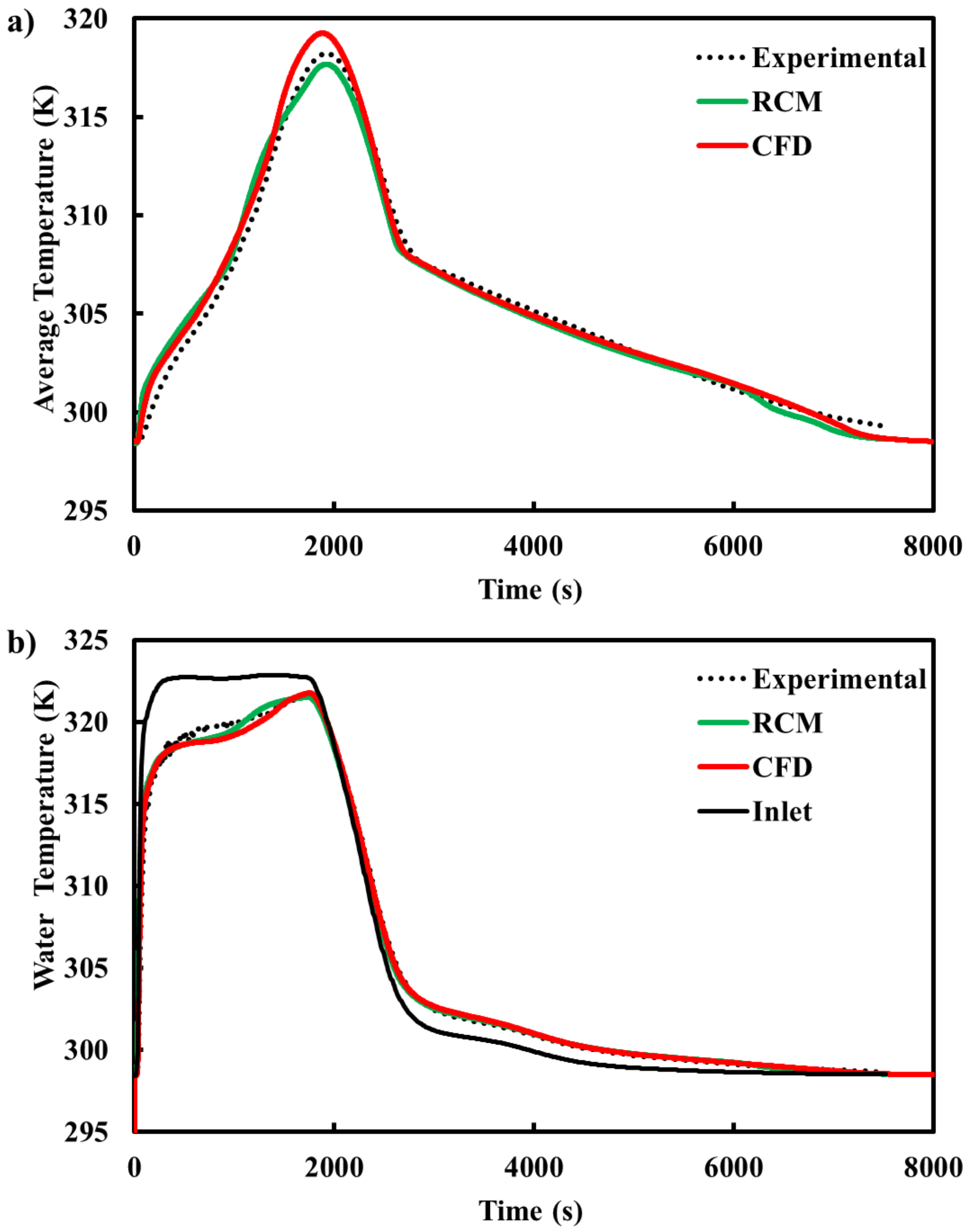

Figure 44: Comparison of a) Average PCM Temperature b) Outlet Water Temperature for Inlet Temperature of 49.5°C

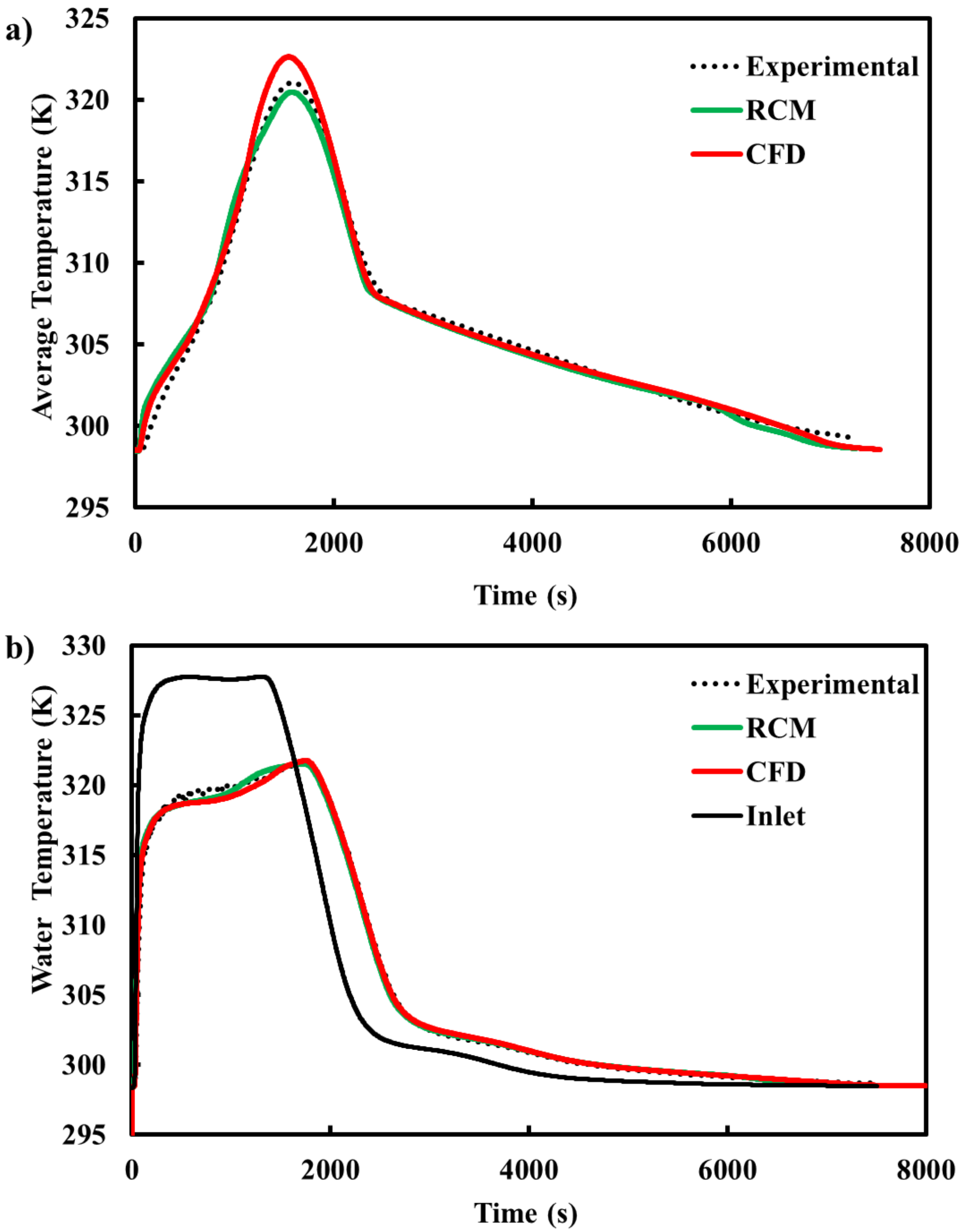

Figure 45: Comparison of a) Average PCM Temperature b) Outlet Water Temperature for Inlet Temperature of 54.5°C

average PCM temperature. The models can output the whole PCM domain temperature which is compared against the experimental temperature to validate the models. Figure 43a, Figure 44a and Figure 45a show the comparison of average PCM temperature from the models and the experiment for three different water inlet temperatures. Figure 43b, Figure 44b and Figure 45b compare the water outlet temperature from the models with the experimental water outlet temperature.

Figure 43, Figure 44 and Figure 45 show that both RCM and CFD can accurately predict the heat transfer in both the water side and the PCM side. Table 22 and Table 23 show the prediction accuracy of both the models for average PCM temperature and water outlet temperature respectively with Root Mean Square Error (RMSE) and maximum deviation. RMSE can be defined by equation (41).

$$RMSE = \sqrt{\frac{\sum_1^N (x_i - \hat{x})^2}{N}} \tag{41}$$

Table 22: Summary of Average PCM Temperature Prediction Accuracy

Inlet Water Temperature (°C)		CFD	RCM
44.5	RMSE (K)	0.55	0.7
	Maximum Deviation (K)	1.54	2.11
49.5	RMSE (K)	0.59	0.69
	Maximum Deviation (K)	1.47	2.1
54.5	RMSE (K)	0.62	0.66
	Maximum Deviation (K)	1.88	2.3

Table 23: Summary of Water Outlet Temperature Prediction Accuracy

Inlet Water Temperature (°C)		CFD	RCM
44.5	RMSE (K)	0.27	0.39
	Maximum Deviation (K)	2.23	4.34
49.5	RMSE (K)	0.35	0.48
	Maximum Deviation (K)	3.23	5.67
54.5	RMSE (K)	0.45	0.63
	Maximum Deviation (K)	4.23	7.26

From Table 22 and, Table 23 it is seen that CFD has smaller RMSE and maximum deviation compared to RCM, although the difference is not very high. The highest deviation in average PCM temperature prediction occurs at the end of the melting for both the models. The highest deviation for water outlet temperature prediction is seen at the beginning of the experiment when the inlet temperature increases rapidly which causes the deviations. The deviations are only seen for very small time and so they are not very clear in Figure 34b, Figure 35b and Figure 36b.

4.3.4 Computational Cost Comparison

Table 24 presents the hardware information of the computer and the computational cost of RCM and CFD for the case of inlet temperature of 44.5°C.

Table 24: Summary of computational cost of RCM and CFD

Model	Flow Time (s)	Simulation Time (s)	Speed Increase in RCM
RCM (400 segments)	8000	13	10^4
CFD (8000 elements)	8000	129600	

Table 22, Table 23 and Table 24 jointly show that while there is a small deviation in result prediction between the two models, RCM can predict the heat transfer and energy storage/ release in an annular finned PCMHX melting and solidification process with 4 orders of speed gain.

4.4 RCM for Annular Finned PCMHX with Copper Foam

4.4.1 Subject of Study

Copper foam has been added to the annular finned PCMHX discussed in the above section to further increase the PCM thermal conductivity. A straight tube annular finned PCMHX with copper foam (Figure 46a) has been experimentally tested in-house in different operating conditions. This geometry is modeled as an axisymmetric domain (Figure 46b). Figure 46c shows the 16 TCs located in different positions in the experimental setup to determine the average PCM temperature.

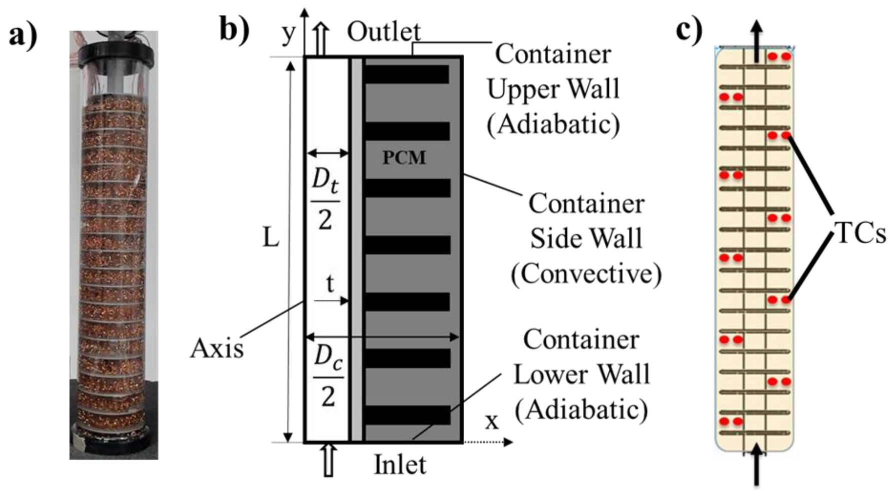

Figure 46: Schematic of a) Physical Model b) Computational Domain c) Thermocouple positions

The modeling approach of CFD and RCM for this configuration is the same as for the configuration without the copper foam. The only difference is seen in the calculation of the effective thermal conductivity k_{eff} which has been discussed in section 2.1.

4.4.2 Model Validation

Figure 47 shows that both RCM and CFD can accurately predict the heat transfer in both the water side and the PCM side. From Table 25, it is seen that the RMSE and maximum deviation in CFD is smaller in CFD compared to RCM as seem in the previous section. Similar to the annular finned PCMHX without copper foam, the highest deviation in average PCM temperature prediction is seen at the end of the melting for both the models and the highest deviation for water outlet temperature prediction is found at the beginning of the experiment.

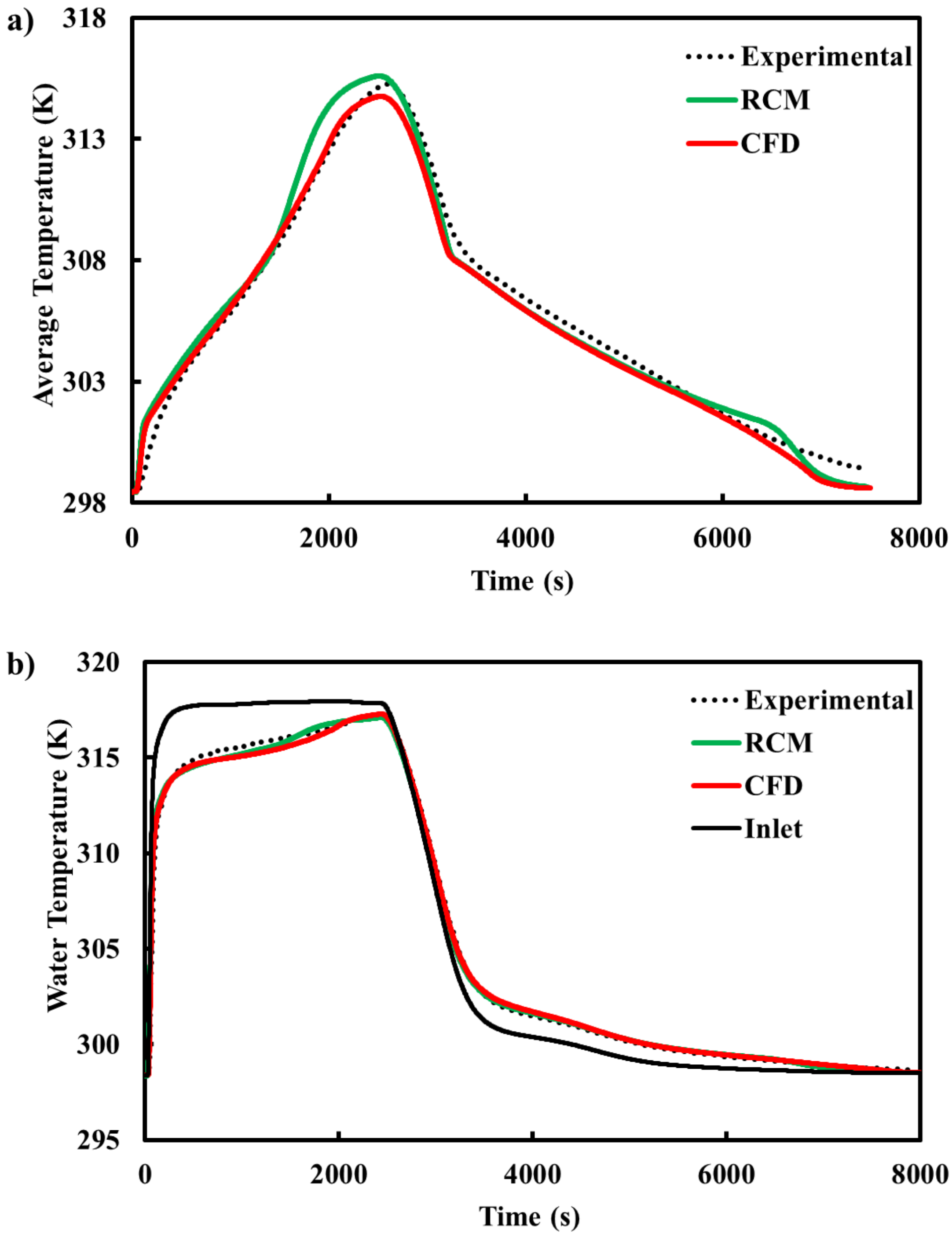

Figure 47: Comparison of a) Average PCM Temperature b) Outlet Water Temperature for Inlet Temperature of 44.5°C for annular fin PCMHX with Copper Sponge

Table 25: Summary of prediction accuracy for 44.5°C Inlet Water Temperature

Parameter		CFD	RCM
Average PCM Temperature	RMSE (K)	0.57	0.72
	Maximum Deviation (K)	1.61	2.03
Water Outlet Temperature	RMSE (K)	0.28	0.37
	Maximum Deviation (K)	2.61	4.43

4.4.3 Comparison of Computational Cost

Table 26 shows the hardware information of the computer and the computational cost of RCM and CFD for annular finned PCMHX with copper foam. Compared to the previous section, it is seen that the CFD simulation takes 3x more time. The addition of porous media approach in the CFD is the reason behind this additional computational cost. RCM uses the k_{eff} from the CFD and is $3x10^5$ times faster compared to CFD.

Table 26: Summary of computational cost of RCM and CFD

Model	**Flow Time (s)**	**Simulation Time (s)**	**Speed Increase in RCM**
RCM (400 segments)	8000	14	$3x10^4$
CFD (8000 elements)	8000	432000	

Chapter 5 RCM Application

5.1 Optimization of Annular Finned PCMHX Integrated with Domestic Water Heater

The load profile for domestic water heating is time-dependent and during some specific time of the day it generates high energy demands. Shifting the peak load completely or partly can have considerable positive environmental and economic impacts. PCM based thermal storage can be a useful technology in peak load shifting for the domestic water heater tank due to their high latent heat and high energy density compared to water. It has been seen that the temperature in the storage type water heater tank drops below set-point during daytime operation and power is drawn from the grid to heat up this water over the setpoint during peak electricity consumption hours [73].

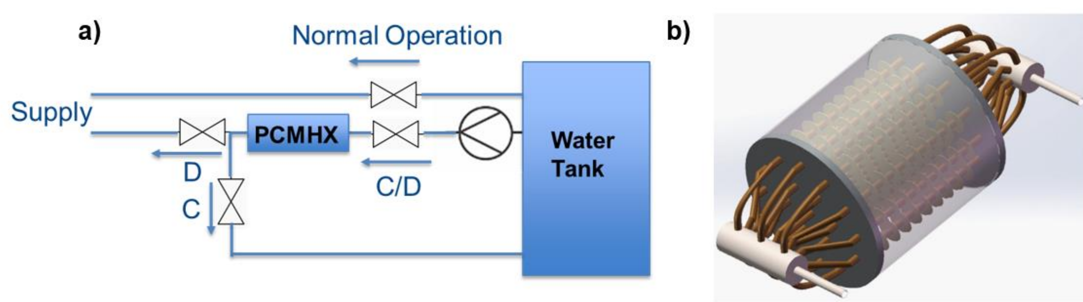

Figure 48: a) Operation diagram for PCMHX integrated with domestic water heater system b) Annular fin PCMHX storage diagram [26]

This temperature drop can be avoided by integrating a TES with domestic water heater system. One way to use TES is with PCMHX as shown in Figure 48a. The PCMHX will operate during the peak periods and will be used to heat up the water before it is supplied to the user. This is shown as the discharge (D) cycle in Figure 48.

During this time period the electric heater does not need to operate. The PCMHX will be charged during the off-peak hours.

Figure 48b shows the proposed latent thermal storage design where number of straight tube annular fins enhancement are used. The tubes will be connected in parallel and the flow rate will equally distributed. The PCM occupies the remaining space in the storage tank where there is no tubes and fins.

For heat extraction, the PCM inside the storage tank must have a melting temperature range high enough compared to the supply water temperature to create a temperature difference. However, selecting a PCM with a very high temperature can complicate the recharging cycle by requiring more energy and time. The water supply temperature must be equal to or greater than 51.7°C [109], thus an appropriate organic PCM RT62HC [110] is selected based on the operation temperature of the system and the melting temperature of the PCM. The thermophysical properties of the PCM, aluminum tube and fins are shown in Table 27.

Table 27: Thermophysical Properties of Materials

Properties	RT32HC	Aluminum alloy
k (W/m-K)	0.2	170
ρ (kg/m^3)	850	2670
c_p (J/kg-K)	2000	890
T_{sol} - T_{melt} (K)	333.15-337.15	-
ΔH (kJ/kg)	230	-

The flow rate of the water is selected to be 6.4L/min based on the DOE standard for a medium usage water heater [109]. We assume that 25% of the total daily hot water consumption will be supplied by the TES. Based on the total draw time for a medium usage tank and the 25% water consumption, the system integrated with TES needs to deliver water with 51.7°C with a flow rate of 6.4L/min for at least 540s continuously. The water inlet temperature in PCMHX is selected as 46.7°C with an assumption that the temperature drops 5°C during the daytime operation due to heat loss.

5.1.1 Optimization Problem Formulation

In previous sections, the validation of RCM for straight tube annular finned PCMHX and the speed increase compared to the CFD have been shown. The low computational cost of RCM can be effectively integrated with MOGA (Multi-objective Genetic Algorithm)[111]. The objective functions of this optimization are to minimize the water pressure drops through the tubes and minimize the total material mass (tube and fin mass) of PCMHX as shown in equation (42) .

$$\begin{gathered} min\ \Delta P_{water}\, , M_{HX,Material} \\ s.t. \\ t_{HW} \geq 540s; \qquad V_{HX,total} \leq 0.1 V_{tank,baseline}; \quad -0.1 \leq SOC \leq 0.1 \end{gathered} \tag{42}$$

The baseline water heater tank volume was selected from a commercially available electric water heater system in the market. It was assumed that there is no heat loss. The design space that is explored is listed in Table 28 . The tube diameter, fin thickness, container diameters are taken as discrete variables based on the off-the-shelf availability of aluminum tube, fin and polycarbonate tube. Two different thickness of tubes were selected as shown in Table 28.

Table 28: Optimization Design Space

Continuous Variables	Lower Limit	Upper Limit
Fin Pitch (mm), F_P	$0.2D_f$	$0.5D_f$
Length (mm), L	300	700
Discrete Variables	**Values**	
Tube Diameter (mm), D_t	15.87, 12.7, 9.52, 7.94 6.35,4.76 (t_t =0.89) 9.52, 6.35 (t_t =0.71)	
Fin Thickness (mm), t_f	0.81,0.63,0.41,0.25	
Container Diameter (mm), D_C	25.4, 28.58, 31.75, 34.93, 38.1, 44.45, 50.8, 57.15,63.5	
Number of Parallel Units, N	20-82	

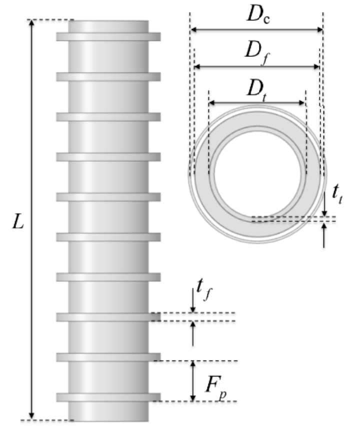

The constraints of the optimization are the total hot water supply time, the total HX volume and the State of Charge (SOC) as shown in equation(42). The minimum total hot water supply time is fixed based on the analysis done in the previous section. The maximum total HX volume ($V_{HX,total}$) is determined based on the volume of a commercially available storage type domestic water heater tank with medium water usage. The total volume of the selected domestic water heater tank ($V_{Tank, Baseline}$) is 254650 cm^3.

The Department of Energy's (DOE) target for thermal storage integrated systems is that the TES does not exceed 10% of the original system volume. The final constraint is based on State of Charge (SOC) which is defined as the ratio of energy stored in a TES at a specific time and the theoretical maximum storable energy in the TES and is shown in equation (43). The SOC constraints ensures that the TES remains mostly in the latent region during the discharge, minimizing temperature changes in the PCM. The problem formulation for the optimization is shown in equation (43).

$$SOC(t) = \frac{Remaining\ energy\ stored\ (t)}{Theoretical\ maximum\ storeable\ energy} \tag{43}$$

5.1.2 Optimization Results

Figure 49 shows the Pareto front for the optimization of annular finned PCMHX study. The shading of the design point is done based on the time, a design is capable of supplying hot water before the outlet temperature drops below the setpoint temperature

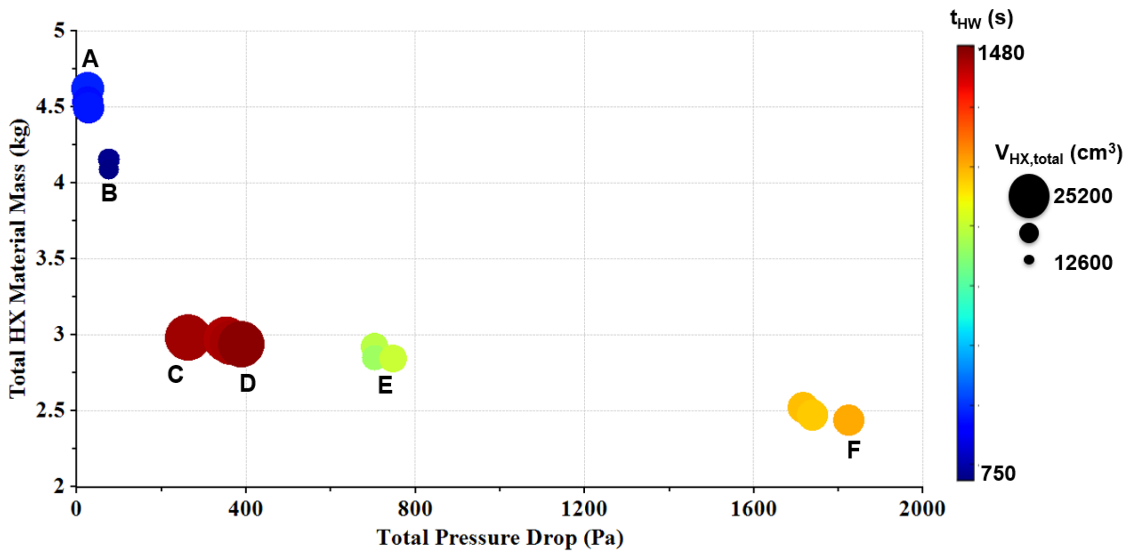

Figure 49: Pareto plot for annular finned PCMHX optimization

(shown by t_{HW} in Figure 49). The size of each design points in the Pareto front is done based on the total PCMHX volume which is by multiplying the volume of each container with the number of parallel units. Six designs from the Pareto front are analyzed next. Each of these points represents a cluster of designs that is seen in the Pareto front and the geometry and performance for the designs in the same cluster do not differ much. This similarity is not seen in only one cluster and so two designs (C and D from Figure 49) from that cluster have been picked. The geometry and performance parameters of these designs are shown in Table 29.

Table 29: Geometry and performance parameters of selected designs

Rea	**A**	**B**	**C**	**D**	**E**	**F**
No of HXs	82	80	70	48	72	76
Tube Diameter (mm)	15.875	12.7	9.525	9.525	7.9375	6.35
Tube Thickness (mm)	0.889	0.889	0.7112	0.7112	0.889	0.7112
Fin Diameter (mm)	24.575	21.4	27.75	27.75	24.575	24.575
Fin Thickness (mm)	0.254	0.254	0.254	0.254	0.254	0.254
Fin Pitch (mm)	6.76	5.32	8.67	9.33	7.22	7.23
Container Inner Diameter (mm)	28.575	25.4	31.75	31.75	28.575	28.575
Tube Length (mm)	400.1	430.2	450.2	662.9	425.1	425.5
Total Volume -PCMHX (cm^3)	21040	17439	24948	25191	19630	20739
Total Volume- PCM (cm^3)	14206	12701	22219	22462	17664	19219
PCM Volume Ratio (%)	67.5	72.8	89.1	89.2	90	92.7
t_{HW}(s)	862.5	751.4	1462.1	1478.1	1171.7	1272.3
Volume Ratio	1.083	1.068	1.098	1.099	1.077	1.082

The volume ratio is defined in equation (44) and Table 29 shows the volume ratio for each design. The values show that by adding the TES with water tank, the increase in the volume of the system is not exceeding 10% of the original system.

$$Volume\ Ratio = \frac{Water\ Tank\ Volume + TES\ Volume}{Water\ Tank\ Volume} \tag{44}$$

From Figure 49 and Table 29, as we move from left to right in the Pareto front, tube diameters and number of parallel units decrease. The Pareto front experiences a greater water pressure drop from left to right as a result. Larger tube diameters, lower fin pitches, and a higher number of parallel units are the reasons behind the higher mass of the designs on the left. With the exception of tube length and the number of parallel units, designs C and D are very similar. Compared to the other designs, Design D has a longer tube length, which compensates for its lower number of parallel units.

5.2 Ragone Plot Generation

Ragone plots are commonly used for electrochemical batteries to show the trade-off between energy storage and power [112]. Thermal energy storage devices (PCMHX) can be considered analogous to the electrochemical batteries (Table 30) and Ragone plots for these can demonstrate how geometry, material properties and operating conditions can play roles in the discharge energy and discharge power trade-off for a PCMHX [113].

Table 30: Definitions for different terms in electrochemical and thermal storage systems [113]

	Electrochemical storage	**Thermal Storage**
Maximum Capacity	$C_{e,max}$= nF (Ah)	$C_{th,max}$= $M_{PCM}\Delta h$ (Wh)
C-rate (h^{-1})	$\frac{I}{C_{e,max}}$	$\frac{\dot{q}}{C_{th,max}}$
SOC (%)	$\frac{\int Idt}{C_{e,max}}$	$\frac{\int \dot{q}dt}{C_{th,max}}$

PCMHX capacity can be defined as the total amount of heat that can be stored. Instead of a cut-off voltage, PCMHX has a cut-off temperature and the point where the fluid temperature reaches below the cut-off temperature defines the point where useful discharge energy ends. In the application of domestic water heater, the cut-off temperature is the supply temperature of hot water.

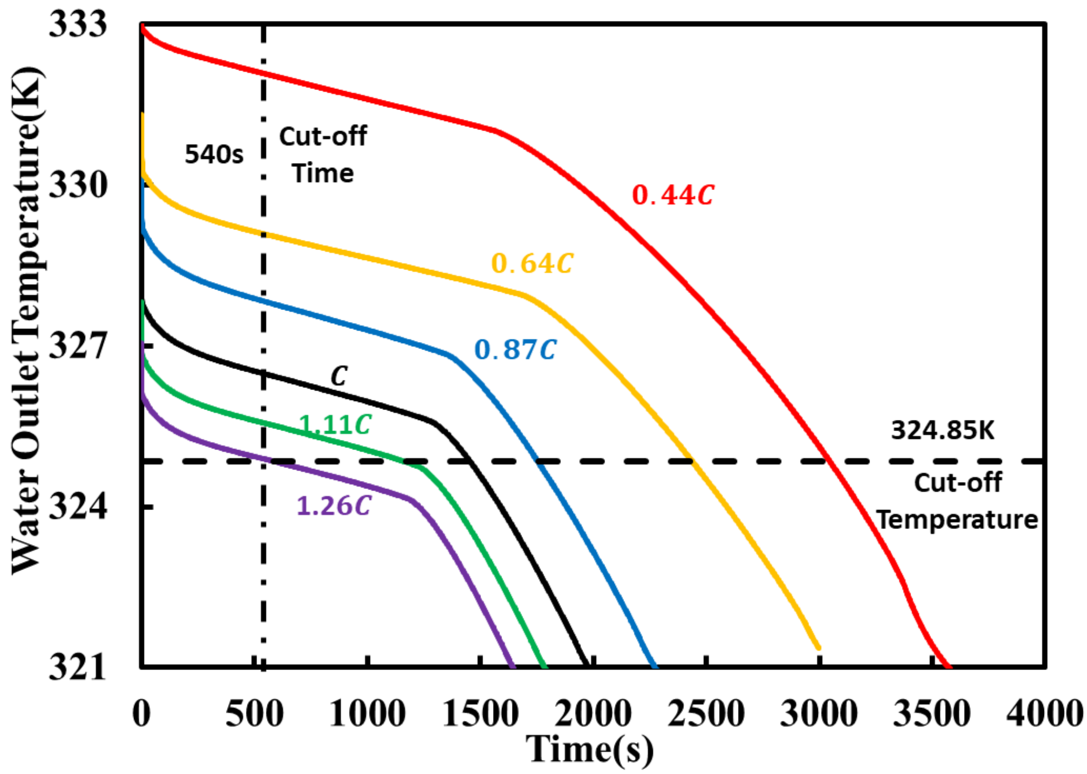

Figure 50: Thermal rate capability curves for PCMHX used with domestic water heater system

Figure 50 shows the water outlet temperature versus utilized time for an optimized PCMHX (design C). This design was selected from the Pareto front discussed in the previous section. The cutoff temperature (supply temperature-324.85K) is shown with the dotted black line. The C-rate of 1C is defined here for the design mass flow rate. The SOC and the C-rate are defined in Table 30. The plot shows that as the C-rate increases, the cut-off temperature is reached sooner while there is significant energy left in the thermal storage. Whereas, for lower C-rate of 0.44C and 0.7C, nearly all the energy stored in the system can be extracted before the fluid temperature reaches the cut-off line. This type of plot is known as thermal rate capability curves [113].

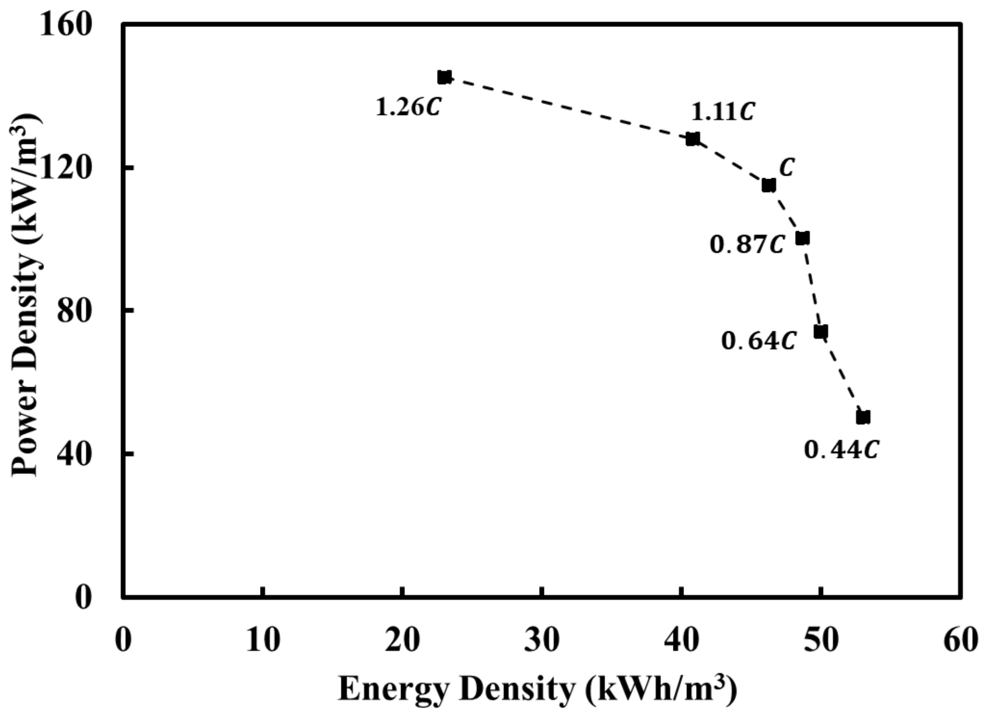

Figure 51: Ragone plot for PCMHX used with domestic water heater system

The rate-capability curves then can be used to generate the Ragone plot shown in Figure 51 for optimized design C. Each of the thermal rate-capability curve corresponds to specific point in the Ragone plot. The energy density is the cumulative energy discharged until the cut-off temperature is reached. The power density is defined as the average discharge rate until water outlet temperature reaches the cut-off temperature.

Figure 52 and Figure 53 show the impact of selecting different setpoint temperature in the thermal rate capability curves and Ragone plot, respectively. Figure 53 shows that by lowering the supply temperature by 1K, 10.5% higher energy density can be achieved. The plot also illustrates that the raising of supply temperature by 1K can also lead to 54.6% reduction in accessible energy. This plot shows the importance of cut-off temperature and the significant role it plays in the selection of an PCMHX for a specific application from a Pareto front.

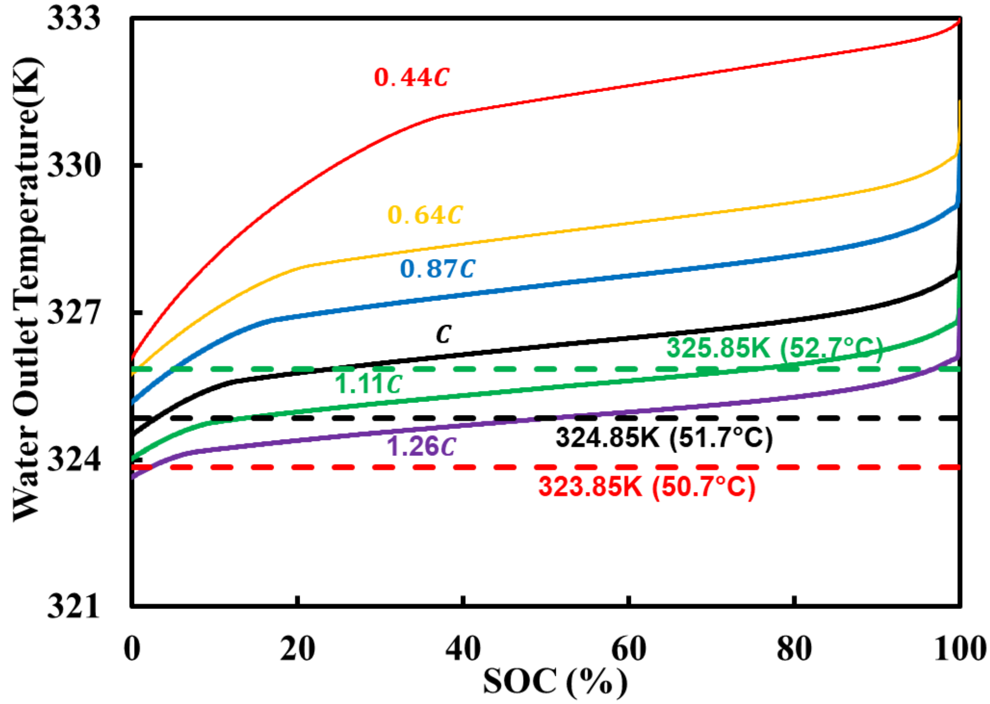

Figure 52: Impact of supply temperature selection in thermal rate capability curves

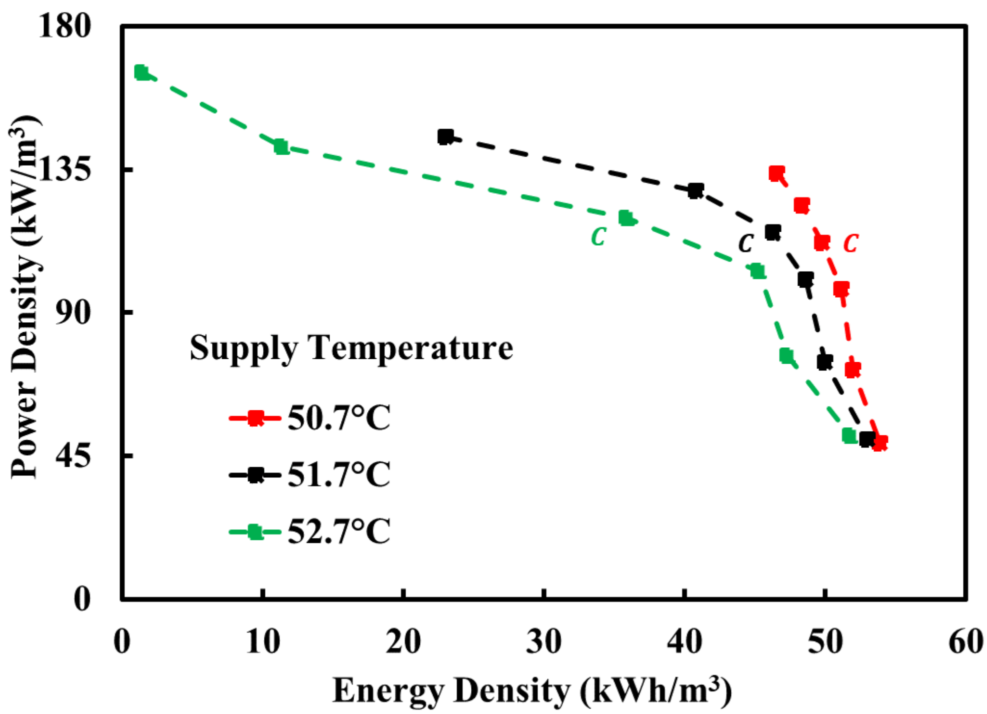

Figure 53: Impact of supply temperature selection in Ragone plot

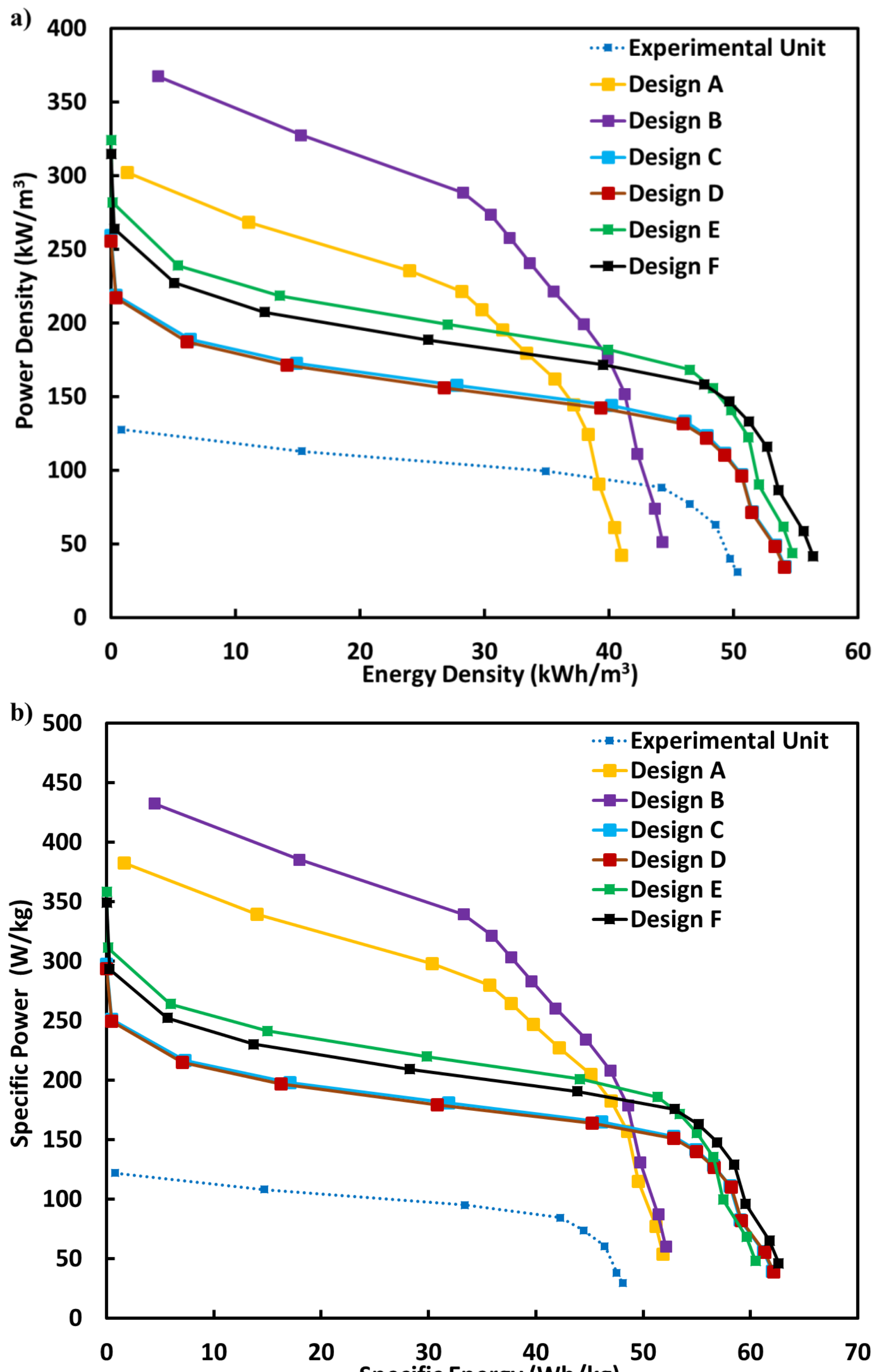

Figure 54: a) Volumetric, b) Gravimetric Ragone plots for different PCMHX designs

Figure 54 show the volumetric and gravimetric Ragone plots for the 6 designs that were discussed in the previous section. The Ragone plots for these designs show significant difference. Figure 54a show that design B has higher power density at high C-rates compared to the other five designs which is expected because this design has the smallest volume. Both designs B and A can provide higher power density and specific energy at higher C-rates but the total energy density and specific energy is lower for this units due to their small volume. Design C and D have almost the same geometric properties and we can see that these designs perform the same in different C-rates from both the volumetric and gravimetric plots.

The best design can be selected from Ragone plot by pushing the Ragone curve up (higher power) and to the right (higher energy). When compared with the annular finned PCMHX that was experimentally tested in-house, these designs show significantly higher performance for the same C-rate. However, for the selection of the best from the optimized designs, a tradeoff is necessary between energy and power based on user requirement. If the user requires a higher mass flow rate (which translates to higher C rate) then design B is the obvious choice as seen from both the gravimetric and volumetric plots in Figure 54. But if the user requirement is a lower C rate then designs E and F are better options as they have approximately 20% higher energy density and specific energy compared to design B. There is some tradeoff between E and F as well; as F has the highest specific energy but E has higher power density than F.

It is possible select a best design without considering tradeoff based on a specific C-rate and a specific performance metric. Table 31 shows the best designs for a specific metric based on the volume flow rate used in the optimization.

Table 31: Best Design for a Specific Metric for Volumetric Flow Rate of 6.4 L/min

Performance Metrics	Best Design
Specific Energy	F
Specific Power	B
Energy Density	F
Power Density	B

Design F can supply hot water for 69.4% longer time than Design B. However, design E can provide similar energy density in the operating condition but has half the pressure drop of design E. Considering these, design E can be selected as the best design for our specific operating condition.

5.3 Web Tool Development

The RCM is used to develop a publicly accessible rapid simulation tool for PCMHX by leveraging the low computational cost. The target is to allow the design community to perform transient simulation of selected PCMHX geometries. The web tool is hosted at a University of Maryland server. Currently the tool uses the validated annular finned PCMHX model. Figure 55 shows a screenshot of the webtool where the user can specify the annular finned PCMHX geometry. The tool is scalable and so a user can provide the number of thermal batteries to get results for a battery array. The tool is connected to a PCM database which has the properties of wide range of organic and inorganic PCMs. The user either select a PCM from the database or can use customized PCM thermophysical properties.

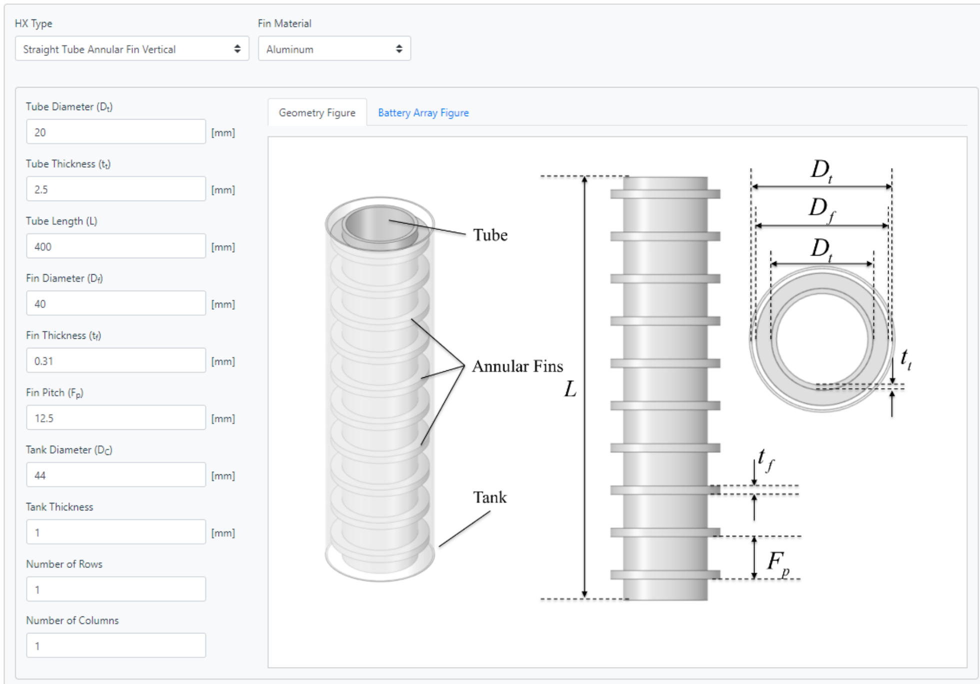

Figure 55: Annular fin geometry specification window in web tool

The annular finned PCMHX can be simulated with different tube wall boundary conditions. The available boundary conditions are the constant wall temperature, constant heat flux and the conjugate heat transfer. The available heat loss boundary conditions are adiabatic, constant heat flux and convective. The user can also choose between three available radial grid sizes.

Figure 56 shows the result window of the web tool and in this window the user can select a time step size and total run time before running the simulation. The user can visualize plots for different important parameters such as liquid fraction, PCM temperature, energy stored etc. The user can also download the case file to get the detailed simulation results from the model.

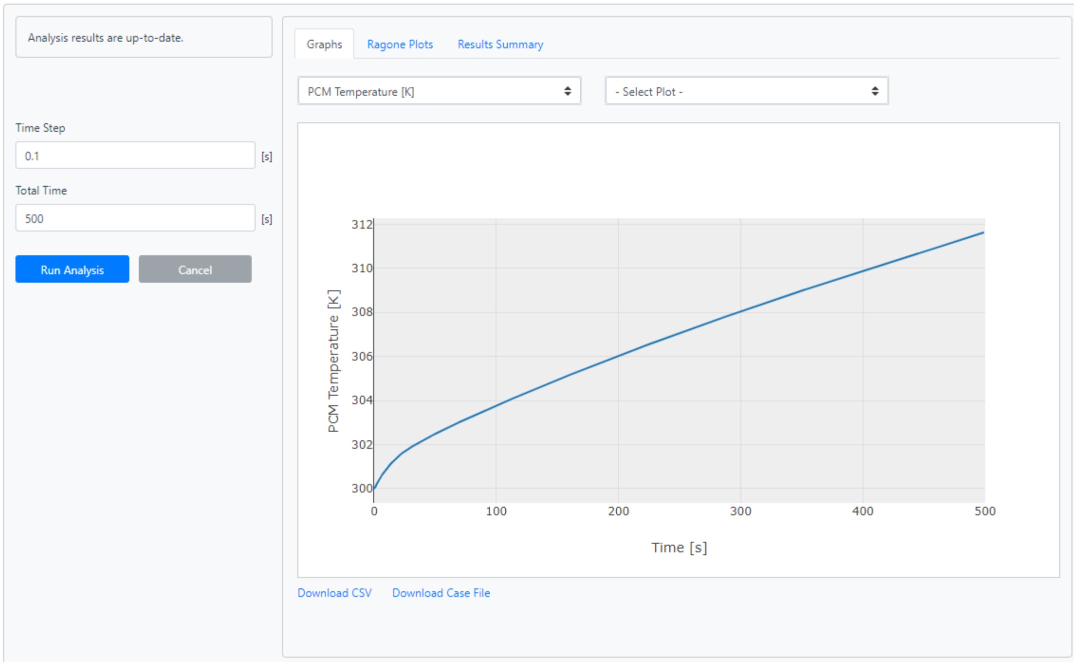

Figure 56: Results window in the web tool

Chapter 6 Conclusions, Contributions and Future Work

6.1 Conclusions

This thesis has presented the development and validation of resistance-capacitance models for four different PCMHXs. The geometries are a) Rectangular PCM enclosure enhanced with copper foam subject to constant heat flux, b) PCMHX geometry enhanced with 3D lattice structures subject to constant heat flux, c) cylindrical PCMHX with annular fin and tube in conjugate heat transfer with single-phase heat transfer fluid d) cylindrical PCMHX with annular fin and tube enhanced with copper foam, also in conjugate heat transfer. The thermal modeling parameters such as the resistance and capacitance for the models are specified based on the thermal properties of the PCMHX materials and the configuration of the container. All the models were validated with experimental data and apart from model b) the models were compared with CFD based models for accuracy and computational cost. RCM models showed similar prediction capability as CFD with negligible accuracy penalty but up to 5 orders of magnitude speed increase. Additionally, the computational efficiency of RCM has been leveraged to optimize a PCMHX integrated with a domestic water heater tank and to generate thermal Ragone plots. The main findings of this work are concluded below:

- Quantify the impact of uncertainty in thermophysical properties on performance prediction of PCMHX
    - In section 3.1, a CFD based model for annular finned PCMHX without additional enhancement was developed and validated with experimental data. It took approximately 105 hours and 50 hours to simulate 6000s

of flow time for melting and solidification respectively for this simple geometry. This study showed the prediction accuracy of CFD models but also highlighted the high computational cost associated with it and the necessity for a breakthrough in speed increase for PCMHX models.

  - Cylindrical PCMHXs without fins and with annular fins have been numerically studied in section 3.2 to find the effect of PCM thermophysical properties (thermal expansion coefficient, viscosity and melting range) on the prediction accuracy. The study underlines challenges imposed by the inaccurate knowledge of μ and β for accurate prediction of PCMHX temperature profile and melting time with CFD. For rapid simulation tool which can be reliably used for the evaluation of different PCMs, focus should be given on geometries where the momentum equations are not required to be solved. The values of μ and β are not required if assumption of neglecting gravitational effects is made. A fast solver is developed for geometries where this assumption can be considered valid.

- Develop a flexible, computationally efficient, and accurate model for common PCMHX
  - A resistance-capacitance model was developed for the melting of PCM with copper foam enhancement under constant heat flux in section 4.1. The model was validated against experimental data in the literature and compared with a CFD model. The mean deviations of CFD and experimental temperature are found to be 1.62K and 2.97K for two for

two thermocouples placed in the PCM domain. For RCM and experimental temperature, the mean deviations are found to be 1.84K and 2.96K for the same thermocouples. RCM was able to provide the local temperature and energy storage prediction accurately with 5 orders of speed gain compared to CFD. The study highlights that the diffusion-based solvers can predict the thermal characteristics of PCMHX and CFD based solvers are not necessary for this type of configuration.

- In section 4.2, an RCM was developed for the melting of PCM in periodic lattice structures with constant heat flux. The model takes the non-uniform distribution of the metal into account by estimating area-based porosity and converting it to volume-based porosity. The model was validated against experimental data and shows good prediction of both average PCM temperature and energy storage. The real-time factor of the model was found to be in the order of 10^{-4} and the accuracy penalty is negligible compared to the speed of the model.
- Next, an RCM was developed for the cylindrical PCMHX with annular fins in section 4.3. Compared to the previous models, this model is able to work with conjugate heat transfer and the model was validated with in-house test data in different operating conditions. A CFD model was also developed for the comparison of computational cost and accuracy with RCM. It was found that both the models can predict the average PCM and outlet water temperature accurately. The RMSE of the water outlet temperature was 0.45K for CFD and 0.63K for RCM. The RMSE

of the average PCM temperature was 0.62K for CFD and 0.7 for RCM. The results also highlighted that RCM was able to predict the thermal characteristics with 10^4 orders of speed increase compared to the CFD with negligible accuracy penalty.

  - An extension of this model was developed by adding the copper foam enhancement in the cylindrical PCMHX with annular fins in section 4.4. Similar to the original one, the model was validated with in house experimental results and compared with CFD. The results showed that the RCM can predict the average PCM and outlet water temperature accurately with $3x10^4$ times faster speed.

- Demonstrate application of RCM for design optimization of PCMHX and evaluate computational efficacy
  - The prediction accuracy and speed of RCM was leveraged for the design optimization of PCMHX integrated with a domestic water heater in section 5.1. Several annular finned PCMHX optimized designs were found using RCM with MOGA. The increase in the volume of the designs did not exceed 10% of the original system and all the designs supplied hot water for longer than the minimum required time. The optimized designs can supply water for 751s-1478s with a material mass increase of 2.44kg-4.62kg and an added water pressure drop of 26 Pa-1860Pa.
  - RCM can be used to generate thermal Ragone plots efficiently which uses the analogies between current flow in batteries and heat flow in

PCMHX to show trade-off between energy and power. The study in section 5.2 demonstrated the sensitivity of the Ragone plots with the change of setpoint temperature. A selection of the best design was made based on the total time of hot water supply and total pressure drop.

6.2 Contributions

Development and validation of low-cost high accuracy PCMHX model

The main contribution of this study is the development of low-cost highly accurate and validated models for different PCMHX geometries.

Computationally efficient optimization of PCMHX for peak load shaving

The second contribution of this work is the development of a computationally efficient optimization approach based on RCM which can work with any PCM. The approach was used to optimize designs for PCMHX integrated with domestic water heater which can shift peak loads.

Web-based tool development

Additionally, a publicly accessible rapid simulation tool for PCMHX was developed by leveraging the low computational cost of the RCM. The web-based tool can be used by the design community for performance simulation of selected PCMHX geometries.

Laid groundwork for generalized RCM solver

This work would serve as a groundwork for a generalized RCM solver which can be applied to solve any arbitrary resistance-capacitance network.

6.3 Future Work

This study can pave the way for future development of reduced order model for PCMHX. The following future work is recommended:

1) The current version of RCM uses a fixed time step and including sophisticated implicit solver algorithms with adaptive time step can be useful for more complex geometries and stiff problems
2) For integration with two-phase refrigerant, the model can be expanded to allow for conjugate heat transfer with two-phase heat transfer fluid.
3) Experimentally validate optimum designs found in this work
4) Explore topology optimization for non-conventional and novel heat transfer surfaces
5) Develop fast performance maps that can be integrated with building simulation tools such as EnergyPlus and Modelica.
6) Develop a generalized RCM solver that can be applied to any arbitrary RC network.

6.4 List of Publications

The following peer-reviewed conference papers were published from this research-

- T. Alam, D. Bacellar, J. Ling, and V. Aute, “Numerical Study and Validation of Melting and Solidification in PCM Embedded Heat Exchangers with Straight Tube,” in *18th International Refrigeration and Air Conditioning Conference at Purdue*, 2021.
- T. Alam, D. Bacellar, J. Ling, and V. Aute, “Effect of thermal expansion

coefficient, viscosity and melting range in simulation of pcm embedded heat exchangers with and without fins," in *International Mechanical Engineering Congress and Exposition*, 2021.

- T. Alam, D. Bacellar, J. Ling, and V. Aute, "Development and Validation of Resistance- Capacitance Model for Phase Change Material Embedded in Porous Media," *IEEE Intersoc. Conf. Therm. Thermomechanical Phenom. Electron. Syst.*, pp. 1–7, 2022, doi: 10.1109/iTherm54085.2022.9899532.
- T. Alam, G. Righetti, D. Bacellar, V. Aute, S. Mancin, and C. Park, "Development and Validation of Resistance-Capacitance Model (RCM) for Phase Change Material (PCM) Embedded in 3D Periodic Structures," in *19th International Refrigeration and Air Conditioning Conference at Purdue*, 2022.
- D. Bacellar, T. Alam, J. Ling, and V. Aute, "Automated Parameterized CFD Simulations of Phase-Change Material Embedded Heat Exchangers," *2021 20th IEEE Intersoc. Conf. Therm. Thermomechanical Phenom. Electron. Syst.*, pp. 538–543, 2021, doi: 10.1109/itherm51669.2021.9503249.
- D. Bacellar, T. Alam, J. Ling, and V. Aute, "A Study on Computational Cost Reduction of Simulations of Phase-Change Material (PCM) Embedded Heat Exchangers," *18th Int. Refrig. Air Cond. Conf. Purdue*, pp. 1–9, 2021.

Appendix

RCM for PCM Embedded in Porous Media

The thermal network parameters can be calculated with a simple explicit time-marching formulation described in equations (45)-(51)

$$\dot{Q}_{i,t} = \dot{Q}''\cdot A; i = 1 \tag{45}$$

$$\dot{Q}_{i,t} = \frac{T_{i-1,t} - T_{i,t}}{R_{i-1,t}}; i \geq 2 \tag{46}$$

$$\frac{dT_{i,t+1}}{dt} = \frac{\dot{Q}_{i,t} - \dot{Q}_{i+1,t}}{C_{i,t}} \tag{47}$$

$$T_{i,t+\Delta t} = T_{i,t} + \frac{dT_i}{dt}\cdot \Delta t \tag{48}$$

$$R_{i,t} \approx R_{cond} = \frac{L/N}{k_{eff}\cdot A}; R_{nat\_conv} \ll R_{cond} \tag{49}$$

$$C_{PCM} = \begin{cases} c_{p,\mathrm{s}} & \text{for } T \leq T_{sol} \\ c_{p,\mathrm{s}} + \dfrac{h_s}{T_{melt} - T_{sol}} & \text{for } T_{sol} < T < T_{melt} \\ c_{p,\mathrm{l}} & \text{for } T \geq T_{melt} \end{cases} \tag{50}$$

$$C_{i,t} = [\gamma C_{PCM}\rho_{PCM} + (1-\gamma)C_{FOAM}\rho_{FOAM}]V \tag{51}$$

Where, i denotes a specific segment and t denotes a specific time step. Total volume of a segment is denoted by V, area of a segment is A and total height of the domain is L. The domain is discretized into N number of equal length segments. $R_{i,t}$, $C_{i,t}$, $Q_{i,t}$, $T_{i,t}$ represents the thermal resistance, thermal capacitance, heat flow and temperature of a specific segment at a specific time. PCM porosity, γ, is 95%, β represents the liquid fraction, ρ, the density, and k_{eff} is the effective thermal conductivity. For the latter, the same value from CFD is used in RCM.

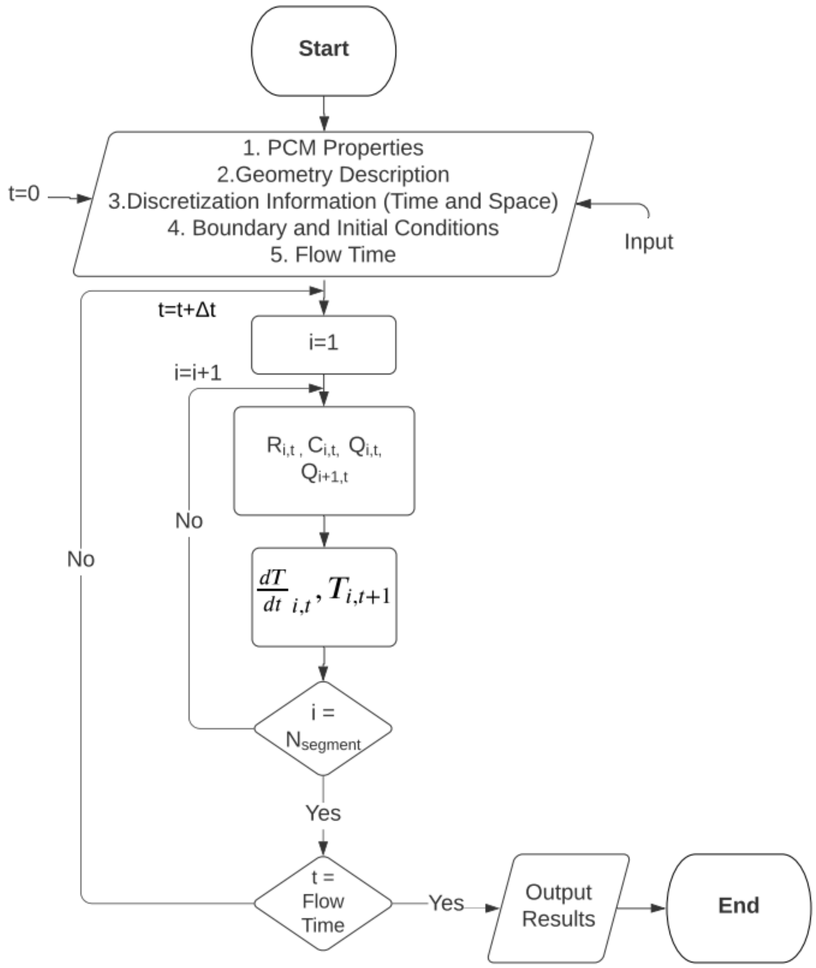

Figure 57: Solver Flowchart for the RCM PCM Embedded in Porous Media

RCM for PCM Embedded in 3D Periodic Structures

The thermal network parameters then can be calculated with explicit time-marching formulation described in equations (52)-(62)

$$\dot{Q}_{Heater} = \dot{Q}''\cdot A_{Base} \tag{52}$$

$$\dot{Q}_{Base,t} = \frac{T_{Heater,t} - T_{Base,t}}{R_{Heater}} \tag{53}$$

$$\dot{Q}_{i,j,t} = \frac{T_{Base,t} - T_{i,j,t}}{R_{Base}}; i = 1 \tag{54}$$

$$\dot{Q}_{i,j,0,t} = \frac{T_{i,j,t} - T_{i+1,j,t}}{R_{i,j,0}}; i \geq 2 \tag{55}$$

$$\dot{Q}_{i,j,1,t} = \frac{T_{i,j,t} - T_{i,j+1,t}}{R_{i,j,1}}; j \geq 2 \tag{56}$$

$$\frac{dT_{i,j,t}}{dt} = \frac{\dot{Q}_{i,j,0,t} + \dot{Q}_{i,j,1,t} - \dot{Q}_{i+1,j,0,t} - \dot{Q}_{i,j+1,1,t}}{C_{i,j}} \tag{57}$$

$$T_{i,j,t+\Delta t} = T_{i,j,t} + \frac{dT_{i,j,t}}{dt} \cdot \Delta t \tag{58}$$

$$R_{i,j,0} \approx R_{cond} = \frac{L/M}{k_{eff,i,j} \cdot A_{i,j}}; \tag{59}$$

$$R_{i,j,1} = \frac{W/N}{k_{eff,i,j} \cdot A_{i,j}}; R_{nat\_conv} \ll R_{cond} \tag{60}$$

$$k_{eff,i,j} = \gamma_{i,j} k_{PCM} + (1-\gamma_{i,j}) k_{alloy} \tag{61}$$

$$C_{i,t} = [\gamma_{i,j} C_{PCM} \rho_{PCM} + (1-\gamma_{i,j}) C_{alloy} \rho_{alloy}] V_{i,j} \tag{62}$$

Where, i denotes a specific segment lengthwise, j is widthwise and t denotes a specific time step. Total volume of a segment is denoted by *V*, area of a segment is *A*, total height of the domain is *L* and width is *W*. The domain is discretized into M x N segments. $R_{i,j,t}$, $C_{i,j,t}$, $Q_{i,j,t}$, $T_{i,j,t}$ represent the thermal resistance, thermal capacitance, heat flow and temperature of a specific segment at time *t*. PCM porosity is, γ, β represents the liquid fraction, ρ, the density, and k_{eff} is the effective thermal conductivity. Figure 58 shows the solver flow chart for the RCM.

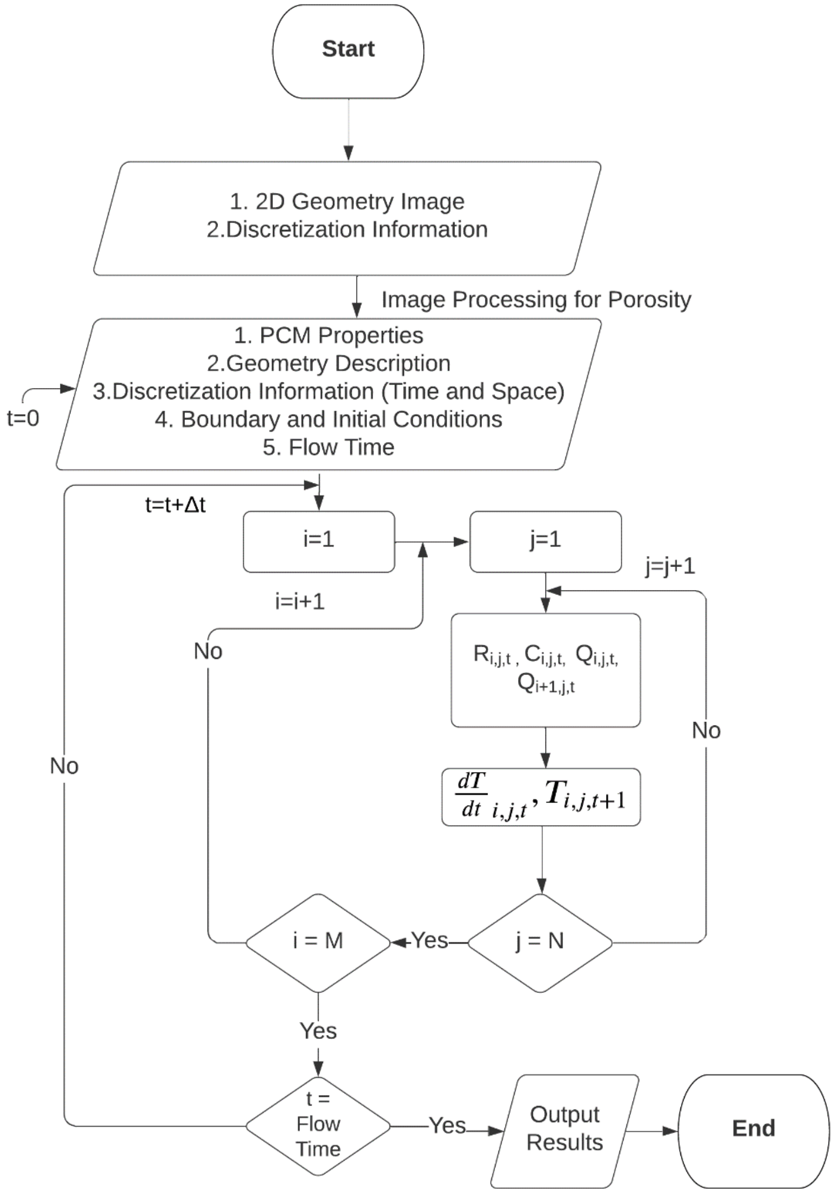

Figure 58: Solver flowchart for the RCM PCM Embedded in 3D Periodic Structures

Bibliography

[1] "EIA projects nearly 50% increase in world energy usage by 2050, led by growth in Asia," 2019. [Online]. Available: https://www.eia.gov/todayinenergy/detail.php?id=41433.

[2] M. González-Torres, L. Pérez-Lombard, J. F. Coronel, I. R. Maestre, and D. Yan, "A review on buildings energy information: Trends, end-uses, fuels and drivers," *Energy Reports*, vol. 8, pp. 626–637, 2022, doi: https://doi.org/10.1016/j.egyr.2021.11.280.

[3] Patrick E. Hopkins, "Bio-based phase change materials (PCMs) for thermal energy storage."

[4] I. Dincer and M. A. Ezan, *Heat Storage: A Unique Solution For Energy Systems*. 2018.

[5] I. Sarbu and C. Sebarchievici, "A comprehensive review of thermal energy storage," *Sustain.*, vol. 10, no. 1, 2018, doi: 10.3390/su10010191.

[6] G. Karmiris and T. Tengnér, "Peak Shaving Control Method for Energy Storage," *Electical Energy Storage Appl. Technol.*, pp. 1–6, 2013.

[7] A. Elgafy and K. Lafdi, "Effect of carbon nanofiber additives on thermal behavior of phase change materials," *Carbon N. Y.*, vol. 43, no. 15, pp. 3067–3074, 2005, doi: 10.1016/j.carbon.2005.06.042.

[8] P. Lamberg and K. Sirén, "Approximate analytical model for solidification in a finite PCM storage with internal fins," *Appl. Math. Model.*, vol. 27, no. 7, pp. 491–513, 2003, doi: 10.1016/S0307-904X(03)00080-5.

[9] B. Šarler, "Stefan's work on solid-liquid phase changes," *Eng. Anal. Bound. Elem.*, vol. 16, no. 2, pp. 83–92, 1995, doi: https://doi.org/10.1016/0955-7997(95)00047-X.

[10] P. J. Shamberger, "Cooling Capacity Figure of Merit for Phase Change Materials," *J. Heat Transfer*, vol. 138, no. 2, pp. 1–8, 2016, doi: 10.1115/1.4031252.

[11] H. Hu *et al.*, "Modelling and Simulation in Materials Science and Engineering Mathematical modelling of solidification and melting : a review Mathematical modelling of solidification and melting : a review," 1996.

[12] K. Yazawa, P. J. Shamberger, and T. S. Fisher, "Ragone Relations for Thermal Energy Storage Technologies," *Front. Mech. Eng.*, vol. 5, no. June, 2019, doi: 10.3389/fmech.2019.00029.

[13] R. Elarem *et al.*, "A comprehensive review of heat transfer intensification methods for latent heat storage units," *Energy Storage*, no. December, pp. 1–30, 2020, doi: 10.1002/est2.127.

[14] A. A. Al-Abidi, S. Mat, K. Sopian, M. Y. Sulaiman, and A. T. Mohammad, "Numerical study of PCM solidification in a triplex tube heat exchanger with internal and external fins," *Int. J. Heat Mass Transf.*, vol. 61, no. 1, pp. 684–695, 2013, doi: 10.1016/j.ijheatmasstransfer.2013.02.030.

[15] A. Ebrahimi, M. J. Hosseini, A. A. Ranjbar, M. Rahimi, and R. Bahrampoury, "Melting process investigation of phase change materials in a shell and tube heat exchanger enhanced with heat pipe," *Renew. Energy*, vol. 138, pp. 378–394,

2019, doi: 10.1016/j.renene.2019.01.110.

[16] M. Esapour, A. Hamzehnezhad, A. A. Rabienataj Darzi, and M. Jourabian, "Melting and solidification of PCM embedded in porous metal foam in horizontal multi-tube heat storage system," *Energy Convers. Manag.*, vol. 171, no. January, pp. 398–410, 2018, doi: 10.1016/j.enconman.2018.05.086.

[17] R. Karami and B. Kamkari, "Experimental investigation of the effect of perforated fins on thermal performance enhancement of vertical shell and tube latent heat energy storage systems," *Energy Convers. Manag.*, vol. 210, no. November 2019, p. 112679, 2020, doi: 10.1016/j.enconman.2020.112679.

[18] M. K. Koukou, M. G. Vrachopoulos, N. S. Tachos, G. Dogkas, K. Lymperis, and V. Stathopoulos, "Experimental and computational investigation of a latent heat energy storage system with a staggered heat exchanger for various phase change materials," *Therm. Sci. Eng. Prog.*, vol. 7, no. May, pp. 87–98, 2018, doi: 10.1016/j.tsep.2018.05.004.

[19] Z. Liu, Y. Yao, and H. Wu, "Numerical modeling for solid-liquid phase change phenomena in porous media: Shell-and-tube type latent heat thermal energy storage," *Appl. Energy*, vol. 112, pp. 1222–1232, 2013, doi: 10.1016/j.apenergy.2013.02.022.

[20] M. Longeon, A. Soupart, J. F. Fourmigué, A. Bruch, and P. Marty, "Experimental and numerical study of annular PCM storage in the presence of natural convection," *Appl. Energy*, vol. 112, pp. 175–184, 2013, doi: 10.1016/j.apenergy.2013.06.007.

[21] M. S. Mahdi *et al.*, "Numerical study and experimental validation of the effects of orientation and configuration on melting in a latent heat thermal storage unit," *J. Energy Storage*, vol. 23, no. November 2018, pp. 456–468, 2019, doi: 10.1016/j.est.2019.04.013.

[22] S. Mat, A. A. Al-Abidi, K. Sopian, M. Y. Sulaiman, and A. T. Mohammad, "Enhance heat transfer for PCM melting in triplex tube with internal-external fins," *Energy Convers. Manag.*, vol. 74, pp. 223–236, 2013, doi: 10.1016/j.enconman.2013.05.003.

[23] L. Pu, S. Zhang, L. Xu, and Y. Li, "Thermal performance optimization and evaluation of a radial finned shell-and-tube latent heat thermal energy storage unit," *Appl. Therm. Eng.*, vol. 166, no. November 2019, p. 114753, 2020, doi: 10.1016/j.applthermaleng.2019.114753.

[24] N. H. S. Tay, F. Bruno, and M. Belusko, "Comparison of pinned and finned tubes in a phase change thermal energy storage system using CFD," *Appl. Energy*, vol. 104, pp. 79–86, 2013, doi: 10.1016/j.apenergy.2012.10.040.

[25] X. Yang, J. Guo, B. Yang, H. Cheng, P. Wei, and Y. L. He, "Design of non-uniformly distributed annular fins for a shell-and-tube thermal energy storage unit," *Appl. Energy*, vol. 279, no. July, p. 115772, 2020, doi: 10.1016/j.apenergy.2020.115772.

[26] X. Yang, Z. Lu, Q. Bai, Q. Zhang, L. Jin, and J. Yan, "Thermal performance of a shell-and-tube latent heat thermal energy storage unit: Role of annular fins," *Appl. Energy*, vol. 202, pp. 558–570, 2017, doi: 10.1016/j.apenergy.2017.05.007.

[27] W. Youssef, Y. T. Ge, and S. A. Tassou, "CFD modelling development and

experimental validation of a phase change material (PCM) heat exchanger with spiral-wired tubes," *Energy Convers. Manag.*, vol. 157, no. December 2017, pp. 498–510, 2018, doi: 10.1016/j.enconman.2017.12.036.

[28] P. Zhang, Z. N. Meng, H. Zhu, Y. L. Wang, and S. P. Peng, "Melting heat transfer characteristics of a composite phase change material fabricated by paraffin and metal foam," *Appl. Energy*, vol. 185, pp. 1971–1983, 2017, doi: 10.1016/j.apenergy.2015.10.075.

[29] S. Zhang, L. Pu, L. Xu, R. Liu, and Y. Li, "Melting performance analysis of phase change materials in different finned thermal energy storage," *Appl. Therm. Eng.*, vol. 176, no. April, p. 115425, 2020, doi: 10.1016/j.applthermaleng.2020.115425.

[30] F. Zhu, C. Zhang, and X. Gong, "Numerical analysis and comparison of the thermal performance enhancement methods for metal foam/phase change material composite," *Appl. Therm. Eng.*, vol. 109, pp. 373–383, 2016, doi: 10.1016/j.applthermaleng.2016.08.088.

[31] D. Bacellar, T. Alam, J. Ling, and V. Aute, "A Study on Computational Cost Reduction of Simulations of Phase-Change Material (PCM) Embedded Heat Exchangers," in *18th International Refrigeration and Air Conditioning Conference at Purdue*, 2021, pp. 1–9.

[32] D. Bacellar, T. Alam, J. Ling, and V. Aute, "Automated Parameterized CFD Simulations of Phase-Change Material Embedded Heat Exchangers," *2021 20th IEEE Intersoc. Conf. Therm. Thermomechanical Phenom. Electron. Syst.*, pp. 538–543, 2021, doi: 10.1109/itherm51669.2021.9503249.

[33] M. S. Mahdi, H. B. Mahood, J. M. Mahdi, A. A. Khadom, and A. N. Campbell, "Improved PCM melting in a thermal energy storage system of double-pipe helical-coil tube," *Energy Convers. Manag.*, vol. 203, no. September 2019, p. 112238, 2020, doi: 10.1016/j.enconman.2019.112238.

[34] A. F. Di Rienzo, "Mesoscopic Numerical Methods for Reactive Flows: Lattice Boltzmann Method and Beyond," 2012.

[35] K.-R. K. Wichmann, "Performance Aspects of Incompressible Navier-Stokes Solvers: Lattice-Boltzmann Method vs. Finite Difference Method," 2019.

[36] Q. Li, K. H. Luo, Q. J. Kang, Y. L. He, Q. Chen, and Q. Liu, "Lattice Boltzmann methods for multiphase flow and phase-change heat transfer," *Prog. Energy Combust. Sci.*, vol. 52, no. 0, pp. 62–105, 2016, doi: 10.1016/j.pecs.2015.10.001.

[37] Q. Liu and Y. L. He, "Double multiple-relaxation-time lattice Boltzmann model for solid-liquid phase change with natural convection in porous media," *Phys. A Stat. Mech. its Appl.*, vol. 438, pp. 94–106, 2015, doi: 10.1016/j.physa.2015.06.018.

[38] D. Gao, Z. Chen, D. Zhang, and L. Chen, "Lattice Boltzmann modeling of melting of phase change materials in porous media with conducting fins," *Appl. Therm. Eng.*, vol. 118, pp. 315–327, 2017, doi: 10.1016/j.applthermaleng.2017.03.002.

[39] D. Li, Q. Ren, Z. X. Tong, and Y. L. He, "Lattice Boltzmann models for axisymmetric solid–liquid phase change," *Int. J. Heat Mass Transf.*, vol. 112, pp. 795–804, 2017, doi: 10.1016/j.ijheatmasstransfer.2017.03.127.

[40] E. M. Sparrow, J. W. Ramsey, and R. G. Kemink, "Freezing Controlled by

Natural Convection," *J. Heat Transfer*, vol. 101, no. 4, pp. 578–584, Nov. 1979, doi: 10.1115/1.3451040.
[41] D. Chen, A. Riaz, V. C. Aute, and R. Radermacher, "A solid–liquid model based on lattice Boltzmann method for phase change material melting with porous media in cylindrical heat exchangers," *Appl. Therm. Eng.*, vol. 207, no. January, p. 118080, 2022, doi: 10.1016/j.applthermaleng.2022.118080.
[42] M. Martinelli, F. Bentivoglio, A. Caron-Soupart, R. Couturier, J. F. Fourmigue, and P. Marty, "Experimental study of a phase change thermal energy storage with copper foam," *Appl. Therm. Eng.*, vol. 101, pp. 247–261, 2016, doi: 10.1016/j.applthermaleng.2016.02.095.
[43] E. H. Mathews, P. G. Richards, and C. Lombard, "A first-order thermal model for building design," *Energy Build.*, vol. 21, no. 2, pp. 133–145, 1994, doi: 10.1016/0378-7788(94)90006-X.
[44] A. Zarrella, A. Capozza, and M. De Carli, "Analysis of short helical and double U-tube borehole heat exchangers: A simulation-based comparison," *Appl. Energy*, vol. 112, pp. 358–370, 2013, doi: 10.1016/j.apenergy.2013.06.032.
[45] N. Zhu, S. Wang, X. Xu, and Z. Ma, "A simplified dynamic model of building structures integrated with shaped-stabilized phase change materials," *Int. J. Therm. Sci.*, vol. 49, no. 9, pp. 1722–1731, 2010, doi: 10.1016/j.ijthermalsci.2010.03.020.
[46] A. Bontemps, M. Ahmad, K. Johanns, and H. Sallée, "Experimental and modelling study of twin cells with latent heat storage walls," *Energy Build.*, vol. 43, no. 9, pp. 2456–2461, 2011, doi: 10.1016/j.enbuild.2011.05.030.
[47] J. Gao, T. Yan, T. Xu, Z. Ling, G. Wei, and X. Xu, "Development and experiment validation of variable-resistance-variable-capacitance dynamic simplified thermal models for shape-stabilized phase change material slab," *Appl. Therm. Eng.*, vol. 146, no. July 2018, pp. 364–375, 2019, doi: 10.1016/j.applthermaleng.2018.09.124.
[48] A. Stupar, U. Drofenik, and J. W. Kolar, "Application of phase change materials for low duty cycle high peak load power supplies," *2010 6th Int. Conf. Integr. Power Electron. Syst. CIPS 2010*, pp. 16–18, 2011.
[49] P. A. Mirzaei and F. Haghighat, "Modeling of phase change materials for applications in whole building simulation," *Renew. Sustain. Energy Rev.*, vol. 16, no. 7, pp. 5355–5362, 2012, doi: 10.1016/j.rser.2012.04.053.
[50] C. Pan, S. Hoenig, C. H. Chen, S. Neti, C. Romero, and N. Vermaak, "Efficient modeling of phase change material solidification with multidimensional fins," *Int. J. Heat Mass Transf.*, vol. 115, pp. 897–909, 2017, doi: 10.1016/j.ijheatmasstransfer.2017.07.120.
[51] M. Parsazadeh, Z. Liu, and X. Duan, "An improved layered thermal resistance model for solid-liquid phase change time estimation," *Int. J. Therm. Sci.*, vol. 156, no. June, p. 106496, 2020, doi: 10.1016/j.ijthermalsci.2020.106496.
[52] H. Neumann, S. Gamisch, and S. Gschwander, "Comparison of RC-model and FEM-model for a PCM-plate storage including free convection," *Appl. Therm. Eng.*, vol. 196, no. September 2020, p. 117232, 2021, doi: 10.1016/j.applthermaleng.2021.117232.
[53] J. Vogel, J. Felbinger, and M. Johnson, "Natural convection in high temperature

flat plate latent heat thermal energy storage systems,” *Appl. Energy*, vol. 184, pp. 184–196, 2016, doi: 10.1016/j.apenergy.2016.10.001.
[54] E. Fleming, S. Wen, L. Shi, and A. K. Da Silva, “Experimental and theoretical analysis of an aluminum foam enhanced phase change thermal storage unit,” *Int. J. Heat Mass Transf.*, vol. 82, pp. 273–281, 2015, doi: 10.1016/j.ijheatmasstransfer.2014.11.022.
[55] H. Zheng, C. Wang, Q. Liu, Z. Tian, and X. Fan, “Thermal performance of copper foam/paraffin composite phase change material,” *Energy Convers. Manag.*, vol. 157, no. September 2017, pp. 372–381, 2018, doi: 10.1016/j.enconman.2017.12.023.
[56] H. T. Cui, “Experimental investigation on the heat charging process by paraffin filled with high porosity copper foam,” *Appl. Therm. Eng.*, vol. 39, pp. 26–28, 2012, doi: 10.1016/j.applthermaleng.2012.01.037.
[57] M. Moeini Sedeh and J. M. Khodadadi, “Thermal conductivity improvement of phase change materials/graphite foam composites,” *Carbon N. Y.*, vol. 60, pp. 117–128, 2013, doi: 10.1016/j.carbon.2013.04.004.
[58] G. Righetti, L. Doretti, C. Zilio, G. A. Longo, and S. Mancin, “Experimental investigation of phase change of medium/high temperature paraffin wax embedded in 3D periodic structure,” *Int. J. Thermofluids*, vol. 5–6, p. 100035, 2020, doi: 10.1016/j.ijft.2020.100035.
[59] C. Zhao *et al.*, “Simulations of melting performance enhancement for a PCM embedded in metal periodic structures,” *Int. J. Heat Mass Transf.*, vol. 168, 2021, doi: 10.1016/j.ijheatmasstransfer.2020.120853.
[60] J. Yang, J. Muehlbauer, D. Bacellar, V. Aute, and Y. Hwang, “Experimental Investigation of a Phase Change Material Charged Finned-Tube Heat Exchanger,” in *19th International Refrigeration and Air Conditioning Conference at Purdue*, 2022.
[61] F. Agyenim, P. Eames, and M. Smyth, “A comparison of heat transfer enhancement in a medium temperature thermal energy storage heat exchanger using fins,” *Sol. Energy*, vol. 83, no. 9, pp. 1509–1520, 2009, doi: 10.1016/j.solener.2009.04.007.
[62] N. H. S. Tay, F. Bruno, and M. Belusko, “Experimental validation of a CFD and an ε-NTU model for a large tube-in-tank PCM system,” *Int. J. Heat Mass Transf.*, vol. 55, no. 21–22, pp. 5931–5940, 2012, doi: 10.1016/j.ijheatmasstransfer.2012.06.004.
[63] V. Saydam, M. Parsazadeh, M. Radeef, and X. Duan, “Design and experimental analysis of a helical coil phase change heat exchanger for thermal energy storage,” *J. Energy Storage*, vol. 21, no. February 2018, pp. 9–17, 2019, doi: 10.1016/j.est.2018.11.006.
[64] L. Jian-you, “Numerical and experimental investigation for heat transfer in triplex concentric tube with phase change material for thermal energy storage,” *Sol. Energy*, vol. 82, no. 11, pp. 977–985, 2008, doi: 10.1016/j.solener.2008.05.006.
[65] J. M. Mahdi and E. C. Nsofor, “Solidification enhancement of PCM in a triplex-tube thermal energy storage system with nanoparticles and fins,” *Appl. Energy*, vol. 211, no. May 2017, pp. 975–986, 2018, doi:

10.1016/j.apenergy.2017.11.082.
[66] J. M. Mahdi and E. C. Nsofor, "Melting enhancement in triplex-tube latent thermal energy storage system using nanoparticles-fins combination," *Int. J. Heat Mass Transf.*, vol. 109, pp. 417–427, 2017, doi: 10.1016/j.ijheatmasstransfer.2017.02.016.
[67] Z. Hu, A. Li, R. Gao, and H. Yin, "Enhanced heat transfer for PCM melting in the frustum-shaped unit with multiple PCMs," *J. Therm. Anal. Calorim.*, vol. 120, no. 2, pp. 1407–1416, 2015, doi: 10.1007/s10973-014-4370-6.
[68] M. Akgün, O. Aydin, and K. Kaygusuz, "Experimental study on melting/solidification characteristics of a paraffin as PCM," *Energy Convers. Manag.*, vol. 48, no. 2, pp. 669–678, 2007, doi: 10.1016/j.enconman.2006.05.014.
[69] M. Faghani, M. J. Hosseini, and R. Bahrampoury, "Numerical simulation of melting between two elliptical cylinders," *Alexandria Eng. J.*, vol. 57, no. 2, pp. 577–586, 2018, doi: 10.1016/j.aej.2017.02.003.
[70] E. Assis, L. Katsman, G. Ziskind, and R. Letan, "Numerical and experimental study of melting in a spherical shell," *Int. J. Heat Mass Transf.*, vol. 50, no. 9–10, pp. 1790–1804, 2007, doi: 10.1016/j.ijheatmasstransfer.2006.10.007.
[71] C. Zhao, M. Opolot, M. Liu, F. Bruno, S. Mancin, and K. Hooman, "Numerical study of melting performance enhancement for PCM in an annular enclosure with internal-external fins and metal foams," *Int. J. Heat Mass Transf.*, vol. 150, p. 119348, 2020, doi: 10.1016/j.ijheatmasstransfer.2020.119348.
[72] A. A. Al-Abidi, S. Mat, K. Sopian, M. Y. Sulaiman, and A. T. Mohammad, "Internal and external fin heat transfer enhancement technique for latent heat thermal energy storage in triplex tube heat exchangers," *Appl. Therm. Eng.*, vol. 53, no. 1, pp. 147–156, 2013, doi: 10.1016/j.applthermaleng.2013.01.011.
[73] A. Najafian, F. Haghighat, and A. Moreau, "Integration of PCM in domestic hot water tanks: Optimization for shifting peak demand," *Energy Build.*, vol. 106, pp. 59–64, 2015, doi: 10.1016/j.enbuild.2015.05.036.
[74] G. Righetti, R. Lazzarin, M. Noro, and S. Mancin, "Phase change materials embedded in porous matrices for hybrid thermal energy storages: Experimental results and modeling," *Int. J. Refrig.*, vol. 106, pp. 266–277, 2019, doi: 10.1016/j.ijrefrig.2019.06.018.
[75] R. Dhumane *et al.*, "Improving system performance of a personal conditioning system integrated with thermal storage," *Appl. Therm. Eng.*, vol. 147, no. August 2018, pp. 40–51, 2019, doi: 10.1016/j.applthermaleng.2018.10.004.
[76] Y. Du, J. Muehlbauer, J. Ling, V. Aute, Y. Hwang, and R. Radermacher, "RECHARGEABLE PERSONAL AIR CONDITIONING DEVICE," in *ASME 2016 10th International Conference on Energy Sustainability,Charlotte, North Carolina*, 2016.
[77] R. Dhumane *et al.*, "Enhancing the thermosiphon-driven discharge of a latent heat thermal storage system used in a personal cooling device," *Int. J. Refrig.*, vol. 88, pp. 599–613, 2018, doi: 10.1016/j.ijrefrig.2018.02.005.
[78] Y. Du, "BATTERY POWERED PORTABLE VAPOR COMPRESSION CYCLE SYSTEM WITH PCM CONDENSER," 2016.
[79] P. Promoppatum, S. C. Yao, T. Hultz, and D. Agee, "Experimental and

numerical investigation of the cross-flow PCM heat exchanger for the energy saving of building HVAC," *Energy Build.*, vol. 138, pp. 468–478, 2017, doi: 10.1016/j.enbuild.2016.12.043.
[80] H. L. Zhang, J. Baeyens, J. Degrève, G. Cáceres, R. Segal, and F. Pitié, "Latent heat storage with tubular-encapsulated phase change materials (PCMs)," *Energy*, vol. 76, pp. 66–72, 2014, doi: 10.1016/j.energy.2014.03.067.
[81] N. Calvet, X. Py, R. Olivès, J. P. Bédécarrats, J. P. Dumas, and F. Jay, "Enhanced performances of macro-encapsulated phase change materials (PCMs) by intensification of the internal effective thermal conductivity," *Energy*, vol. 55, pp. 956–964, 2013, doi: 10.1016/j.energy.2013.03.078.
[82] R. Velraj, R. V. Seeniraj, B. Hafner, C. Faber, and K. Schwarzer, "Experimental analysis and numerical modelling of inward solidification on a finned vertical tube for a latent heat storage unit," *Sol. Energy*, vol. 60, no. 5, pp. 281–290, 1997, doi: 10.1016/S0038-092X(96)00167-3.
[83] K. A. R. Ismail, C. L. F. Alves, and M. S. Modesto, "Numerical and experimental study on the solidification of PCM around a vertical axially finned isothermal cylinder," *Appl. Therm. Eng.*, vol. 21, no. 1, pp. 53–77, 2001, doi: 10.1016/S1359-4311(00)00002-8.
[84] A. Erek, Z. Ilken, and M. A. Acar, "Experimental and numerical investigation of thermal energy storage with a finned tube," *Int. J. Energy Res.*, vol. 29, no. 4, pp. 283–301, 2005, doi: 10.1002/er.1057.
[85] Q. Liu, X. B. Feng, Y. L. He, C. W. Lu, and Q. H. Gu, "Multiple-relaxation-time lattice Boltzmann model for simulating axisymmetric thermal flows in porous media," *Int. J. Heat Mass Transf.*, vol. 137, pp. 1301–1311, 2019, doi: 10.1016/j.ijheatmasstransfer.2019.03.118.
[86] Y. B. Tao and V. P. Carey, "Effects of PCM thermophysical properties on thermal storage performance of a shell-and-tube latent heat storage unit," *Appl. Energy*, vol. 179, pp. 203–210, 2016, doi: 10.1016/j.apenergy.2016.06.140.
[87] B. Peng *et al.*, "Effects of thermal conductivity and density on phase change materials-based thermal energy storage systems," *Energy*, vol. 172, pp. 580–591, 2019, doi: 10.1016/j.energy.2019.01.147.
[88] A. Sharma and D. Buddhi, "Effect of thermophysical properties of the PCM and heat exchanger material on the performance of a latent heat storage system," *Int. J. Sustain. Energy*, vol. 24, no. 2, pp. 99–105, 2005, doi: 10.1080/14786450512331329583.
[89] S. Ebadi, M. Al-Jethelah, S. H. Tasnim, and S. Mahmud, "An investigation of the melting process of RT-35 filled circular thermal energy storage system," *Open Phys.*, vol. 16, no. 1, pp. 574–580, 2018, doi: 10.1515/phys-2018-0075.
[90] M. Rahimi, A. A. Ranjbar, D. D. Ganji, K. Sedighi, M. J. Hosseini, and R. Bahrampoury, "Analysis of geometrical and operational parameters of PCM in a fin and tube heat exchanger," *Int. Commun. Heat Mass Transf.*, vol. 53, pp. 109–115, 2014, doi: 10.1016/j.icheatmasstransfer.2014.02.025.
[91] RUBITHERM GmbH, "RUBITHERM RT35 Phase change material," 2022. [Online]. Available: https://www.rubitherm.eu/media/products/datasheets/Techdata_-RT35_EN_02092022.PDF.

[92] W. Lin, Z. Ma, C. McDowell, Y. Baghi, and B. Banfield, “Optimal design of a thermal energy storage system using phase change materials for a net-zero energy Solar Decathlon house,” *Energy Build.*, vol. 208, p. 109626, 2020, doi: 10.1016/j.enbuild.2019.109626.

[93] M. Z. Malik, F. Musharavati, S. Khanmohammadi, S. Khanmohammadi, and D. D. Nguyen, “Solar still desalination system equipped with paraffin as phase change material: exergoeconomic analysis and multi-objective optimization,” *Environ. Sci. Pollut. Res.*, vol. 28, no. 1, pp. 220–234, 2021, doi: 10.1007/s11356-020-10335-9.

[94] Y. Zhou, S. Zheng, and G. Zhang, “Machine learning-based optimal design of a phase change material integrated renewable system with on-site PV, radiative cooling and hybrid ventilations—study of modelling and application in five climatic regions,” *Energy*, vol. 192, p. 116608, 2020, doi: 10.1016/j.energy.2019.116608.

[95] K. A. R. Ismail and M. M. Abugderah, “Performance of a thermal storage system of the vertical tube type,” *Energy Convers. Manag.*, vol. 41, no. 11, pp. 1165–1190, 2000, doi: 10.1016/S0196-8904(99)00140-5.

[96] A. Trp, K. Lenic, and B. Frankovic, “Analysis of the influence of operating conditions and geometric parameters on heat transfer in water-paraffin shell-and-tube latent thermal energy storage unit,” *Appl. Therm. Eng.*, vol. 26, no. 16, pp. 1830–1839, 2006, doi: 10.1016/j.applthermaleng.2006.02.004.

[97] H. M. Ettouney, I. Alatiqi, M. Al-Sahali, and S. Ahmad Al-Ali, “Heat transfer enhancement by metal screens and metal spheres in phase change energy storage systems,” *Renew. Energy*, vol. 29, no. 6, pp. 841–860, 2004, doi: https://doi.org/10.1016/j.renene.2003.11.003.

[98] F. Agyenim, P. Eames, and M. Smyth, “Heat transfer enhancement in medium temperature thermal energy storage system using a multitube heat transfer array,” *Renew. Energy*, vol. 35, no. 1, pp. 198–207, 2010, doi: 10.1016/j.renene.2009.03.010.

[99] M. J. Hosseini, A. A. Ranjbar, K. Sedighi, and M. Rahimi, “A combined experimental and computational study on the melting behavior of a medium temperature phase change storage material inside shell and tube heat exchanger,” *Int. Commun. Heat Mass Transf.*, vol. 39, no. 9, pp. 1416–1424, 2012, doi: 10.1016/j.icheatmasstransfer.2012.07.028.

[100] O. Mesalhy, K. Lafdi, A. Elgafy, and K. Bowman, “Numerical study for enhancing the thermal conductivity of phase change material (PCM) storage using high thermal conductivity porous matrix,” *Energy Convers. Manag.*, vol. 46, no. 6, pp. 847–867, 2005, doi: https://doi.org/10.1016/j.enconman.2004.06.010.

[101] M. J. Hosseini, M. Rahimi, and R. Bahrampoury, “Experimental and computational evolution of a shell and tube heat exchanger as a PCM thermal storage system,” *Int. Commun. Heat Mass Transf.*, vol. 50, pp. 128–136, 2014, doi: 10.1016/j.icheatmasstransfer.2013.11.008.

[102] V. R. Voller and C. Prakash, “A fixed grid numerical modelling methodology for convection-diffusion mushy region phase-change problems,” *Int. J. Heat Mass Transf.*, vol. 30, no. 8, pp. 1709–1719, Aug. 1987, doi: 10.1016/0017-

9310(87)90317-6.
[103] V. R. Voller, A. D. Brent, and C. Prakash, "The modelling of heat, mass and solute transport in solidification systems," *Int. J. Heat Mass Transf.*, vol. 32, no. 9, pp. 1719–1731, 1989, doi: https://doi.org/10.1016/0017-9310(89)90054-9.
[104] G. Righetti, G. Savio, R. Meneghello, L. Doretti, and S. Mancin, "Experimental study of phase change material (PCM) embedded in 3D periodic structures realized via additive manufacturing," *Int. J. Therm. Sci.*, vol. 153, no. October 2019, p. 106376, 2020, doi: 10.1016/j.ijthermalsci.2020.106376.
[105] "MATLAB." The MathWorks Inc., Natick, Massachusetts, 2018.
[106] S. Zhang, L. Pu, L. Xu, R. Liu, and Y. Li, "Melting performance analysis of phase change materials in different finned thermal energy storage," *Appl. Therm. Eng.*, vol. 176, no. March, p. 115425, 2020, doi: 10.1016/j.applthermaleng.2020.115425.
[107] M. Schimmelpfennig, K. Weber, F. Kalb, and K. Feller, "Volume expansion of paraffins from dip tube measurements," *Synthesewachs.Com*, no. 430 ml, pp. 1–9, 2007.
[108] M. Calati, D. Guarda, G. Righetti, and C. Zilio, "Numerical Modelling of a PCM Embedded in Periodic Structures," in *13th IIR Conference on Phase-Change Materials and Slurries for Refrigeration and Air Conditioning*, 2021, doi: 10.18462/iir.PCM.2021.2203.
[109] US Department of Energy, "Code of Federal Regulations, 2016, Title 10 – Energy, Chapter X - DEPARTMENT OF ENERGY (GENERAL PROVISIONS)," 2016.
[110] RUBITHERM GmbH, "RT62HC." [Online]. Available: https://www.rubitherm.eu/media/products/datasheets/Techdata_-RT62HC_EN_09102020.PDF.
[111] K. Deb, *Multi-Objective Optimization using Evolutionary Algorithms*. 2001.
[112] T. S. Mathis, N. Kurra, X. Wang, D. Pinto, P. Simon, and Y. Gogotsi, "Energy Storage Data Reporting in Perspective—Guidelines for Interpreting the Performance of Electrochemical Energy Storage Systems," *Adv. Energy Mater.*, vol. 9, no. 39, pp. 1–13, 2019, doi: 10.1002/aenm.201902007.
[113] J. Woods, A. Mahvi, A. Goyal, E. Kozubal, A. Odukomaiya, and R. Jackson, "Rate capability and Ragone plots for phase change thermal energy storage," *Nat. Energy*, vol. 6, no. 3, pp. 295–302, 2021, doi: 10.1038/s41560-021-00778-w.